1-1-2012

New precursors and chemistry for the growth of transition metal films by atomic layer deposition

Thomas Joseph Knisley
Wayne State University,

Recommended Citation
Knisley, Thomas Joseph, "New precursors and chemistry for the growth of transition metal films by atomic layer deposition" (2012). *Wayne State University Dissertations.* Paper 571.

NEW PRECURSORS AND CHEMISTRY FOR THE GROWTH OF TRANSITION METAL FILMS BY ATOMIC LAYER DEPOSITION

by

THOMAS JOSEPH KNISLEY

DISSERTATION

Submitted to the Graduate School

of Wayne State University,

Detroit, Michigan

in partial fulfillment of the requirements

for the degree of

DOCTOR OF PHILOSOPHY

2012

MAJOR: CHEMISTRY (Inorganic)

Approved by:

Advisor Date

DEDICATION

I dedicate this dissertation to my lovely wife, Nicole Rose Knisley, who supported me each step of the way. Without her constant support and motivation, this dissertation would not be possible.

“If I find 10,000 ways something won't work, I haven't failed. I am not discouraged, because every wrong attempt discarded is just another step forward.”

-Thomas A. Edison

ACKNOWLEDGMENTS

Completing my Ph.D. is one of the most challenging and demanding activities in the first 27 years of my life. The greatest and worst instances of this journey have been shared with numerous individuals. It has been a great privilege to spend several years in the Department of Chemistry at Wayne State University, and its members will always remain dear to my heart.

My first debt of gratitude must undoubtedly go to my advisor, Dr. Charles H. Winter. He patiently provided the ideas, vision, advice, encouragement, and challenge necessary for me to progress through the doctoral program and complete my dissertation. He has fostered experiences that have allowed me to make invaluable connections within ALD community. Dr. Winter has been a strong supporter of my efforts throughout my graduate career and has always given me vast freedom to pursue results by nearly all means necessary.

I am also highly grateful to my committee members, Dr. Matthew J. Allen, Dr. James H. Rigby, and Dr. Mark Cheng, for their comments, guidance, and helpful suggestions on my thesis. Their guidance has served me well and I owe them sincere appreciation for this role.

I would like to thank those individuals within the Lumigen Instrument Center at Wayne State who have directly impacted the advancement of my research. I am also grateful for the advice and counsel that I received from Dr. Ronald Baird. Furthermore, I would like to thank the past and present Winter group members for their constant support and friendship. In particular, I would like to thank Dr. Mahesh Karunarathne and Dr. Charles Dezelah for the helpful synthesis advice and useful ALD discussions. Finally, I want to give special thanks to Dr. Mark J. Saly for the insightful and often challenging discussions that we have had.

I wish to thank my parents, Jill D. Boucher and Thomas C. Knisley who have consistently driven me towards success. Without this motivation, I simply would not be where I am at today. Finally, I give endless appreciation and thanks to my wife, Nicole Rose Knisley, whose boundless love and encouragement have allowed me to begin, continue, and finish this journey.

TABLE OF CONTENTS

LIST OF TABLES

LIST OF FIGURES

LIST OF CHARTS

LIST OF ABBREVIATIONS

ABBREVIATION	**LONG FORM**
Acac	Acetylacetonate
AFM	Atomic Force Microscopy
ALD	Atomic Layer Deposition
CCTBA	μ^2-η^2-(*t*Bu-acetylene)-dicobalthexacarbonyl
CMOS	Complimentary Metal-Oxide Semiconductor
CVD	Chemical Vapor Deposition
DMAP	1-Dimethylamino-2-propoxide
DMAMB	1-Dimethylamino-2-methyl-butoxide
DRAM	Dynamic Random Access Memory
ERDA	Elastic Recoil Detection Analysis
EtCp	Ethylcyclopentadienyl
FED	Field Emission Display
LED	Light Emitting Diode
ILD	Interlayer Dielectric
MeCp	Methylcyclopentadienyl
MOSFET	Metal Organic Semiconducting Field Effect Transistor
MRAM	Magnetoresistive Random Access Memory
OtBu	*tert*-butoxy
PVD	Physical Vapor Deposition
ReRAM	Resistive Random Access Memory
RSC	Relative Sticking Coefficient
SEM	Scanning Electron Microscopy

THF	Tetrahydrofuran
tmhd	2,2,6,6-tetramethylheptanedionate
TGA	Thermogravimetric Analysis
tBu$_2$DAD	1,4-di-*tert*-butyl-1,3-diazabutadiene
USB	Universal Serial Bus
XPS	X-Ray Photoelectron Spectroscopy
XRD	X-Ray Diffraction
1	Cr(tBu$_2$DAD)$_2$
2	Mn(tBu$_2$DAD)$_2$
3	Fe(tBu$_2$DAD)$_2$
4	Co(tBu$_2$DAD)$_2$
5	Ni(tBu$_2$DAD)$_2$
6	Cu(dmap)$_2$

CHAPTER 1

Introduction

1.1 Trends in Microelectronics Device Miniaturization

Thin film growth is an essential step in the production of functional devices and materials. Current trends in microelectronics device manufacturing are calling for the growth of conformal films at thickness ranges from tens of nanometers down to a few atomic layers.[1] The drive and motivation towards the continued miniaturization of device features was predicted by Gordon Moore in 1965.[1] His publication became the doctrine commonly known as "Moore's Law" which stated that the number of transistors on a single device will double every 18-24 months. The semiconductor industry has maintained pace in accordance with this prediction for the last 60 years through constant innovation using new materials and transistor architectures. Exponential growth of transistor density in logic and memory devices has led to devices that are smaller, faster, and increasingly power efficient. Continued advancement in this regard has led to a fundamental shift in computing technology that has ushered in the Digital and Information Age.

Unfortunately, semiconductor device sizes cannot be reduced to the smallest possible dimension due to the physical limitations dictated by quantum mechanics. While the fundamental limits are challenging to overcome, they can often be mitigated by introducing novel materials and unique device architectures. Constant advancement in technologies such as photolithography and thin film growth have allowed the industry to achieve the modern level of design for logic and memory devices with transistor gate lengths of 22 and 28 nm, respectively.

To manufacture devices of such complexity, thin films grown with absolute precision and thickness control are required. In addition, uniform coverage of highly detailed, three-dimensional features with high aspect ratios is required if the current trend in microelectronics miniaturization is to continue.[2,3] With functional devices predicted to reach the 14 nm node in early 2014 and 10 nm in 2016, the need for producing thin conformal films with precise thickness control becomes increasingly important.[4] This drive toward smaller feature sizes will require controlled growth of films as thin as 1 nm.

1.2 Important Materials Containing Transition Metals

Thin films containing first row transition metal elements have many important current and future applications. Copper has replaced aluminum as the interconnect material in electronics due to its lower resistivity and higher resistance towards electromigration. Metallic copper is applied in trenches and vias through a two-step process involving the creation of a thin, conformal copper seed layer by physical vapor deposition, followed by electrodeposition copper fill.[2] However, copper does not adhere well to SiO_2 surfaces, and the creation of a continuous copper seed layer is difficult. In response to this challenge, other metal seed layers for Cu metallization have been explored, including chromium, cobalt, and ruthenium.[3] Copper is known to diffuse readily into SiO_2 layers and Si substrates during the high temperatures encountered in microelectronics device fabrication. Therefore, a barrier between copper and silicon is required. This barrier must stop the diffusion of copper at deposition temperatures long enough for device fabrication, must be unreactive toward both copper and silicon, and should demonstrate good adhesion to both copper and silicon. In addition, barriers in future devices should be $\leq$ 5 nm thick to reduce the electrical resistivity of the interconnect structure.[2,4] Materials that are currently under consideration as advanced barriers include TaN and WN_x ($x = 0.5$-1), as well as ternary compositions of these materials containing carbon or silicon.[5] However, ≤ 5 nm thick layers of these nitride-based barrier materials may not serve as effective copper diffusion barriers.[2] In reaction to this concern, considerable effort has been directed toward identification of alternative barrier materials. Very thin films (≤ 5 nm) of transition metals such as manganese,[6] chromium, ruthenium,[7] and others have emerged as new copper diffusion barrier materials.[8] It has been recently shown that annealing of a 150 nm thick 90/10 Cu/Mn alloy film on SiO_2 substrates at temperatures between 250-450 °C led to migration of the Mn atoms towards the SiO_2 interface to form a separate 2-8 nm $MnSi_xO_y$ layer between the SiO_2 and Cu layers (Figure 1).[6] Most notably, this Mn-containing layer served as a Cu diffusion barrier for up to 100 h at 450 °C.[6c] This work is very significant, as it suggests that ultrathin Mn-based films can replace current nitride-based barriers (TaN, WN_x) in future microelectronics devices. However, growth of the Cu/Mn alloy films relied upon a physical deposition method (sputtering),[9] which affords poor conformal coverage in the narrow and deep features of future microelectronics devices.[2,8] There are other applications that require the growth of thin transition metal films. Magnetoresistive random access memory (MRAM) devices require thin, conformal layers of magnetic metals such as Ni, Co, or Fe.[9] More applications will be discussed in Chapter 1.4.

Figure 1. ALD Growth of $MnSi_xO_y$ Diffusion Barriers.

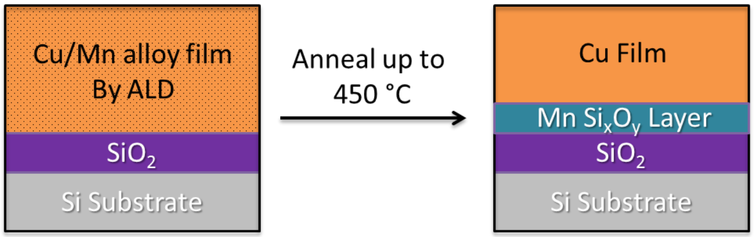

1.3 Thin Film Deposition Methods

Vapor deposition methods that are currently employed, including physical vapor deposition (PVD), chemical vapor deposition (CVD) and atomic layer deposition (ALD), allow the formation of uniform films throughout the micron and nanometer range.[10] Film thickness control is challenging for films ≤ 100 nm and becomes ever more difficult in nanoscale features.[10] Conformality is the ability of a film to coat a topographically complex surface uniformly (Figure 2). In order for a device to function appropriately, all three dimensional features (trenches and vias) should be coated uniformly. PVD, CVD, and ALD are able to coat features uniformly to varying degrees depending on feature size, which will be discussed in detail below. The research outlined in this thesis focuses upon precursor and process development for ALD.

Figure 2. Film conformality illustration for various thin film deposition methods.

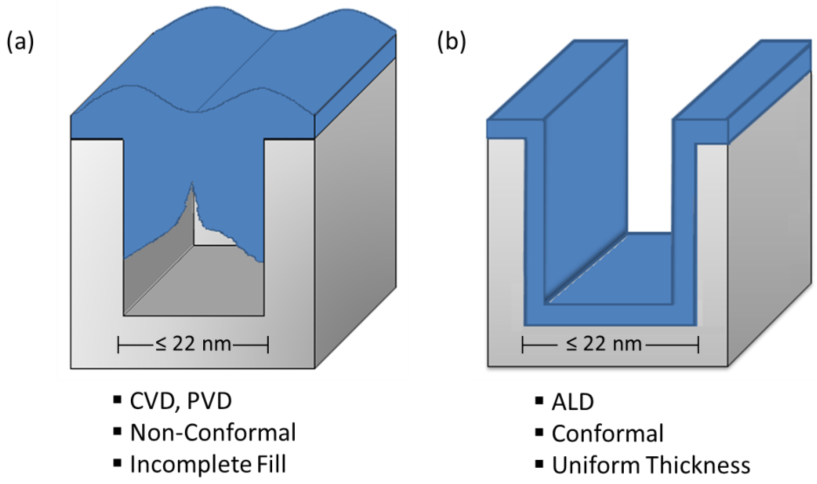

1.3.1 Physical Vapor Deposition (PVD)

In a typical PVD-type film growth process, discrete atoms are removed from solid source material and travel through an evacuated vacuum chamber until the atoms collide on a substrate of interest and condense to create a thin film (Figure 3).[11] The removal of the surface-bound source atoms can be accomplished by laser ablation, thermal heating, or by physically bombarding the surface with electrons, atoms, ions, or photons.[11] A standard evaporative-type PVD setup is shown in Figure 3a. There are two types of source evaporation techniques: quasi-equilibrium and non-equilibrium-based processes.[11] In the quasi-equilibrium example, the source is held in a near steady state equilibrium between the liquid and gas phase. Knudsen cells often consist of a heated vessel with a small canal. The source vapor slowly diffuses through the tunnel and travels towards the target substrate and condenses upon the surface. In non-equilibrium evaporative methods, the source is vaporized in an open vessel, such as a boat or ceramic crucible, and the source vapor distributes through the chamber towards the target substrate.[11] Another non-equilibrium evaporation process used in PVD involves the use of an electron beam. The electron beam is focused towards the target to cause confined heating at the surface. After sufficient heating, source vaporization is induced which allows for target molecules to diffuse and travel towards to substrate of interest.

Figure 3. (a) Evaporative PVD and (b) Sputter PVD.[11]

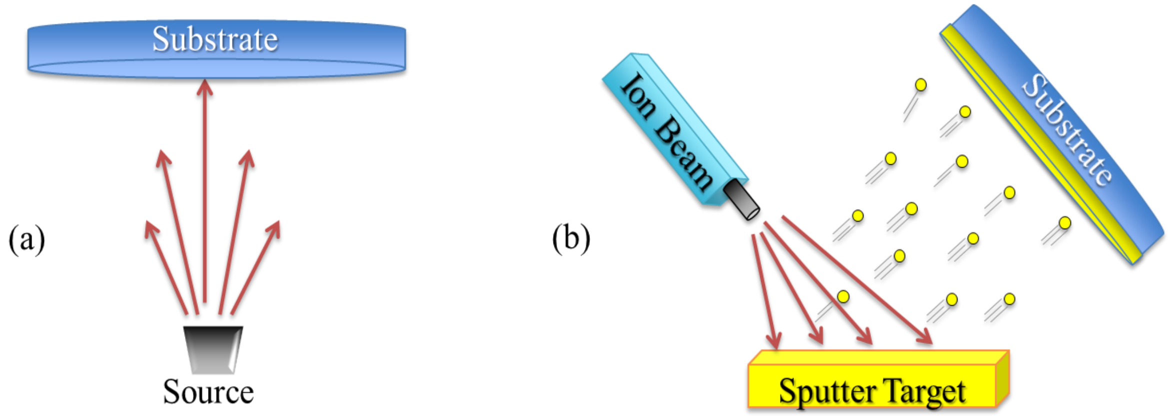

In sputter-type PVD film growth, a target material is bombarded with high energy particles such as inert gas ions, molecules, or neutral atoms.[11] Induced collision of energetic particles results in the subsequent ejection of surface-bound atoms. The discharged atoms are then directed towards a substrate and condense upon the surface resulting in the formation of a thin film (Figure 3b). Sputter PVD processes are economical, and can allow for the deposition of highly pure and uniform films over large, two-dimensional surfaces. However, films grown by sputtering have a tendency to have poor thickness conformality in nanoscale features due to the line-of-sight nature of this technique.

Evaporative and sputtered PVD have the capability to grow thin films at high growth rates. However, in the instance of evaporative sputtering, the film growth is highly directional leading to films that have an inherent pillar-type microstructural features.[11] Directionality in evaporative PVD is a consequence of the low probability of in-flight collisions with other non-target gas atoms.[11] In sputter PVD, film growth occurs in a non-directional manner. Presumably, this is a result of the increased gas pressure in the deposition space that leads to gas-phase scattering of the sputtered target atoms. Resultant multidirectional growth from this process generates a wide distribution of atoms upon the target substrate leading adequate step-coverage in three-dimensional surface features.[11] Unfortunately, many PVD processes result in film growth with poor step coverage in features with high aspect ratios (> 10:1), which is associated with the low surface mobility of source atoms, as well as the inherent directionality of PVD film growth.[11] As a result, adsorbing species do not penetrate and coat the intricate three-dimensional features and high-aspect-ratio structures within advanced microelectronic devices.

1.3.2 Thin Film Growth by CVD

In CVD film growth, one or more precursors are introduced to a heated substrate.[12] Once the precursors are in close proximity or in contact with the heated substrate, a series of complex gas phase and surface reactions afford a thin film of interest.[12] CVD is widely employed in the semiconductor industry because of the high throughput of thin conformal films by this method.[12] Figure 4 exemplifies the general scheme of CVD growth. First, the precursors are introduced to the heated substrate typically by an inert gas stream. Once the precursors approach the substrate within the heated region of the reaction chamber, many complex processes can occur. The precursor may react with other precursor molecules in the gas phase, which can result in gas phase precipitation. Gas phase precipitation can lead to the formation of fine particles and impurities which can incorporate into the film, affording defects and non-conformality.[12b] Intact precursor molecules can also adsorb on the surface and undergo oxidation and reduction reactions, depending upon reaction conditions. Adsorption can be classified into physisorption (weak van der Waals interactions on the substrate surface) or chemisorption (where the adsorbing molecule chemically reacts with the functionalized substrate surface). Excess reactants and volatile byproducts are taken into the inert gas stream and are eliminated out of the reaction chamber.

Figure 4. Typical CVD scheme in the deposition of graphene from methane and hydrogen gas.

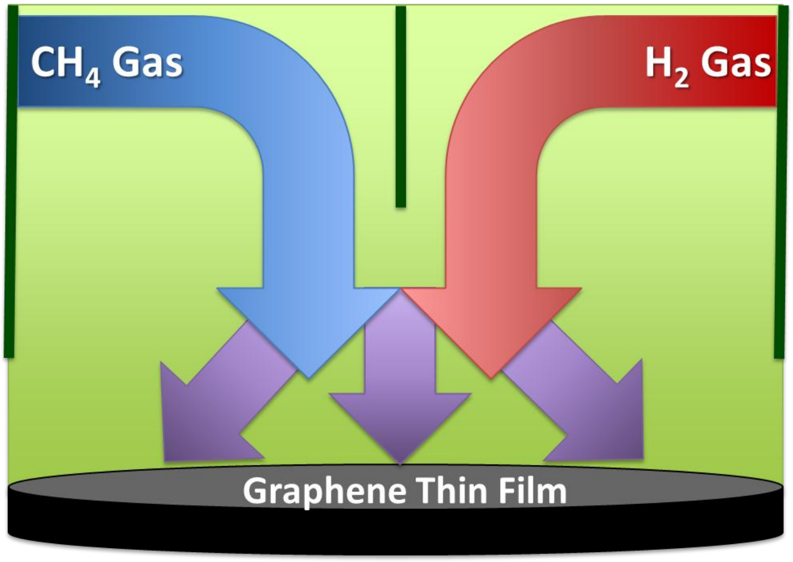

Selection of precursors is very important in CVD, since film growth proceeds by complex surface and gas phase reactions. In addition, CVD precursors must meet a stringent set of requirements that include volatility, thermally stability, and reactivity at the desired deposition temperatures.[12b] The properties of the precursor can have profound effects on the uniformity, conformality, and resultant step-coverage of a deposited thin film. The probability of a precursor to react with or adhere to a substrate surface is called the relative sticking coefficient (RSC).[12b] The RSC of a molecule depends upon the surface conditions as well as the chemistry of the precursor at the substrate temperature. A highly reactive precursor is expected to have a high RSC value. In contrast, precursors with low reactivity, and hence a low RSC value, would be relatively inert at the deposition temperature and be prone to surface desorption. However, it has been shown that precursors with low RSC values have high surface mobility and consequently afford conformal thin films in featured substrates.[12b]

CVD and PVD are the primary film growth techniques in the semiconductor industry due to their high throughput and ability to produce conformal thin films. However, it can be difficult to obtain conformal films on high-aspect-ratio features using these methods. With the rapid miniaturization of feature sizes in microelectronics devices and increased use of such features, a deposition technique that can lead to thin, uniform films in nanoscale topographies will be required. As a result, there has been increased interest in ALD because of its inherent ability to deposit thin, conformal films with excellent thickness control.[13]

1.3.3 Atomic Layer Deposition

ALD was developed in the 1970's by Tuomo Suntola for the production of electroluminescent flat panel displays.[14,15] Continued device miniaturization in the semiconductor industry has led to a need for thin, conformal films with excellent thickness control at the nanoscale thickness regime.[14] ALD is able to coat high-aspect-ratio features with perfect conformality and excellent thickness control.[14] In contrast to CVD, an ALD process requires precursors to be pulsed into the reaction chamber separately. Film growth by ALD occurs in a stepwise, self-limited manner, which allows for sub-nanometer control of film thickness.[10] Under optimized deposition conditions, the growth rate per cycle remains constant, allowing the film thickness to be dependent upon the number deposition cycles. This self-limiting growth mechanism allows for defined thickness control and conformality upon various substrates.[10-12] ALD is emerging as a primary deposition technique for the manufacturing of functional materials and microelectronic devices in the years to come.[4,10,13,18]

In a typical ALD process, a metal precursor is transported in the vapor phase by an inert carrier gas into the reaction chamber, where it adsorbs to reactive surface sites upon the substrate. This process is illustrated in Figure 5 with the deposition of Al_2O_3 thin films on silicon substrates with native oxide. Once all accessible surface sites have become occupied, the surface is saturated and unreacted precursor and reaction byproducts are eliminated out of the reactor using an inert gas purge. A pulse of a second vapor precursor subsequently reacts with surface adsorbed metal precursor to produce the desired thin film material. To conclude a growth cycle, a second inert gas purge is then performed to remove additional byproducts and excess precursor.[10] Repetition of this process affords smooth thin films with excellent thickness control.

Figure 5. Steps in the ALD cycle of Al_2O_3 using trimethylaluminum and water.

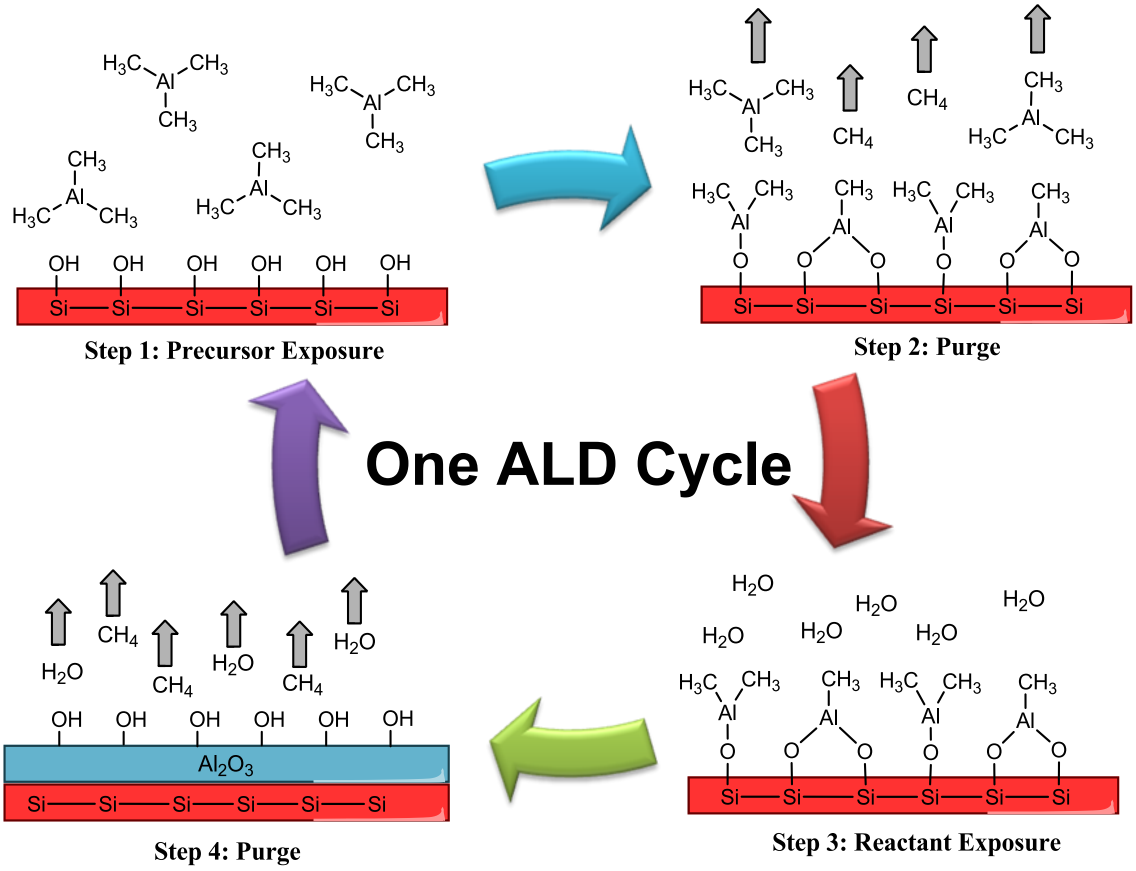

Step 1: Precursor Exposure

Step 2: Purge

Step 3: Reactant Exposure

Step 4: Purge

In ALD, a precursor adsorbs to or reacts with the active surface sites on the target substrate. Once all of the active sites are occupied, excess precursor molecules that are purged out of the reaction chamber.[10] This results in the formation of one atomic layer. The hallmark of ALD growth is exhibited in Figure 6, where a plot of growth rate versus precursor pulse length affords a region of constant growth rate that corresponds to the point where the precursor has reacted with all available surface reactive sites. The minimum precursor pulse length needed to achieve a constant growth rate is termed the minimum saturative dose. If the precursor is thermally stable at the deposition temperature, no further film growth reactions occur once the minimum surface saturative dose has been delivered.

Figure 6. Plot of precursor pulse length versus growth rate. Region A (**red**): Sub-saturative film growth. Region B (**green**): Surface sites are saturated and film growth is self-limited.

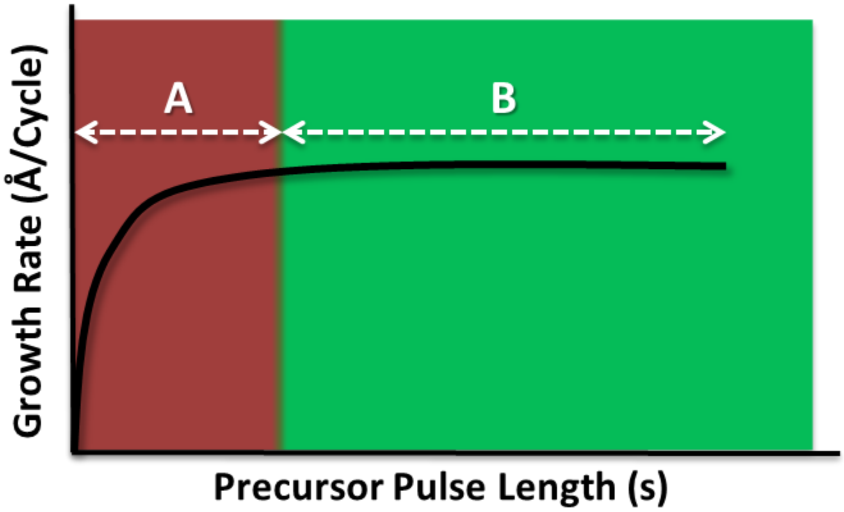

Plotting precursor pulse length as a function of deposition temperature allows one to assess the thermal growth properties of an ALD process. In most ALD processes, there is a region of constant growth rate that is independent of the deposition temperature (Figure 7, **region II**).[10] This temperature region is referred to as the “ALD Window”. At lower growth temperatures, an increase in growth rate is suggestive of precursor condensation (dashed line,

region I). Inadequate precursor reactivity at lower deposition temperatures can lead to a reduction in growth rate (solid line, **region I**). At higher deposition temperatures, a decrease in growth rate can occur as a result of thermal desorption of surface bound precursor molecules or loss of surface-reactive sites (dashed line, **region III**). An increase in growth rate can also be observed if the process temperature is in excess of the precursor decomposition temperature (solid line, **region III**). Although there are some advantages to having an ALD window, such as precise thickness control across broad temperature ranges, it is not necessary to be considered ALD growth. Demonstrating surface saturation is the key to establishing self-limited growth.

Figure 7. A plot of temperature versus growth rate. Region I (**blue**): Insufficient reactivity (solid line), Precursor condensation (dashed line). Region II (**green**): ALD window. Region III (**red**): Precursor desorption (dashed line), Precursor self-decomposition (solid line).

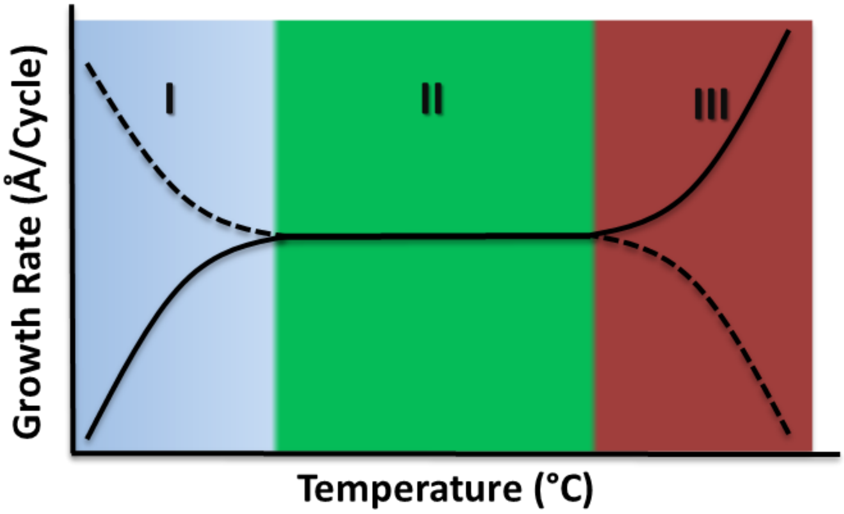

ALD film growth has several advantages over other vapor phase methods. The thickness of the film is only dependent on the number of reaction cycles, affording thin films with excellent thickness control. Since ALD growth occurs only by surface reactions, the precursor fluxes and gas flows are not crucial to the formation of uniform and conformal films over large areas.[10] Keeping the precursors separated allows for the use of highly reactive compounds, which can afford growth at low temperatures. Furthermore, the presence of an ALD window for a particular process allows the growth rate to remain constant even in the event of temperature fluctuations.[10]

Thermal and plasma ALD are two types of processes that are often considered when discussing this type of film growth.[17] Thermal ALD processes use the heat of the deposition reactor to drive growth thermodynamically. Plasma processes, often noted as plasma-enhanced ALD (PEALD), use high-energy radicals to react with surface bound precursor molecules. Plasma sources can also offer flexibility when developing new ALD processes and can include sources from O_2, N_2, NH_3, H_2, and H_2O vapor. Advantages of PEALD processes include higher growth rates relative to thermal processes and lower process temperatures due to the highly reactive nature of the generated plasma species. These attributes are attractive towards developing processes for making oxide and nitride films by ALD.

In metal ALD process development, there exists a set of stringent requirements to fulfill the needs of the microelectronic industry. These include depositing metals at temperatures of $\leq$ 100 °C to afford smooth films, promote facile nucleation, and give continuous films even at thicknesses of a few nanometers. At higher temperatures, metal atom agglomeration occurs, leading to high surface roughness, void formation, and eventual device failure. In addition, plasma processes are to be avoided due to the fact that plasma species suffer from low conformal coverage in plasma processes. This occurs due to the radical recombination of plasma species along the feature leading to a loss of reactive growth species. Furthermore, plasmas are known to induce substrate damage and lead to rough films.

Overall, the microelectronics industry would prefer to limit any viable metal deposition process to thermal ALD in device manufacturing.

1.4 Transition Metal Precursors for ALD and CVD

Unfortunately, there is a limited number of chemical precursors available that have high thermal stability, reactivity, and vapor pressure suitable for ALD film growth to occur. Thermal decomposition of the precursor within the deposition chamber would lead to a loss of the self-limited growth mechanism, leading to CVD-type growth. Precursor molecules are also required to adsorb on or react with surface sites and reactivity must be sufficient towards other precursors. In addition, sufficient volatility of the precursor is also necessary to ensure effective mass transport to achieve self-limited film growth. These properties jointly contribute to the lack of suitable transition metal precursors available for use in ALD. As a result, new ALD precursors with optimized properties must be developed and tested to allow broad application of the ALD technique. A description outlining the state of the literature regarding transition metal thin film precursors will be discussed below.

1.4.1 Chromium and Iron

Thin films containing chromium and iron have received attention due to their potential use in magnetic, catalytic, optical, and electrical applications.[3] Chromium metal in particular, has been proposed as a seed layer for copper metallization technology.[3] While chromium metal films have never been deposited by CVD or ALD, Cr_2O_3 films were deposited using $Cr(CO)_6$ and O_2 as the oxygen source.[18,19] Other volatile chromium source compounds have included $Cr(B_3H_8)_2$,[20] $Cr(iPrNC(CH_3)NiPr)_3$,[21] $Cr(tBuNC(CH_3)NtBu)_2(X)$ (X = pyrazolate, 1,2,4-triazolate),[21] and $Cr(tBu_2DAD)_2$.[22]

There have been a small number of metal-organic precursors reported for iron-containing materials. Precursors for the CVD growth of Fe_2O_3 include $Fe(CO)_5$[23] and $Fe_2(OtBu)_6$.[24] Volatile ALD iron source precursors include $Fe(tmhd)_3$,[25] $Fe_2(OtBu)_6$,[24] $Fe(Cp)_2$,[26,27] and $Fe(tBu_2DAD)_2$.[22] ALD Fe_2O_3 was demonstrated from $Fe(Cp)_2$ and ozone with a growth rate of 1.4 Å/cycle at 200 °C.[27] ALD growth of iron metal upon aerogels was claimed, although no details were discussed.[28] Thermal self-decomposition of $Fe(tBu_2DAD)_2$ to Fe metal at 260 °C illustrates the potential of this precursor in CVD.[22]

Chart 1. Selected iron precursors for ALD and CVD.

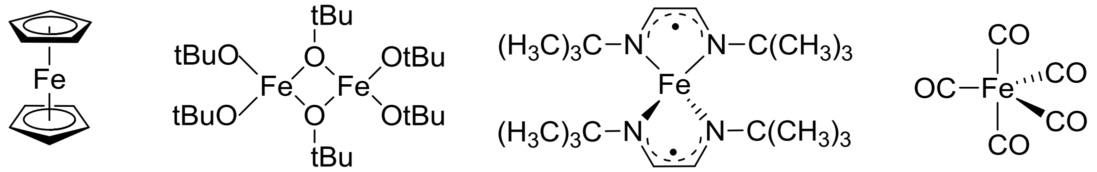

$Fe(Cp)_2$ **$Fe_2(OtBu)_6$** **$Fe(tBu_2DAD)_2$** **$Fe(CO)_5$**

1.4.2 Manganese

Manganese-containing thin films have important applications in memory and logic devices, sensors, flat panel displays, and battery technologies. Manganese silicate copper diffusion barriers in advanced integrated circuits have also spurred interest in developing manganese films.[6] Given the large negative redox couple of Mn^{2+}/Mn^0 (E_0= -1.185 V),[29a] Mn^{2+} is very difficult to reduce. While there are numerous examples of PVD Mn,[6] only one documented example of ALD Mn exits. Presumably the difficulty in reducing Mn^{2+} to Mn^0 explains why there is one example of the deposition of ALD Mn.[29b] This process entailed the use of $Mn(tmhd)_3$ and hydrogen plasma, although specific details were not mentioned.[29b]

Manganese oxides (MnO, MnO_2) have been deposited using CVD and ALD methods. MnO is the exclusive composition of thin films produced by CVD.[30,31] ALD growth of MnO has been demonstrated from $Mn(EtCp)_2$ and H_2O with a growth rate of 1.2 Å/cycle at 100 °C.[32] ALD MnO_2 was demonstrated using $Mn(tmhd)_3$ and ozone.[33,34] Unfortunately, only a few precursors have been developed for manganese. Suitable thin film manganese precursors include $Mn(EtCp)_2$,[32] $Mn(tmhd)_3$,[33,34] $Mn_2(CO)_{10}$,[35] $Mn(MeCp)_2$,[35] $Mn(iPrNC(nBu)NiPr)_2$,[36] and $Mn(tBu_2DAD)_2$.[22] The surface chemistry of $Mn_2(CO)_{10}$ on SiO_2 and Cu surfaces have been extensively studied using XPS with hopes of forming metallic films.[35] However, it was found that MnO and manganese silicates and not Mn metal are being produced.[35c]

Chart 2. Selected manganese precursors for ALD and CVD.

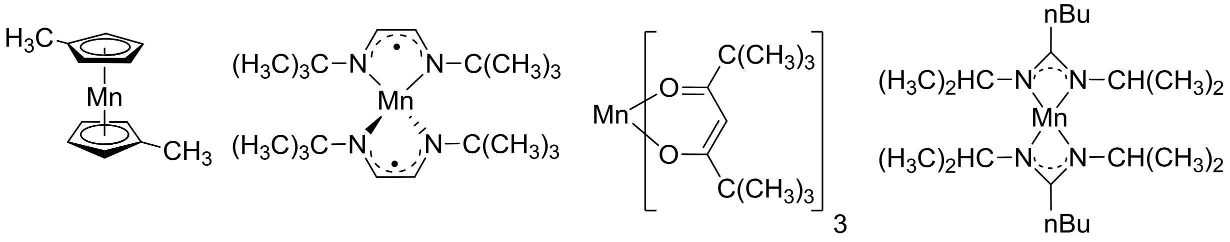

$Mn(MeCp)_2$ **$Mn(tBu_2DAD)_2$** **$Mn(tmhd)_3$** **$Mn(iPrNC(nBu)NiPr)_2$**

1.4.3 Cobalt

Cobalt is an important element in magnetoresistive devices, integrated circuits, lithium battery technologies, and spintronics.[37] The deposition of highly conformal cobalt metal films is the key process responsible for the continued miniaturization of dynamic random access memory (DRAM) technology. Selective deposition of Co-containing films on Cu lines is also useful for preventing Cu diffusion into the overlying ILD layer.[4] Such technology is responsible for the ongoing development of high density information storage such as USB flash memory and solid state drives. Thin films of CoO and Co_3O_4 have been previously deposited by CVD and ALD using various oxygen sources that include water and ozone.[38,39] A cobalt ALD metal process was claimed using $CoCp(CO)_2$ and $Co(Cp)_2$ as the cobalt source precursors and NH_3 plasma as the reducing source.[40] However, the deposition temperature of 300 °C is above the thermal decomposition temperature of the cobalt precursors indicating a large CVD component to the film growth. Other plasma ALD processes for reducing cobalt precursors have been developed but there is often little mention of surface roughness and film composition.[41,42,44,45] A handful of Co ALD processes are known.[43,46] A thermal Co ALD process was claimed using $Co(iPrNC(nBu)NiPr)_2$ and NH_3 gas, however a process temperature of 350 °C was required for film growth.[43] Another thermal Co ALD process was demonstrated at 140 °C using $Co(tBuCHCH{=}CH_2)(CO)_3$ and 1,1-dimethylhydrazine as the reducing agent.[46a] This study explored the unique ability of this process to deposit Co selectively on hydrogen-terminated silicon using surface analysis techniques. Other volatile source precursors for Co have included $Co(tmhd)_2$,[26,27,47] $Co_2(CO)_8$,[41] Co(Cp)(iPrNC(nBu)NiPr),[44] CCTBA,[46b] and $Co(tBu_2DAD)_2$.[22]

Chart 3. Selected cobalt precursors for ALD and CVD.

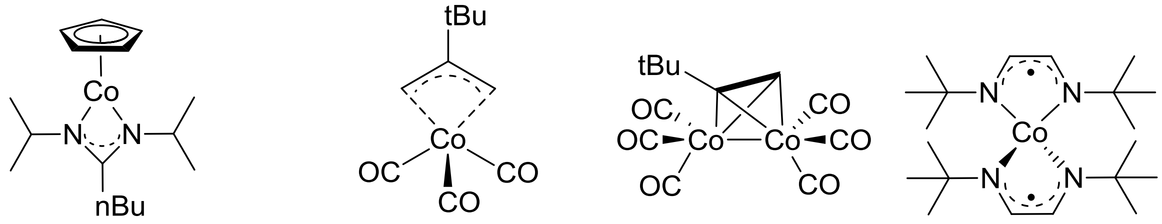

Co(Cp)(iPrNC(nBu)NiPr) **$Co(tBuCHCH{=}CH_2)(CO)_3$** **CCTBA** **$Co(tBu_2DAD)_2$**

1.4.4 Nickel

Thin films of nickel and its alloys (NiSi, Ni_3N) have inherently low contact resistivity and are useful as contact materials in metal oxide semiconductor field effect transistor (MOSFET) devices.[48] Silicidation of Ni metal or Ni_3N using silane gas results in the formation of NiSi, which is a low resistivity material used in the gate contact junction of

MOSFET devices.[48,60] Several Ni metal CVD processes have been reported that use $Ni(CO)_4$ or nickelocene derivatives as the nickel precursor.[49] All Ni ALD processes reported to date use reactive plasmas as the reducing species,[50] presumably due to the difficulty in reducing Ni^{2+} to Ni^0 (E_0= -0.257 V).[29a] There is a drive to avoid plasma-based processes for the deposition of ALD metal films for the reasons previously mentioned.

Nickel oxide (NiO) films have also received much attention for their useful optical, magnetic, and electrical properties.[51] Films of this material have been deposited by both CVD[52] and ALD[53] methods using water or ozone as the oxygen sources. Currently, NiO films are being integrated into resistive switching random access memory (ReRAM), a next generation memory technology with the promise of faster speeds and low power consumption.[54] Volatile source precursors for nickel include $Ni(dmamp)_2$,[53a,53f] $Ni(dmamb)_2$,[50,52f,56] $Ni(tmhd)_2$,[53c,53d] $Ni(Cp)_2$,[53b,53e] $Ni(EtCp)_2$,[53b] $Ni(ohapim)_2$,[57] Ni(Cp)(allyl),[58] Ni(tta),[59] $Ni(tBuNC(nBu)NtBu)_2$,[60] $Ni(OC(CF_3)CHCMeNH)_2$,[61] and $Ni(tBu_2DAD)_2$.[22]

Chart 4. Selected nickel precursors for ALD and CVD.

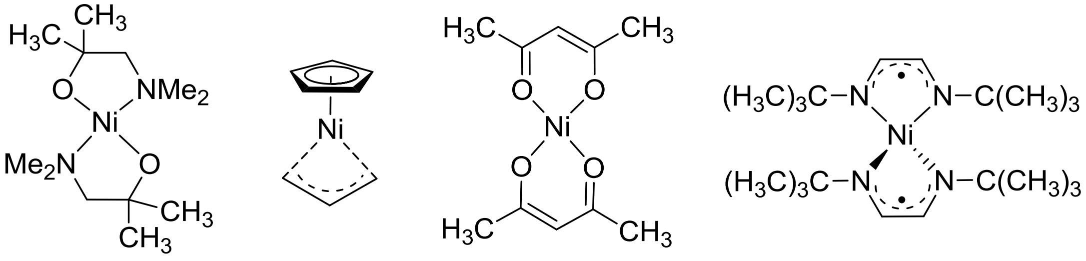

$Ni(dmamp)_2$ **Ni(Cp)allyl** **$Ni(acac)_2$** **$Ni(tBu_2DAD)_2$**

1.4.5 Copper

Copper is the primary interconnect material in microelectronics devices, due to its low resistivity and high resistance to electromigration.[1a] The dimensions of the smallest features in microelectronics devices are scheduled to reach 22 nm by 2012,[3] which places severe demands upon the film growth techniques used in device fabrication. Copper metal needs to be deposited by ALD to meet future conformality and film thickness uniformity requirements in microelectronics devices. In addition, the copper metal should be deposited ideally at ≤ 100 °C to afford the smallest surface roughnesses, promote facile nucleation, and give continuous films even at thicknesses of a few nanometers. Existing copper ALD processes have yet to meet all of these demands. Examples of direct copper ALD processes include $CuL_2/ZnEt_2$ at 100-150 °C (L = $OCHMeCH_2NMe_2$, *β*-ketiminate, *β*-diketiminate),[62,63] $Cu(tmhd)_2/H_2$ at 190-260 °C,[64] $[Cu(sBuNCMeN\text{-}sBu)]_2/H_2$ at 150-250 °C,[65] $Cu(hfac)_2$/isopropanol at 300 °C,[66] $CuCl/H_2$ at 360-410 °C,[67] and CuCl/Zn at 440-500 °C.[68] ALD growth of copper thin films was claimed from a copper(I) β-diketiminate precursor and diethylsilane,[69] but a later study showed that this process proceeds by a pulsed CVD mechanism.[70] Indirect routes to copper films have included reduction of ALD CuO by isopropanol,[71] reduction of ALD Cu_3N with H_2,[72] and reduction of ALD Cu_2O by formic acid in conjunction with a ruthenium seed layer.[73] Finally, plasma-based ALD processes include $Cu(acac)_2$/hydrogen plasma[74] and $Cu(dmap)_2$/hydrogen plasma.[75] Problems with existing copper ALD processes include high growth temperatures, lack of self-limited growth in some of the systems, low reactivity of the copper precursors toward the reducing co-reagents, incorporation of unwanted elements (Zn), and possible substrate damage and low conformal coverage in plasma processes.

Chart 5. Selected copper precursors for ALD and CVD.

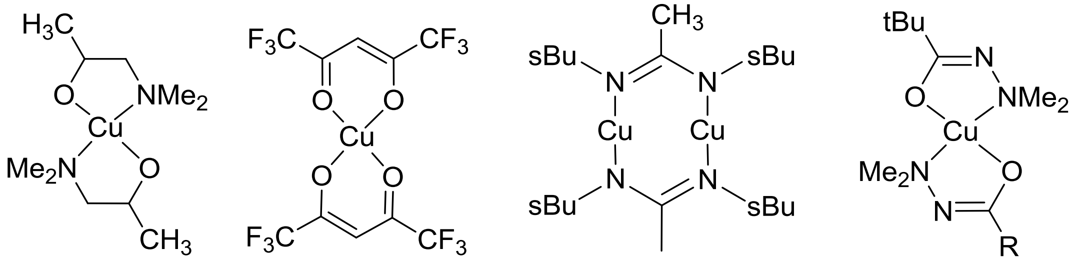

Cu(dmap)$_2$ **Cu(hfac)$_2$** **[Cu(sBuNC(Me)NsBu)]$_2$** **Cu(OCtBuNNMe$_2$)$_2$**

1.5 Thesis Problem

As stated previously, there are many current and future applications for thin films containing first-row transition metal elements.[4] ALD has been proposed as the primary deposition technique for the manufacturing of future microelectronic devices due to its inherit ability to provide thin films with absolute surface conformality and thickness control.[10] Unfortunately, there is a limited quantity of existing first-row transition metal precursors that have the requisite high thermal stability, reactivity, and vapor pressure suitable for ALD film growth to occur. These desired properties contribute to the lack of suitable transition metal precursors available. As a result, new first-row transition metal ALD precursors with optimal properties must be developed and tested to allow broad application of the ALD technique. An increase in thermal stability and volatility relative to existing ALD precursors can decrease impurity content and lead to lower deposition temperatures. These features can allow for the growth of smooth and continuous metallic films.

The thesis objective is to develop new ALD precursors and processes that afford thin films of high purity chromium, manganese, iron, cobalt, nickel, and copper metal thin films. These processes should obey the self-limited ALD growth mechanism over the widest possible temperature range to meet future microelectronics and other manufacturing requirements. In addition, the metals should be deposited at the lowest possible temperatures (ideally ≤ 100 °C) to afford the smallest surface roughnesses, promote facile nucleation, and give continuous films even at thicknesses of a few nanometers. To meet these goals, highly volatile precursors with the highest possible thermal stabilities are required. The aim is to synthesize and structurally characterize new transition metal complexes containing various substituents that promote volatility, thermal stability, and appropriate reactivity. The thermal stability and volatility of the complexes will be assessed by TGA/DTA, solid state decomposition determinations, and preparative sublimations. ALD growth studies of manganese, cobalt, nickel, and copper will be performed using newly-developed precursors and studied by varying film growth parameters. The composition and surface morphology of the films will be assessed using X-ray photoelectron spectroscopy (XPS), X-ray diffraction (XRD), elastic recoil detection analysis (ERDA), atomic force microscopy (AFM), scanning electron microscopy (SEM), and four-point probe resistivity.

CHAPTER 2

Volatility and High Thermal Stability in Mid- to Late-First-Row Transition-Metal Diazadienyl Complexes

2.1 Introduction

Nitrogen ligands are of special interest in the design of ALD precursors, since the metal-nitrogen bonds are often highly reactive. In addition, the absence of oxygen within the ligand framework makes these complexes particularly attractive since oxygen atoms can potentially be incorporated into metallic films. However, the challenge is to identify nitrogen-containing ligand systems that can also lead to volatile and highly thermally stable complexes. Recently, 1,4-diaza-1,3-butadienes (RN=CR'CR'=NR, R = alkyl, aryl, R' = H, alkyl) have been investigated as ligands, especially for the mid to late first row transition metals.[76-80] Most complexes discussed are of high molecular weight (> 500 g/mol) and are therefore not volatile. These ligands are redox non-innocent, and can exist in three distinct forms (Figure 8).[77-80] Form A is neutral with a long carbon-carbon distance and short carbon-nitrogen distances, form B is a monoanionic, delocalized radical anion with intermediate carbon-carbon and carbon-nitrogen distances, and form C is formally dianionic with a short carbon-carbon distance and long carbon-nitrogen distances. These ligands can form square planar to distorted tetrahedral complexes with chromium(II),[77] manganese(II),[78] iron(II),[79] cobalt(II),[80] and nickel(II) ions[80] and could potentially lead to thermally stable and volatile complexes that are useful for CVD or ALD. The redox nature of these systems may prove useful in forming a wide combination of transition metal complexes.

Figure 8. Redox non-innocent nature of α-diimine ligands.

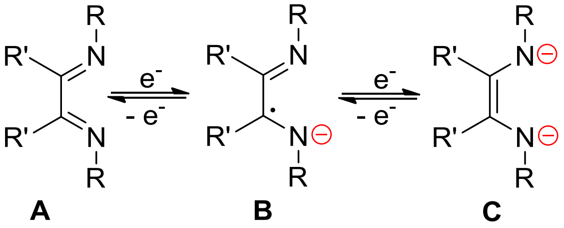

In this chapter, the synthesis, structure, volatility, thermal stability, and thermal decomposition of a series of chromium(II), manganese(II), iron(II), cobalt(II), and nickel(II) complexes that contain 1,4-di-*tert*-butyl-diaza-1,3-butadienyl (tBu_2DAD) ligands are reported. These complexes sublime at low temperatures and have high solid state decomposition temperatures, which highlight the potential application of these complexes as ALD or CVD precursors. In addition, these transition metal complexes self-decompose to their respective metal foils upon heating, a unique attribute that may prove useful in developing new CVD processes.

2.2 Results and Discussion

Synthetic Aspects. Treatment of anhydrous metal(II) chlorides (MCl_2, M = Cr, Mn, Fe, Co, Ni) with two equivalents of 1,4-di-*tert*-butyl-diaza-1,3-butadiene and two equivalents of lithium metal afforded complexes of the formula $M(tBu_2DAD)_2$ as purple (**1**), black (**2**), brown (**3**), blue (**4**), and dichroic red/green (**5**) crystalline powders (Figure 9). Crystalline samples of **1-5** were subsequently obtained either by sublimation or crystallization in hexane at -23 °C. The synthetic procedure is a modification of previous routes to transition metal complexes containing 1,4-diaza-1,3-butadiene ligands.[77-80] It was not possible to prepare any copper(II) or copper(I) complexes containing tBu_2DAD ligands, since all reactions afforded copper powders. The compositions of **1-5** were determined by a combination of analytical and spectroscopic techniques, and by X-ray crystal structure determinations of **1** and **3-5**. Complex **5** is the only diamagnetic species in the series, and revealed *tert*-butyl and imino hydrogen atom resonances at δ 1.93 and 8.95, respectively, in the ^{1}H NMR spectrum in benzene-d_6. In the infrared spectra of **1-5**, the carbon-nitrogen stretching frequencies were observed between 1716 and 1698 cm^{-1}. Solid state magnetic moments for **1-4** were 2.83, 3.85, 2.88, and 1.75 BM, respectively. Very similar values were measured in benzene solution using the Evans method, suggesting similar molecular structures in the solid state and solution. The magnetic moments for **1-4** are very close to those expected for high spin M(II) ions that are antiferromagnetically coupled to two unpaired electrons of radical anion tBu_2DAD ligands (Figure 8, form B). Analogous magnetic coupling is well established in transition metal complexes containing 1,4-diaza-1,3-butadiene radical anion ligands with various alkyl and aryl substituents.[76-80] Complexes **3**[79e] and **5**[80e] have been previously reported, and **4** was studied theoretically.[80g] The solution state magnetic moment reported for **3** in benzene solution was 2.88 BM,[79e] which is very similar to the values of 2.88 and 2.68 BM that were observed herein for the solid state and benzene solution magnetic moments, respectively. The ^{1}H NMR spectrum previously reported for **5** exactly match that reported herein.[80e]

Figure 9. Synthesis of transition metal diazadienyl complexes.

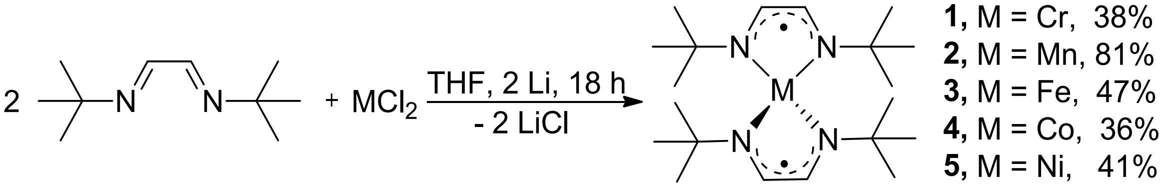

Structural Aspects. The X-ray crystal structures of **1** and **3-5** were determined to establish their solid-state configurations. Despite multiple attempts, high quality crystals of **2**

could not be obtained, although a low resolution X-ray structure revealed a monomeric, tetrahedral complex with a molecular arrangement similar to those of **3-5**. Experimental crystallographic data are summarized in Table 4, selected bond lengths and angles are given in Tables 2 and 3, and perspective views are presented in Figures 10-13.

Complexes **1** and **3-5** adopt mononuclear structures, with distorted tetrahedral geometry about the metal centers. In **3-5**, the planes of the C_2N_2 ligand cores are constrained by symmetry to be orthogonal. Complex **1** crystallizes with two independent molecules in the unit cell; both molecules are identical within experimental error. Complexes **3-5** are isostructural. The metal-nitrogen bond lengths (**1**, 1.924(2)-1.934(2) Å; **3**, 1.952(1)-1.956(1) Å; **4**, 1.929(1)-1.936(1) Å; **5**, 1.916(1)-1.919 Å) fall into a narrow range. The metal-nitrogen bond distances in **1** are considerably shorter than those found in Cr(2,6-$iPr_2C_6H_3N{=}CHC(Me){=}NC_6H_3$-2,6-$iPr_2)_2$ (2.019(1), 2.030(1) Å)[77a] and Cr(2,6-$iPr_2C_6H_3N{=}CHCH{=}NC_6H_3$-2,6-$iPr_2)_2$ (2.030(4), 2.035(5) Å),[77b] but are similar to the values observed in Cr_2(2,6-$iPr_2C_6H_3N{=}CHCH{=}NC_6H_3$-2,6-$iPr_2)_2$ (1.914(2), 1.913(2) Å).[77c] The metal-nitrogen bond distances in **3** are similar to those of $Fe(C_6F_5N{=}C(Me)C(Me){=}NC_6F_5)_2$ (1.962(2), 1.962(2) Å),[79c] but are shorter than those found in Fe(2,6-$iPr_2C_6H_3N{=}C(Me)C(Me){=}NC_6H_3$-2,6-$iPr_2)_2$ (1.988(9)-2.077(8) Å).[79d] $Fe(C_6F_5N{=}C(Me)C(Me){=}NC_6F_5)_2$ is proposed to contain two diazadienyl radical anion ligands, based upon the carbon-carbon and carbon-nitrogen distances of the ligand core.[79c] By contrast, one of the ligand core carbon-carbon distances in Fe(2,6-$iPr_2C_6H_3N{=}C(Me)C(Me){=}NC_6H_3$-2,6-$iPr_2)_2$ is about 0.08 Å longer than the other, suggesting more neutral character in one ligand (Figure 8, form C).[79d] The cobalt-nitrogen distances in **4** are similar to those of $Co(C_6F_5N{=}C(Me)C(Me){=}NC_6F_5)_2$ (1.931(3), 1.932(3) Å).[80c] The nickel-nitrogen bond lengths in **5** compare well with those of $Ni(C_6F_5N=C(Me)C(Me)=NC_6F_5)_2$ (1.9173(18), 1.9165(17) Å)[80c] and $Ni(2,6\text{-}Me_2C_6H_3N=CHC(Me)=NC_6H_3\text{-}2,6\text{-}Me_2)_2$ (1.921(1)-1.948(1) Å),[80a] but are shorter than those found in $Ni(2,6\text{-}iPr_2C_6H_3N=CHC(Me)=NC_6H_3\text{-}2,6\text{-}iPr_2)_2$ (1.963(2)-1.999(2) Å).[80a] Interestingly, the X-ray crystal structure of a polymorph of **5** was reported,[80d] and has nickel nitrogen bond lengths of 1.906 to 1.941 Å, with an average value of 1.923 Å.

Table 1. Selected bond lengths (Å) and angles (°) for **1**.

Cr1-N1	1.924(3)
Cr(1)-N(2)	1.924(2)
Cr(1)-N(3)	1.928(3)
Cr(1)-N(4)	1.934(2)
Cr(1)-C(1)	2.351(3)
Cr(1)-C(2)	2.361(3)
C(1)-C(2)	1.395(4)
C(11)-C(12)	1.337(5)
C(1)-N(1)	1.360(4)
C(2)-N(2)	1.356(4)
C(11)-N(3)	1.386(4)
C(12)-N(4)	1.367(4)
N(1)-Cr(1)-N(2)	91.79(11)
N(1)-Cr(1)-N(3)	127.13(11)
N(1)-Cr(1)-N(4)	118.60(11)
N(2)-Cr(1)-N(3)	123.99(11)
N(2)-Cr(1)-N(4)	114.94(11)
N(3)-Cr(1)-N(4)	82.91(11)
Cr(1)-N(1)-C(1)	89.69(19)
Cr(1)-N(2)-C(2)	90.38(18)
Cr(1)-N(3)-C(11)	112.1(2)
Cr(1)-N(4)-C(12)	112.2(2)

Figure 10. Perspective view of **1** with thermal ellipsoids at the 50% probability level.

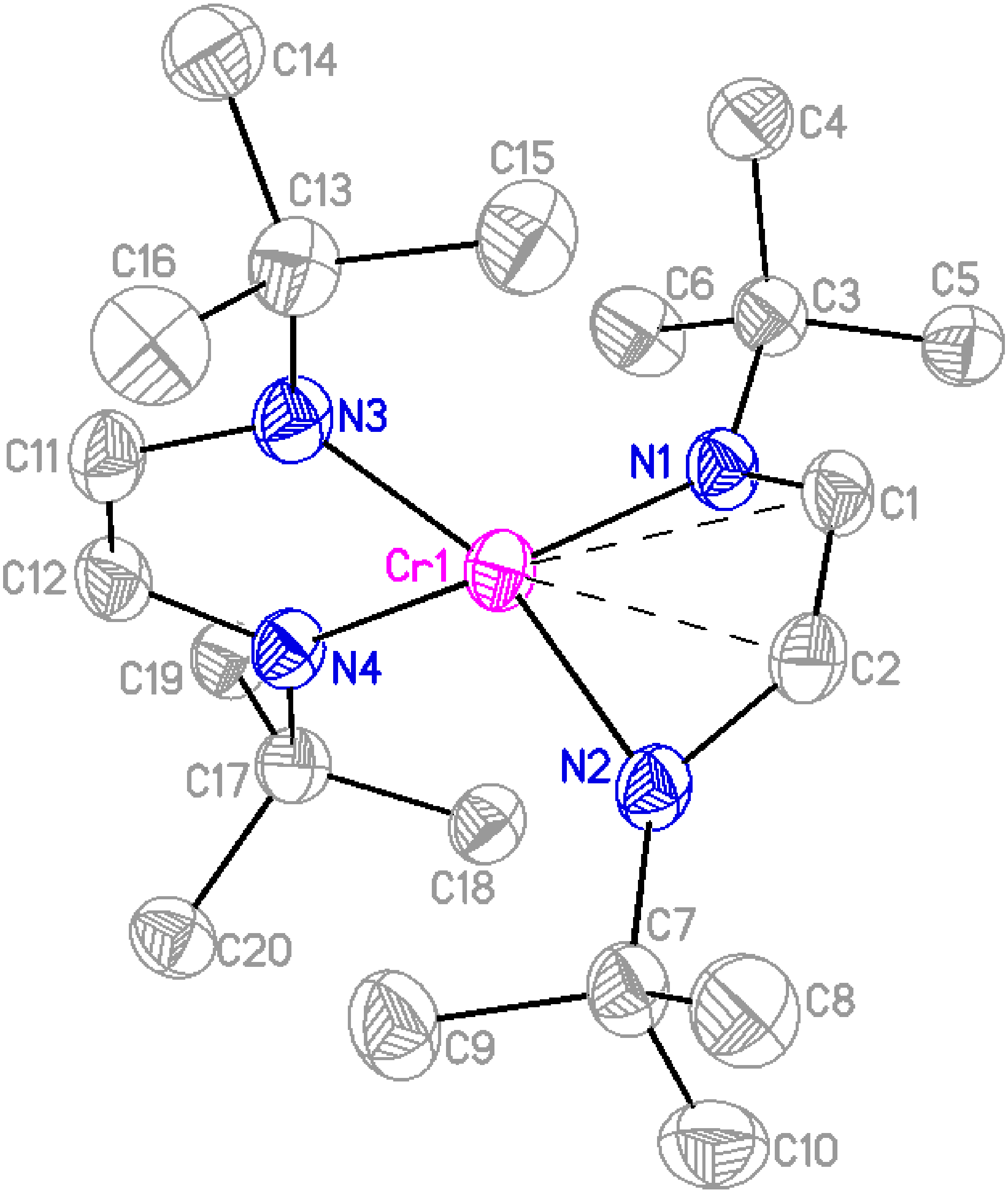

The average metal-nitrogen bond lengths follow the order **3** (1.954 Å) > **4** (1.932 Å) > **1** (1.928 Å) > **5** (1.917 Å), even though the ionic radii of the metal ions decrease in the order Cr(II) (0.80 Å) > Fe(II) (0.78 Å) > Co(II) (0.745 Å) > Ni(II) (0.69 Å).[81] Hence, the chromium-nitrogen distances in **1** are shorter than expected, based upon the ionic radius of the Cr(II) ion relative to those of the other ions. Closer inspection of **1** reveals that there are two types of tBu_2DAD ligands. The ligand that contains N(1) and N(2) has the C(1) and C(2) atoms tilted toward the chromium atom, with chromium-carbon distances of 2.351(3) and 2.361(3) Å. By contrast, the ligand containing N(3) and N(4) forms a planar CrN_2C_2 ring and has chromium-carbon distances of 2.758 and 2.767 Å. For comparison the metal-carbon distances associated with the tBu_2DAD core carbon atoms of **3-5** range between 2.706 and 2.727 Å and the metal ions are coplanar with the N_2C_2 rings. The chromium-carbon interactions in the ligand in **1** containing C(1) and C(2) appear to reflect the additional empty *d*-orbitals associated with the d^4 Cr(II) ion. The modified bonding to one of the ligands in **1** may alleviate interligand *tert*-butyl crowding by a small amount, thereby allowing slightly shorter chromium-nitrogen bond lengths than expected based upon the ionic radius of the Cr(II) ion.

It is well established that the carbon-carbon and carbon-nitrogen bond lengths within the C_2N_2 ligand cores offer a reliable tool for distinguishing among forms A, B, and C in Figure 8.[77-80] In **3-5**, the carbon-carbon and carbon-nitrogen bond lengths fall into the narrow ranges of 1.393 to 1.407 Å and 1.326 to 1.347 Å, respectively. These values are in between those expected for single and double bonds, and are diagnostic of the tBu_2DAD radical anion. These assignments are also consistent with the magnetic moment data described above. The situation with **1** is a little more complex, since one ligand has a carbon-carbon distance of

1.337(5) Å and carbon-nitrogen distances of 1.386(4) and 1.367(4) Å. The other ligand is bent toward the chromium ion and has a carbon-carbon distance of 1.395(4) Å and carbon-nitrogen distances of 1.360(4) and 1.356(4) Å. The bond distances of the latter ligand are very similar to those of **3-5**, and support assignment as a tBu_2DAD radical anion. In the former ligand, only the carbon-carbon bond length differs significantly within experimental error from that of the latter ligand. Hence, there may be a slightly higher amount of charge localization on the nitrogen atoms in the former ligand, but any differences in the structural data are small and at the edge of experimental uncertainty. The magnetic moment data for **1** described above are consistent with the presence of two tBu_2DAD radical anion ligands that are antiferromagnetically coupled to a high-spin d^4 Cr(II) ion. Complexes of the formula $FeCl_3(tBu_2DAD)$,[82a] $CoCl_2(tBu_2DAD)$,[82b] and $NiBr_2(tBu_2DAD)$[82c] have been structurally characterized, and have C_2N_2 ligand core carbon-carbon and carbon-nitrogen distances of 1.455-1.510 and 1.247-1.275 Å, respectively. The carbon-carbon distances in these complexes are close to those expected for a single bond, and the carbon-nitrogen distances are close to those expected for a double bond. Hence, these ligands are consistent with neutral form A in Figure 8, and are distinct from the radical anion ligand type B observed in **1** and **3-5**.

Table 2. Selected bond lengths (Å) and angles (°) for **3-5**.

	3	**4**	**5**
M-N(1)	1.952(1)	1.929(1)	1.919(1)
M-N(2)	1.956(1)	1.936(1)	1.916(1)
M-N(3)	1.953(1)	1.931(1)	1.917(1)
C(1)-C(2)	1.393(2)	1.393(2)	1.401(2)
C(9)-C(9)’	1.397(2)	1.403(2)	1.407(2)
C(1)-N(1)	1.339(2)	1.334(2)	1.326(2)
C(2)-N(2)	1.341(2)	1.332(2)	1.326(2)
C(9)-N(3)	1.347(1)	1.335(2)	1.330(1)
N(1)-M-N(2)	84.72(5)	84.65(6)	83.51(5)
N(1)-M-N(3)	122.74(3)	122.93(4)	123.93(3)
N(2)-M-N(3)	123.28(3)	123.26(4)	123.62(3)
N(3)-M-N(3)’	85.00(5)	84.77(6)	83.65(5)
M-N(1)-C(1)	110.18(10)	110.76(11)	112.33(10)
M-N(2)-C(2)	109.97(9)	110.61(11)	112.61(10)
M-N(3)-C(9)	110.07(6)	110.87(8)	112.55(7)

Table 3. Crystal data and data collection parameters for **1**, and **3-5**.

	1	**3**	**4**	**5**
Formula	$C_{20}H_{40}CrN_4$	$C_{20}H_{40}FeN_4$	$C_{20}H_{40}CoN_4$	$C_{20}H_{40}NiN_4$
FW	388.56	392.41	395.49	395.27
space group	P-1	Pnma	Pnma	Pnma
a (Å)	11.1969(10)	18.3813(8)	18.2363(8)	18.1617(7)
b (Å)	14.0988(13)	13.4195(6)	13.3810(6)	13.3739(5)
c (Å)	14.4001(14)	9.2799(4)	9.2410(4)	9.2280(4)
α (°)	86.857(2)			
β (°)	82.672(3)			
γ (°)	88.077(3)			
V ($Å^3$)	2250.5(4)	2289.05(17)	2254.99(17)	2241.41(15)
Z	4	4	4	4
T (K)	100(2)	100(2)	100(2)	100(2)
λ (Å)	0.71073	0.71073	0.71073	0.71073
ρ_{calcd} (g, cm^{-3})	1.147	1.139	1.165	1.171
μ (mm^{-1})	0.518	0.668	0.770	0.875
R(F) (%)	6.65	2.96	2.62	3.02
Rw(F) (%)	16.83	7.78	6.64	7.72

$R(F) = \Sigma||Fo|-|Fc||/ \Sigma|Fo|$, $R_w(F)^2 = [\Sigma w(Fo^2-Fc^2)^2/ \Sigma w(Fo^2)^2]^{1/2}$ for $I > 2\sigma(I)$

Figure 11. Perspective view of **3** with thermal ellipsoids at the 50% probability level.

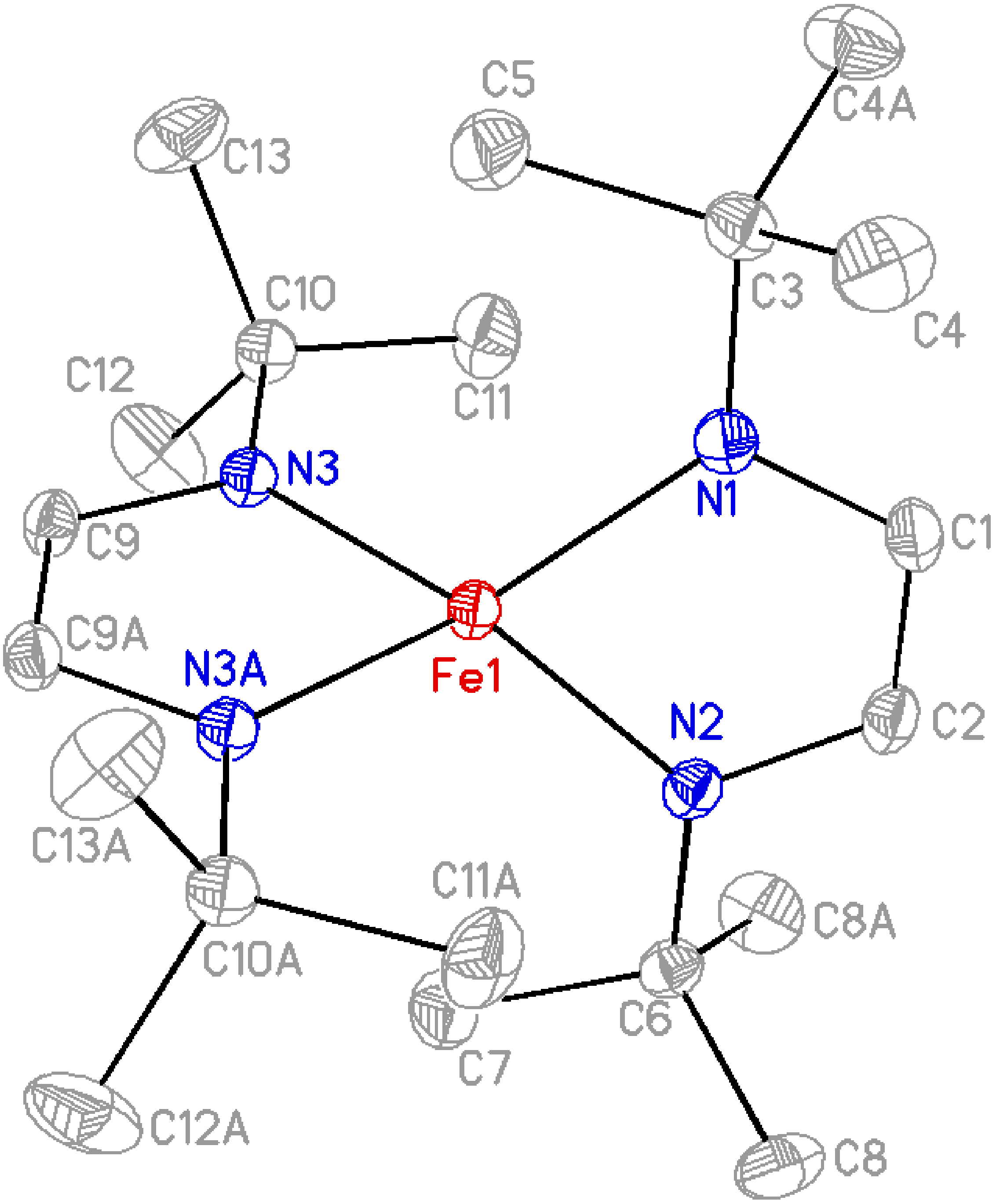

Figure 12. Perspective view of **4** with thermal ellipsoids at the 50% probability level.

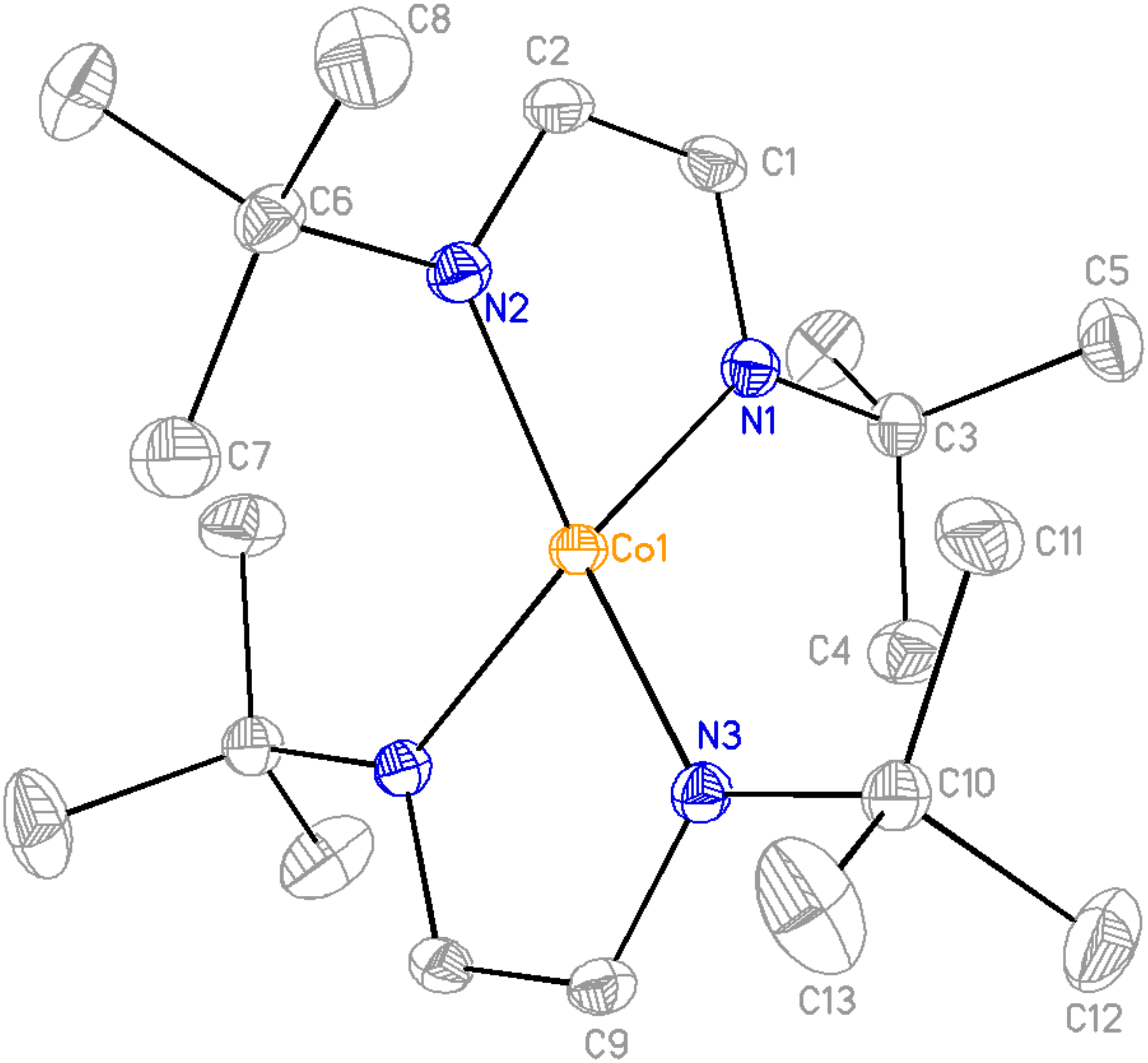

Figure 13. Perspective view of **5** with thermal ellipsoids at the 50% probability level.

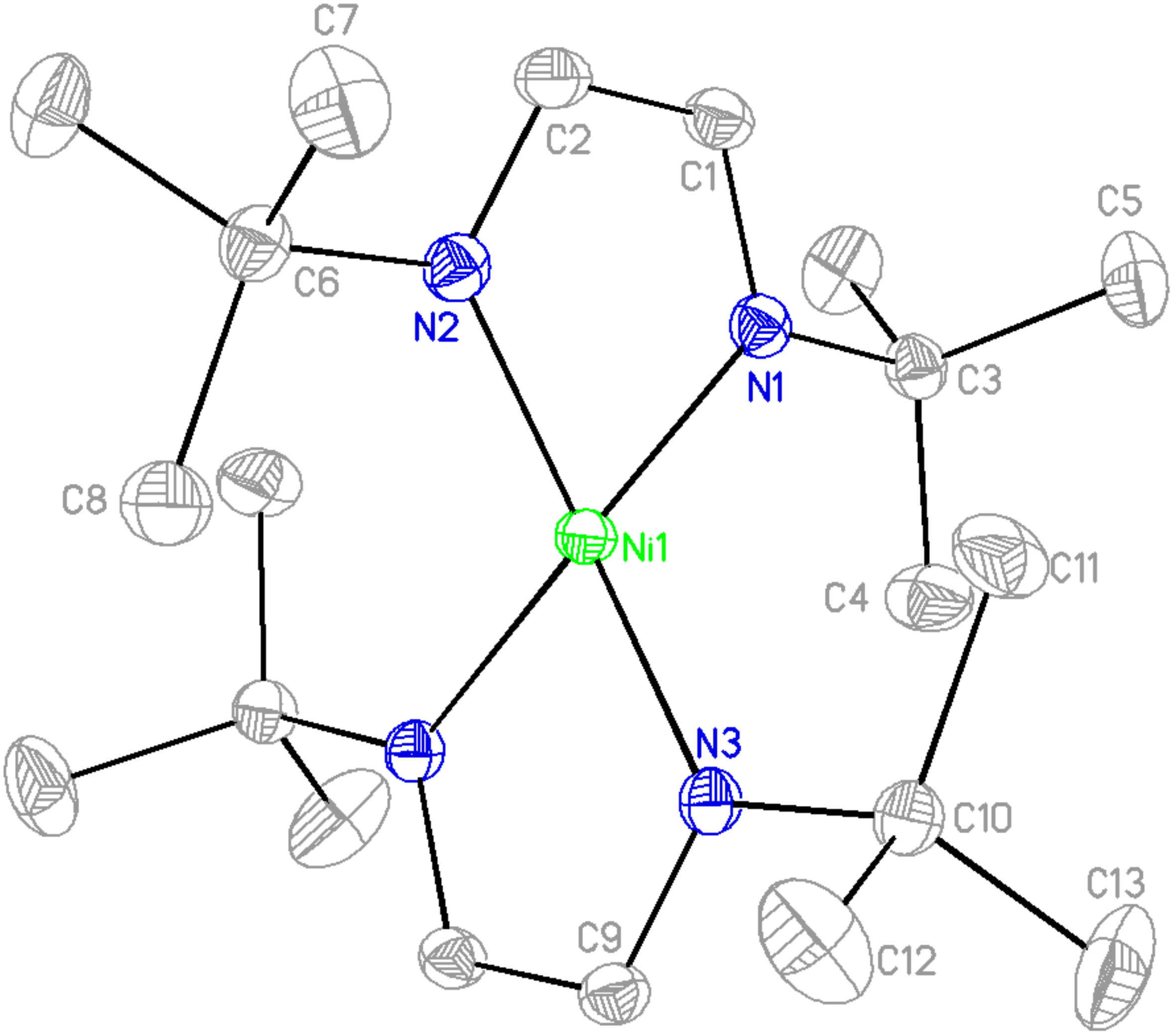

Volatility and Thermodynamic Stability Study. The volatility and thermal stability of **1-5** were studied by preparative sublimation, thermogravimetric analyses, and melting point/solid state thermal decomposition experiments to assess their potential for use as ALD precursors. Sublimation data, melting points, and solid state decomposition temperatures for **1-5** are listed in Table 4. In preparative sublimations, 0.5-1.0 g samples were sublimed at 0.05 Torr and the temperature was adjusted so that the sublimation was complete in less than five hours. In previous work, we have established that these preparative sublimation temperatures approximate the temperatures required for the vapor phase delivery of precursors in our ALD reactors.[83] Under these conditions, the sublimed recoveries of **1-5** were ≥ 92.3% with nonvolatile residues of ≤ 6.9%. The high air sensitivity of **1-5** limited the ability to obtain higher sublimed recoveries, since product isolation had to be conducted in an inert atmosphere dry box. Additionally, exposure to trace amounts of air during sample loading may have led to higher nonvolatile residues.

Table 4. Sublimation Temperature, Melting Point, Solid State Decomposition Temperature, Percent Recovery, and Percent Nonvolatile Residue for **1-5**.

Complex	Sublimation Temperature (°C/0.05 Torr)	Melting Point (°C)	Solid State Decomposition Temperature (°C)	% Recovery	% Nonvolatile Residue
1	85	95	295	96.7	3.2
2	120	155-157	325	95.0	4.3
3	115	132-134	260	96.1	3.4
4	115	174-175	235	94.7	5.2
5	115	184-185	230	92.3	6.9

The solid state decomposition temperatures were determined visually by monitoring sealed glass capillary tubes containing a few milligrams of **1**-**5**, and then noting the temperatures at which metal foils began to appear. These solid state decomposition temperatures are generally very close to the upper limit of self-limited ALD growth in plots of growth rate versus deposition temperature,[83] and are thus very useful. The solid state decomposition temperature of **2** is the highest at 325 °C, while that of **5** is the lowest at 230 °C. Interestingly, a plot of the solid state decomposition temperatures of **1**-**5** versus the $M^{2+}\rightarrow M^0$ reduction potentials[84] is linear (Figure 14), suggesting that decomposition might occur through transfer of an electron from the tBu_2DAD radical anion ligands to the metal ions. The failure to produce copper(II) or copper(I) complexes noted above likely arises from immediate reduction of the copper ions to copper metal, due to the large positive reduction potentials of these ions (Cu^{2+} 0.342 V, Cu^+ 0.521 V).[84]

Figure 14. Comparison of the solid-state decomposition temperatures of **1**-**5** versus the M^{2+}/M^0 redox couple.

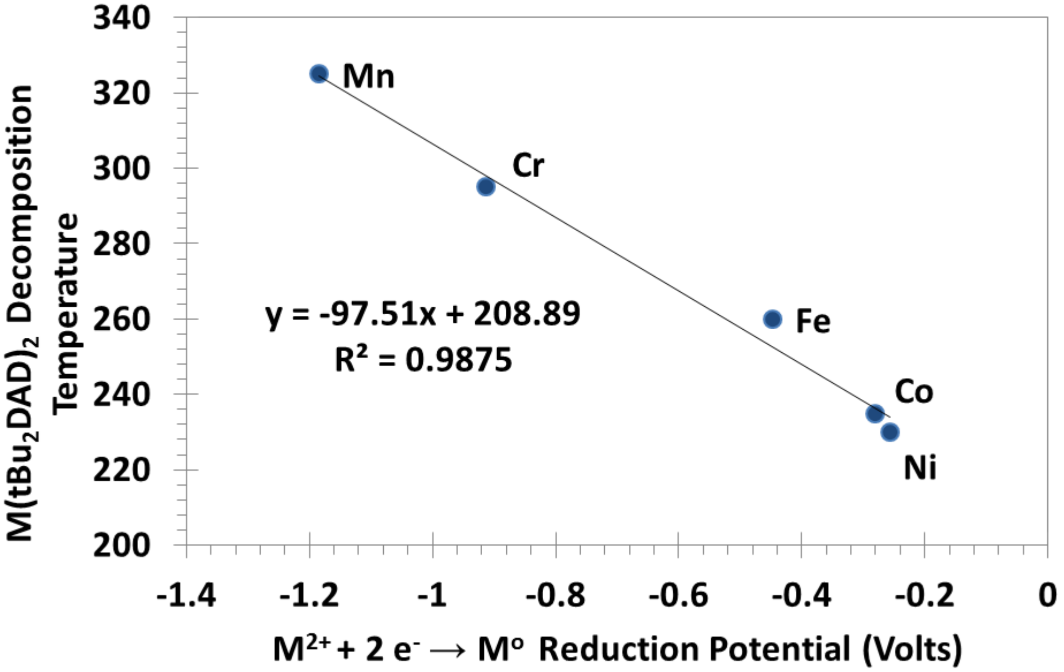

Thermogravimetric analyses (TGA) were performed on **1-5** to understand their volatilities and thermal stabilities (Figure 15). These analyses were carried out with an instrument that was contained in a high-purity nitrogen-filled glove box to minimize decomposition arising from exposure to air. Complexes **1-5** have similar TGA traces with single step weight losses occurring between 150 and 225 °C. The residues upon reaching 500 °C were all ≤ 3.6%. Complex **2** is the most air sensitive compound in the series, and its TGA traces always showed 10-20% weight losses between 50 and 150 °C that were presumably due to reaction with ambient oxygen or water, in spite of multiple runs and utmost care to maintain a high purity nitrogen atmosphere.

Figure 15. Thermogravimetric analysis traces of **1-5** from 50 to 550 °C at 10 °C/min.

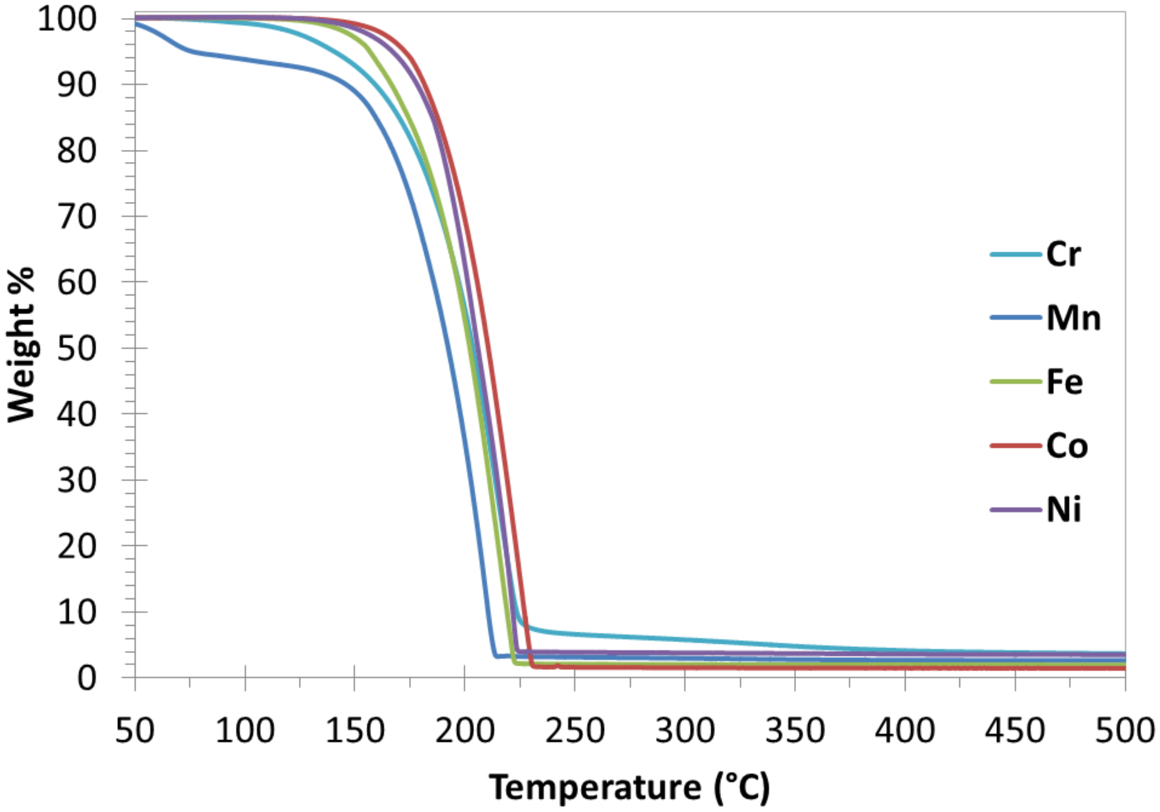

Vapor pressure measurements were carried out on **2** and **5** using a previously reported method and apparatus (Figures 16 and 17).[85] The vapor pressure of **2** obeys the equation $\mathrm{Log}_{10}\mathrm{P(mTorr)} = 12.753 - 3631/\mathrm{T(K)}$, whereas the equation for **5** is $\mathrm{Log}_{10}\mathrm{P(mTorr)} = 13.983 - 3986/\mathrm{T(K)}$. The vapor pressures of **2** and **5** at 115 °C are 2.48 and 5.13 Torr, respectively. The vapor pressures of **1**, **3**, and **4** should be close to those of **2** and **5**, since the preparative sublimation temperatures of **1-5** are similar.

Figure 16. Vapor pressure measurement of **2**.

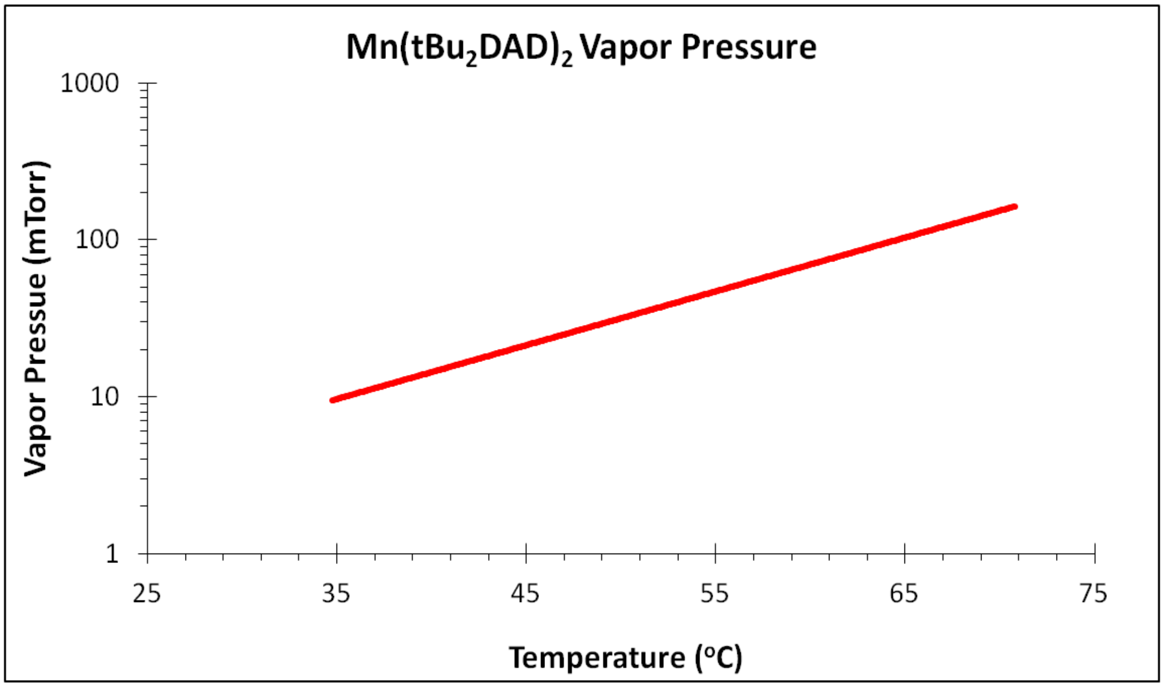

Figure 17. Vapor pressure measurement of **5**.

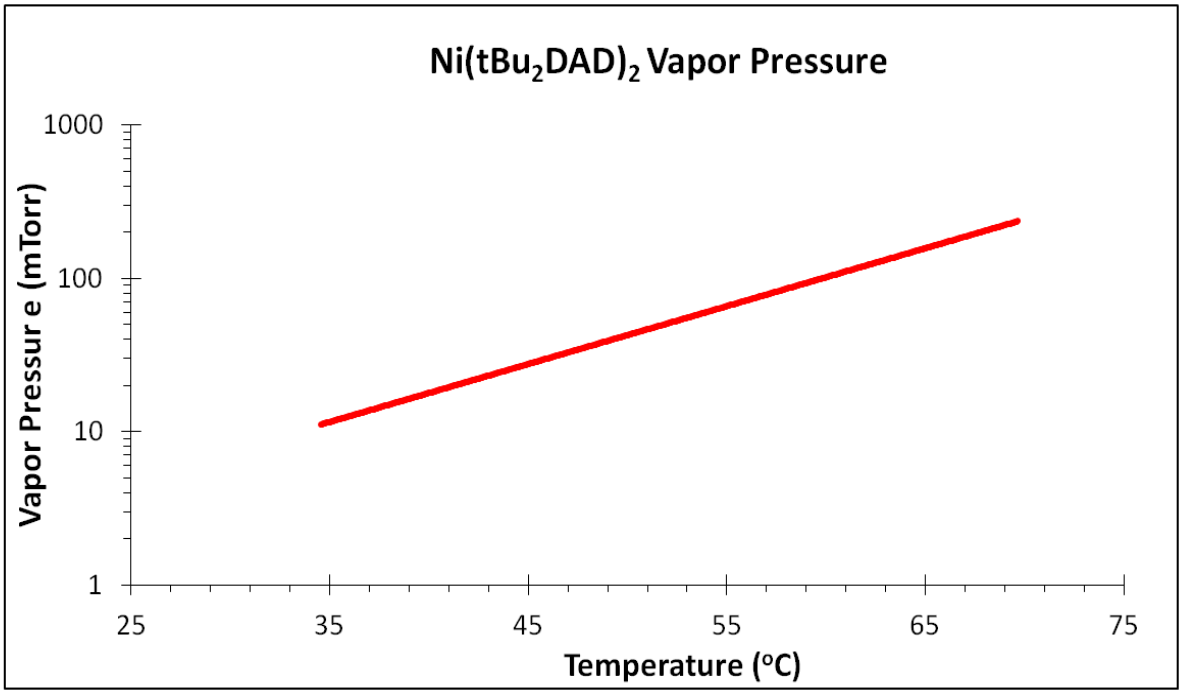

As described above, solid state decompositions of **1**-**5** afforded shiny metallic foils as products. The rationale behind this result is presumably due to the recombination of the two radicals with the M^{2+} metal center to form M^0 and neutral diazadiene. This process can be summarized in Figure 18 below.

Figure 18. Self-reduction of transition metal diazadiene complexes.

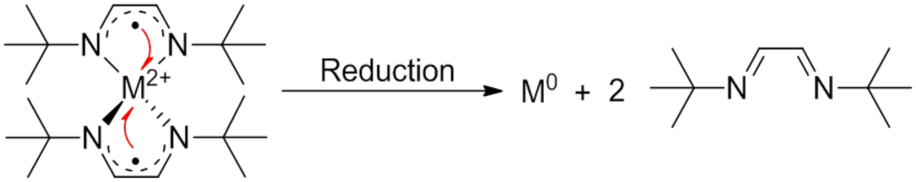

To verify the formation of the metals, preparative scale solid state thermolyses were carried out on **1**-**5** as described in the Experimental Section and the residues were analyzed by X-ray powder diffraction. X-ray diffraction analyses demonstrated that **1** and **3**-**5** afford crystalline, shiny gray-black powders of the metals. Figure 19 shows the X-ray diffraction pattern of the chromium metal thermolysis product from **1**, which matches the JCPDS 06-0694 reference pattern for chromium metal. The X-ray diffraction patterns of the powders derived from **3-5** are contained in Figures 19-22. The thermolysis product of **2** was also a shiny metallic powder. The X-ray diffraction pattern of the thermolysis product obtained under conditions similar to those used for the thermolysis of **1** and **3-5** showed weak reflections that were consistent with Mn_3O_4 (JCPDS 04-07320).[86] Since it was possible that the Mn_3O_4 formed upon oxidation of manganese metal by residual oxygen or water in the argon used in the thermolysis experiment, the thermolysis of **2** was repeated under a vacuum of 0.05 Torr at 375 °C for one hour. X-ray diffraction spectra of the resulting gray-black metallic powder did not show any reflections, suggesting an amorphous product. Treatment of the powders resulting from the thermolysis of **2** with 30% aqueous hydrogen peroxide led to vigorous reaction and gas evolution. Similar reactivities were observed for the powders resulting from thermolysis under flowing argon and under vacuum. For comparison, manganese metal powder reacted in a similar vigorous manner with 30% aqueous hydrogen peroxide, whereas commercial Mn_3O_4 powder was inert under the same conditions. The commercial Mn_3O_4 powder was crystalline and indexed as Hausmannite (JCPDS 24-0734), and is thus in a different crystalline form from the powder described above that was obtained upon thermolysis of **2**. However, the reactivity of both forms of Mn_3O_4 toward 30% hydrogen peroxide should be similar. Hence, it is possible that thermolysis of **2** affords amorphous manganese metal powder.

Figure 19. X-ray diffraction pattern of chromium metal powder obtained upon thermolysis of **1**.

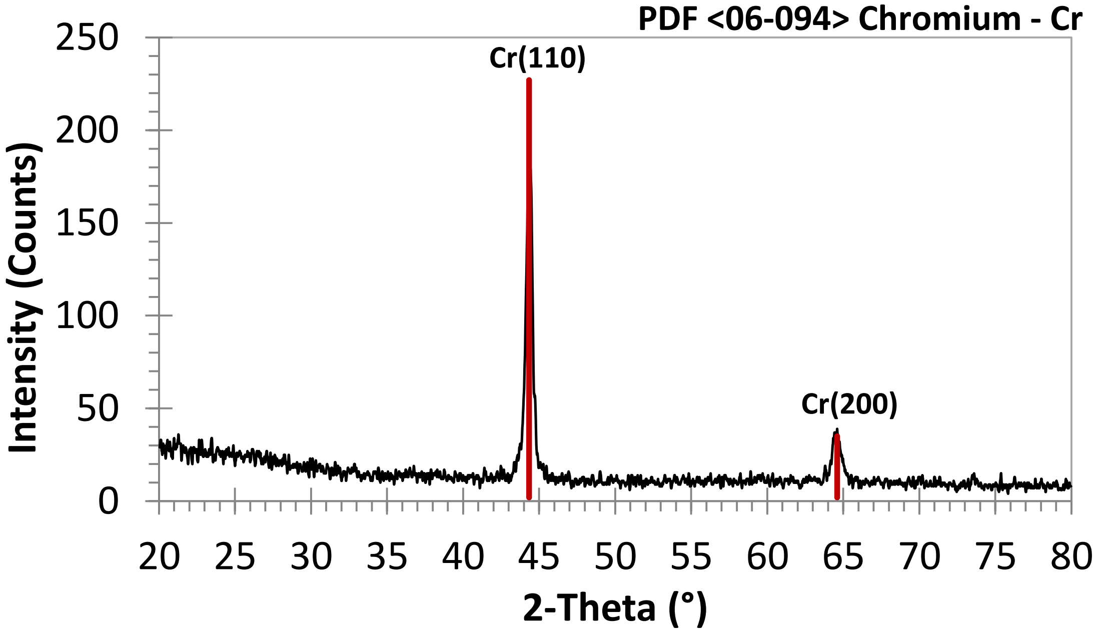

Figure 20. X-ray diffraction pattern of iron metal powder obtained upon thermolysis of **3**.

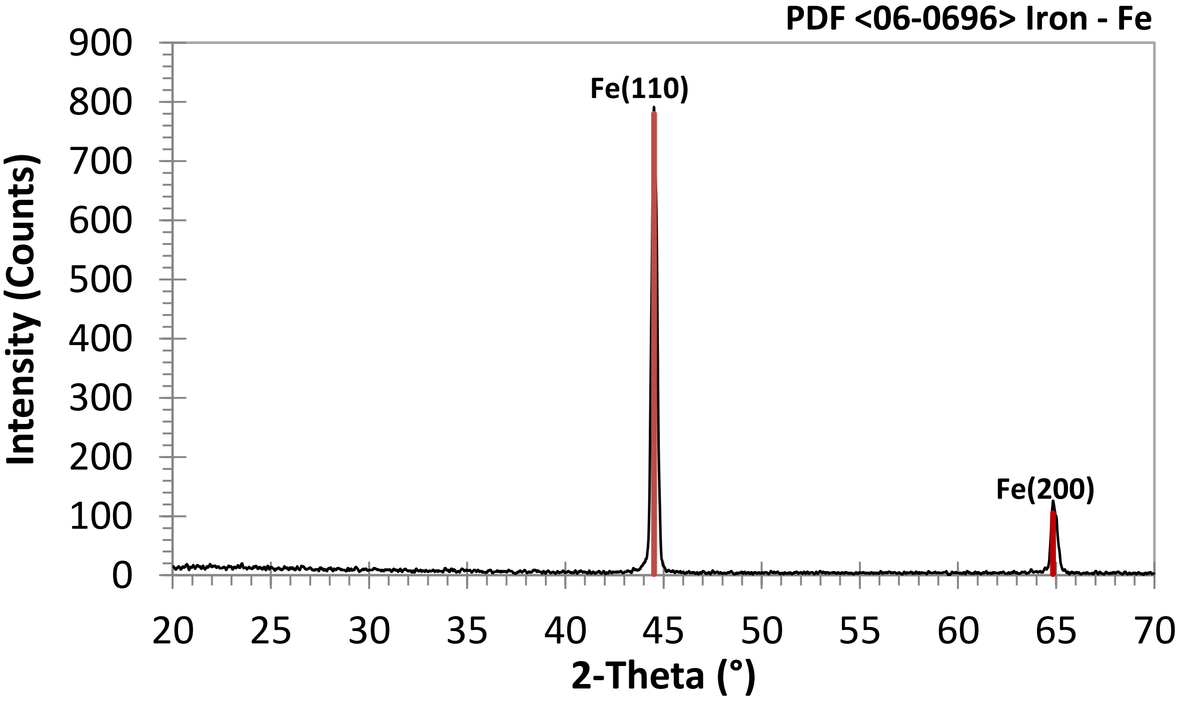

Figure 21. X-ray diffraction pattern of cobalt metal powder obtained upon thermolysis of **4**.

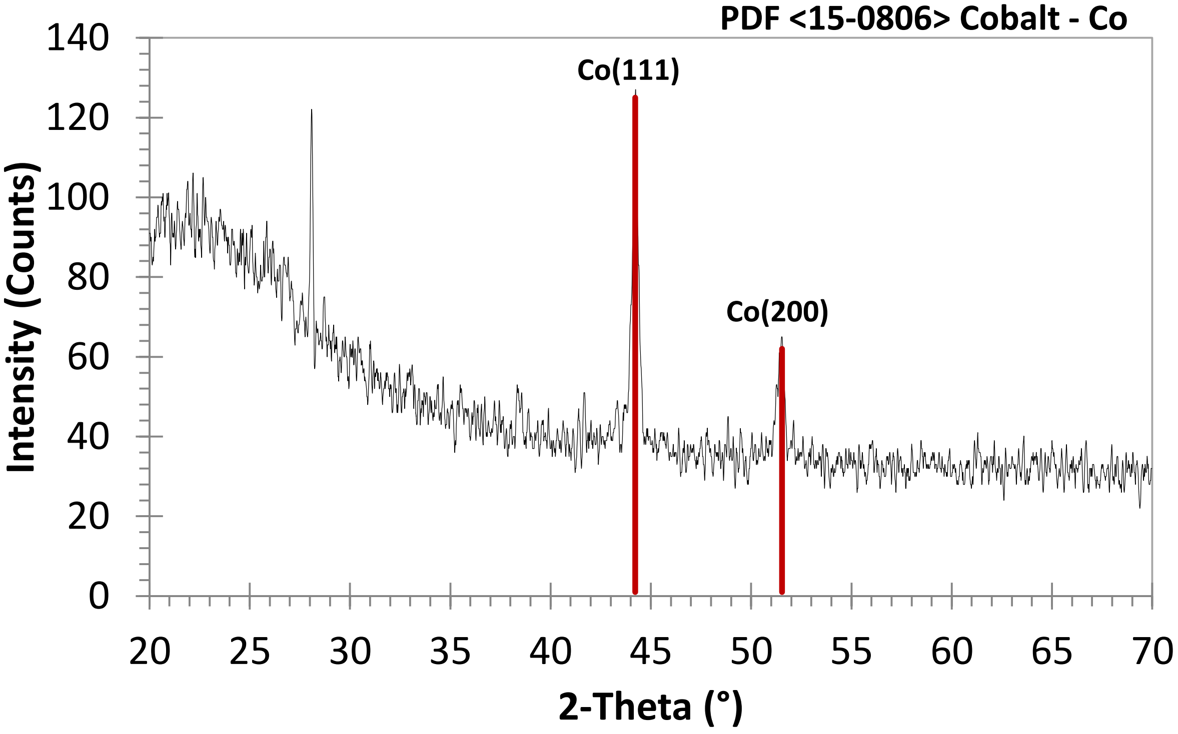

Figure 22. X-ray diffraction pattern of nickel metal powder obtained upon thermolysis of **5**.

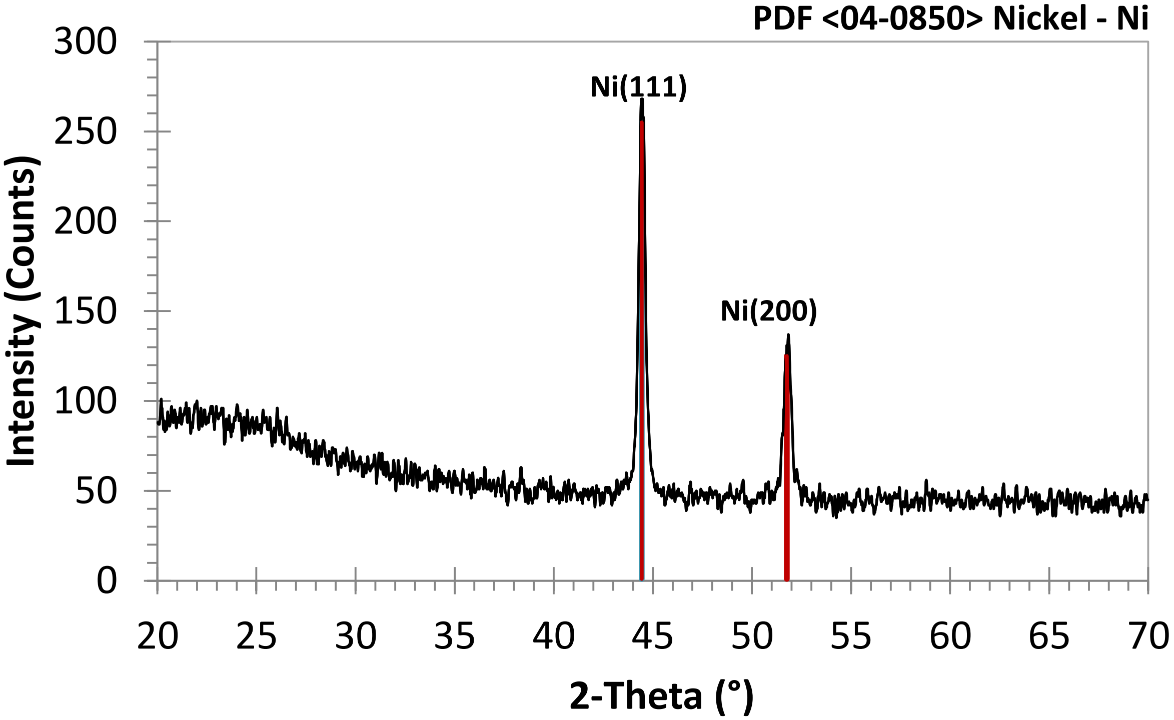

Solution Screening Studies. Solutions reactions are a powerful tool in ALD process development. Such experiments entailing promising ALD precursors and reducing agents provide a powerful and efficient means of discovering suitable combinations for thin film growth. In addition, solution reactions can allow one to probe the mechanistic details of a particular ALD process since their products may be susceptible to characterization techniques such as NMR, IR, and powder XRD studies. Metal ALD process development can benefit from such studies since most solution reactions will occur < 100 °C and the desired product (metal) is insoluble in most solvents. The insoluble precipitate can then be collected and subjected to XRD studies to verify the presence of crystalline metal. Solution reaction studies have been used in CVD/ALD process development for many metals including Cu,[86] Ti,[87] Pt,[88] and Pd.[89] In the solution screening study for a Cu(II) aldiminate complex, several mechanistic conclusions were developed to rationalize formation of Cu metal from several reducing agents including $ZnEt_2$, $AlMe_3$, and BEt_3.[86] A follow up paper from the same group investigated the ALD process development of Cu metal film growth from successful solution reactions.[63] Hence, this work illustrates the significance and understanding achieved performing solution screening studies to scout new metal ALD processes.

To demonstrate initial evidence of metal formation in solution, transition metal diazadiene complexes were treated with volatile reducing agents in solution to demonstrate viable reduction to the metal. In these studies, 500 mg of the transition metal diazadiene complex was dissolved in 10 mL of THF under inert conditions. Subsequently, the respective reducing agent was added in excess (5 molar equivalents) slowly upon vigorous stirring. Initial evidence of metal formation would involve violent gas evolution and formation of a black, non-soluble metallic precipitate. If metal or gas formation was not initially evident, the solutions were placed under refluxing conditions for 5 h. The solutions then would be cooled down to ambient temperature, filtered and precipitate collected. Retrieved residues then would be subject to powder XRD studies to verify the presence of metal. The summary of these results can be seen in Table 5.

Table 5. Solution reaction results of complexes **1-5**.

Reducing Agent:	**1**	**2**	**3**	**4**	**5**
$H_3B{\cdot}NEt_3$	No reaction	No reaction	No reaction	No reaction	No reaction
$H_3B{\cdot}NHMe_2$	No reaction	No reaction	No reaction	No reaction	No reaction
$H_3B{\cdot}SMe_2$	No reaction	Color Change; No precipitate	No reaction	No reaction	No reaction
$AlMe_3$	Gray Precipitate; Amorphous	Gray Precipitate; Amorphous	Gray Precipitate; Amorphous	Gray Precipitate; Amorphous	Gray Precipitate; Amorphous
$AlEt_3$	Gray Precipitate; Amorphous	Gray Precipitate; Amorphous	Gray Precipitate; Amorphous	Gray Precipitate; Amorphous	Gray Precipitate; Amorphous
$ZnEt_2$	Gray Precipitate; Amorphous	Gray Precipitate; Amorphous	Gray Precipitate; Amorphous	Gray Precipitate; Amorphous	Gray Precipitate; Amorphous
$HSiEt_3$	No reaction	No reaction	No reaction	No reaction	No reaction
H_2SiEt_2	No reaction	No reaction	No reaction	No reaction	No reaction
H_2NNMe_2	Color Change; No precipitate	Color Change; No precipitate	Color Change; No precipitate	Color Change; No precipitate	Color Change; No precipitate
Aqueous N_2H_4	Color Change; No precipitate	Color Change; No precipitate	Color Change; No precipitate	Color Change; No precipitate	Color Change; No precipitate

In summary, no reaction combination resulted in metal formation. In particular, amine-borane complexes ($H_3B{\cdot}NEt_3$, $H_3B{\cdot}NMe_2$, $H_3B{\cdot}SMe_2$) and silanes ($HSiEt_3$, H_2SiEt_2) did not induce color change or precipitate formation upon addition. The main-group metal alkyl complexes ($AlMe_3$, $AlEt_3$, $ZnEt_2$) upon addition produced a gray precipitate followed by total loss of color to the reaction mixture. Powder XRD analysis of residues in this series revealed a complex sequence of reflections suggestive of oxide formation or metal alloying with Zn or Al. Reduction reactions involving hydrazine (N_2H_4) and 1,1-dimethylhydrazine (H_2NNMe_2) lead to an immediate color change to the precursor with no precipitate observed suggesting hydrazine adduct formation. These newly formed adducts are stable under refluxing conditions as there was no evidence of darkening or metal formation after 5 h. Failure to demonstrating metal reduction through the above scouting reactions is presumably due to the lack of reducing power of the selected reducing agents.

Evaluation of Precursor Properties. Complexes **1-5** sublime at 85 (**1**) and 115-120 °C (**2-5**) with low nonvolatile residues, have high solid state decomposition temperatures, and are highly reactive toward ambient atmosphere. Additionally, **1** and **3-5** decompose to the metals upon thermolysis, and **2** may afford manganese metal upon thermolysis. These complexes thus have useful properties for applications as film growth precursors by ALD and CVD. Complexes **1** and **3-5** decompose thermally between 230 and 295 °C to afford the metals, and **2** decomposes at 325 °C possibly to afford manganese metal. Since **1-5** evaporate with low residues between 85 and 120 °C, they are highly likely to be useful CVD precursors to films of the metals. ALD precursors must be thermally stable at the film growth temperatures, or the self-limited ALD growth mechanism is lost and CVD-like growth occurs.[10] Complexes **1-5** also have properties that may be useful in ALD film growth, especially since they have high thermal decomposition temperatures compared to other available precursors for each metal. For example, the amidinate complex $Ni(iPrNC(Me)NiPr)_2$ decomposes at about 180 °C,[65a] compared to a solid state decomposition temperature of 235 °C for nickel complex **5**. The amidinate complexes Fe(tBuNC(Me)NtBu)$_2$ and Co(iPrNC(Me)NiPr)$_2$ exhibited single step weight loss events in the TGA traces, but had 12 and 9% nonvolatile residues, respectively, upon reaching 225 (Fe(tBuNC(Me)NtBu)$_2$) and 200 °C (Co(iPrNC(Me)NiPr)$_2$).[90a] These nonvolatile residues are higher than those observed in the TGA traces of **1**-**5** (< 3.6%), again suggesting that our new complexes have higher thermal decomposition temperatures than the analogous amidinate complexes. The increased thermal stabilities of **1**-**5** could allow wider temperature ranges of self-limited ALD film growth, relative to amidinate and other precursors with lower decomposition temperatures.

2.3 Conclusions

Transition metal complexes containing radical-anion diazadienyl ligands have been synthesized and structurally characterized, and their volatilities and thermal stabilities were assessed. Complexes **1** and **3-5** were structurally characterized, and exist as tetrahedral monomers in the solid-state. X-ray crystal structures and magnetic measurements are consistent with the ligand existing in the radical anion form. All complexes exhibit high thermal stabilities and volatilities, as demonstrated by the TGA traces, preparative sublimations, and melting point/decomposition determinations. Furthermore, all complexes decompose into metal powders upon decomposition, demonstrating promise as CVD film growth precursors.

2.4 Experimental Section

General Considerations. All manipulations were carried out under argon using either Schlenk or glove box techniques. Tetrahydrofuran was distilled from sodium benzophenone ketyl, and hexane was distilled from P_2O_5. Lithium metal was obtained from Acros Organics. Anhydrous transition metal chlorides ($CrCl_2$, $MnCl_2$, $FeCl_2$, $CoCl_2$, and $NiCl_2$) were obtained from Strem Chemicals Inc. and used as received. Manganese metal powder and Mn_3O_4 were obtained from Aldrich Chemical Company. $NiCl_2{\cdot}CH_3CN$[91] and 1,4-di-*tert*-butyl-1,3-diazabutadiene[92] were prepared according to literature procedures.

^1H and $^{13}C\{^1H\}$ NMR spectra were obtained at 400 and 100 MHz respectively in benzene-d_6 and were referenced to the residual proton and the ^{13}C resonances of the solvent. Infrared spectra were obtained using Nujol as the medium. Magnetic moments were determined in the solid state using a Johnson Mathey magnetic susceptibility apparatus, and in benzene solution using the Evans method.[93] Melting points were determined on a Thermo Scientific Mel-Temp 3.0 melting point apparatus and are uncorrected. X-ray quality crystals of **1** and **3-5** were grown from hexane at -23 °C. Preparative sublimations and solid state decomposition temperatures were determined using previously described procedures.[83e] Thermogravimetric analyses were performed in a nitrogen filled glovebox on a TA Instruments Q500 equipped with an evolved gas analysis furnace with samples heated at a rate of 10 °C/min. Elemental analyses were performed by Midwest Microlab, Indianapolis, Indiana. Powder X-ray diffraction data was acquired on a Rigaku RU200B diffractometer with a Cu Kα rotating anode. Crystalline phases were identified by comparison of the experimental patterns with the powder diffraction files of the International Center of Diffraction Data using the Jade 5.0 software package.

Preparation of Bis(1,4-di-*tert*-butyl-1,3-diazabutadienyl)chromium(II) (1). A 100 mL Schlenk flask, equipped with a magnetic stir bar and a rubber septum, was charged with 1,4-di-*tert*-butyl-1,3-diazabutadiene (1.000 g, 5.94 mmol) and tetrahydrofuran (20 mL). To this stirred solution at ambient temperature was slowly added freshly cut lithium metal (0.042 g, 6.000 mmol) and the resultant dark brown solution was stirred for 6 h. This solution was then added dropwise by cannula over a 30 min period to a stirred suspension of anhydrous chromium(II) chloride (0.365 g, 2.970 mmol) in tetrahydrofuran (40 mL). The resultant deep purple solution was stirred for 6 h at ambient temperature. The volatile components were then removed under reduced pressure and the resultant dark purple powder was dissolved in toluene (50 mL). The solution was filtered through a 1-cm pad of Celite on a coarse glass frit, and toluene was then removed under reduced pressure. Dark purple crystals of **1** were obtained by sublimation at 85 °C/0.05 Torr (0.442 g, 38%): mp 95-97 °C; IR (Nujol, cm^{-1}) 1704 (w), 1628 (w), 1538 (w), 1246 (m), 1209 (s), 1132 (m), 1104 (m), 1034 (m); μ_{eff} = 2.83 and 2.84 BM in the solid state and in benzene solution, respectively. Anal. Calcd for $C_{20}H_{40}CrN_4$: C, 61.82; H, 10.38; N, 14.42. Found: C, 61.71; H, 10.06; N, 14.37.

Preparation of Bis(1,4-di-*tert*-butyl-1,3-diazabutadienyl)manganese(II) (2). In a fashion similar to the preparation of **1**, treatment of anhydrous $MnCl_2$ (0.371 g, 2.970 mmol) in tetrahydrofuran (40 mL) with a solution of $Li^{tBu2}DAD$ (prepared from 1,4-di-*tert*-butyl-1,3-diazabutadiene (1.000 g, 5.940 mmol) and freshly cut lithium metal (0.042 g, 6.000 mmol) in tetrahydrofuran (20 mL)) for 6 h at ambient temperature afforded **2** (0.942 g, 81%) as black crystals upon sublimation at 120 °C/0.05 Torr: mp 155-157 °C; IR (Nujol, cm^{-1}) 1716 (m), 1610 (m), 1558 (w), 1364 (s), 1254 (s), 1210 (s), 1007 (m), 929 (m), 759 (s); ^1H NMR (C_6D_6, 23 °C, δ) 8.06 (s, broad, C*H*), 1.10 (s, very broad, $C(CH_3)_3$); μ_{eff} = 3.85 and

3.85 BM in the solid state and in benzene solution, respectively. Anal. Calcd for $C_{20}H_{40}MnN_4$: C, 61.36; H, 10.30; N, 14.31. Found: C, 60.99; H, 9.96; N, 14.01.

Preparation of Bis(1,4-di-*tert*-butyl-1,3-diazabutadienyl)iron(II) (3). In a fashion similar to the preparation of **1**, treatment of anhydrous $FeCl_2$ (0.377 g, 2.970 mmol) in tetrahydrofuran (40 mL) with $Li^{tBu2}DAD$ (prepared from 1,4-di-*tert*-butyl-1,3-diazabutadiene (1.000 g, 5.940 mmol) and freshly cut lithium metal (0.042 g, 6.000 mmol) in tetrahydrofuran (20 mL)) for 6 h at ambient temperature afforded **3** (0.544 g, 47%) as dark brown crystals upon sublimation at 110 °C/0.05 Torr: mp 132-134 °C; IR (Nujol, cm^{-1}) 1703 (w), 1606 (w), 1525 (w), 1359 (s), 1254 (s), 1208 (s), 1022 (m), 1002 (m), 926 (m), 762 (s); μ_{eff} = 2.88 and 2.68 BM in the solid state and in benzene solution, respectively. Anal. Calcd for $C_{20}H_{40}FeN_4$: C, 61.22; H, 10.27; N, 14.16. Found: C, 61.39; H, 10.03; N, 14.16.

Preparation of Bis(1,4-di-*tert*-butyl-1,3-diazabutadienyl)cobalt(II) (4). In a fashion similar to the preparation of **1**, treatment of anhydrous $CoCl_2$ (0.386 g, 2.970 mmol) in tetrahydrofuran (40 mL) with $Li^{tBu2}DAD$ (prepared from 1,4-di-*tert*-butyl-1,3-diazabutadiene (1.000 g, 5.940 mmol) and freshly cut lithium metal (0.042 g, 6.000 mmol) in tetrahydrofuran (20 mL)) for 6 h at ambient temperature afforded **4** (0.418 g, 36%) as dark-blue crystals upon sublimation at 110 °C/0.05 Torr: mp 173-174 °C; IR (Nujol, cm^{-1}) 1698 (m), 1605 (m), 1527 (m), 1362 (s), 1260 (s), 1210 (s), 1008 (s), 933 (m), 763 (s); μ_{eff} = 1.75 and 1.83 BM in the solid state and in benzene solution, respectively. Anal. Calcd for $C_{20}H_{40}CoN_4$: C, 60.74; H, 10.19; N, 14.17. Found: C, 60.84; H, 10.01; N, 14.29.

Preparation of Bis(1,4-di-*tert*-butyl-1,3-diazabutadienyl)nickel(II) (5). In a fashion similar to the preparation of **1**, treatment of $NiCl_2 \cdot CH_3CN$ (0.507 g, 2.970 mmol) in tetrahydrofuran (40 mL) with $LitBu_2DAD$ (prepared from 1,4-di-*tert*-butyl-1,3-

diazabutadiene (1.000 g, 5.940 mmol) and freshly cut lithium metal (0.042 g, 6.000 mmol) in tetrahydrofuran (20 mL)) for 6 h at ambient temperature afforded **5** (0.482 g, 41%) as dichroic red-green crystals upon sublimation at 110 °C/0.05 Torr: mp 184-185 °C; IR (Nujol, cm^{-1}) 1715 (w), 1625 (w), 1547 (w), 1493 (s), 1264 (s), 1212 (s), 934 (m), 764 (s); ^{1}H NMR (C_6D_6, 23 °C, δ) 8.95 (s, 2H, C*H*), 1.93 (s, 18H, $C(CH_3)_3$); $^{13}C\{^{1}H\}$ NMR (C_6D_6, 23 °C, ppm) 129.88 (s, *C*H), 64.61 (s, $C(CH_3)_3$), 30.61 (s, $C(CH_3)_3$). Anal. Calcd for $C_{20}H_{40}N_4Ni$: C, 60.77; H, 10.20; N, 14.85. Found: C, 60.89; H, 9.88; N, 14.61.

Solid State Thermolyses of 1-5. Thermolysis experiments were performed on analytically pure samples of **1-5** to assess their solid state thermal decomposition products. A 20-cm long, 2.5-cm diameter quartz tube, equipped with female 24/40 joints on each end, was fitted with two flow control valves that were attached to male 24/40 joints. A 6-cm long, 1-cm diameter glass vial was charged with 1.00 g of the sample in a glove box. The vial was placed in the center of the quartz tube. This apparatus was placed into a tube furnace and a 50 sccm flow of argon was established. The sample was then heated to 500 °C for 1 h and was allowed to cool to room temperature under argon flow. Subsequently, the powder residues were collected from the inside of the quartz tube and subjected to X-ray powder diffraction analyses as described in the text.

X-ray Crystallographic Structure Determinations. Diffraction data were measured on a Bruker *X8 APEX-II* kappa geometry diffractometer with Mo radiation and a graphite monochromator. Frames were collected at 100 K with the detector at 40 mm and 0.3-0.5° between each frame. The frames were recorded for 3-5 s. *APEX-II*[94] and *SHELX*[95] software were used in the collection and refinement of the models. All structures contained discrete neutral complexes without ions or solvent. Complex **1** crystallized with two independent but chemically equivalent molecules in the asymmetric unit. Complexes **3-5** are all isostructural, with one-half molecule in the asymmetric unit. The iron, cobalt and nickel atoms all occupy a crystallographic mirror plane.

Preparative Sublimation Studies. For the sublimation experiments, 2.5 cm diameter, 30 cm long glass tubes were employed. One end of the tube was sealed and the other end was equipped with a 24/40 male glass joint. In an argon-filled glove box, the compound to be sublimed (0.5-1.0 g) was loaded into a 1.0 x 4.0 cm glass tube and this tube was placed at the sealed end of the glass sublimation tube. The sublimation tube was fitted with a 24/40 vacuum adapter, and then was inserted into a horizontal Büchi Kugelrohr oven such that about 15 cm of the tube was situated in the oven. A vacuum of 0.05 Torr was established, and the oven was heated to the indicated temperature. The compounds sublimed to the cool zone just outside of the oven. The percent recovery was obtained by weighing the sublimed product. The percent nonvolatile residue was calculated by weighing the 1.0 x 4.0 cm glass tube at the end of the sublimation. Data are given in the above text and are included in Table 4.

CHAPTER 3

Atomic Layer Deposition of Nickel Nitride Thin Films from a Volatile and Thermally Stable Nickel Diazadienyl Precursor

3.1 Introduction

Transition metal nitrides have received considerable attention recently due to their potential uses as diffusion barriers, electrical contacts, optical coatings, and corrosion inhibitors.[96] Nickel nitride (Ni_3N) in particular is recognized as a useful material due to its inherit magnetic and electrical properties.[97] Ni_3N is also used as an intermediate material to the formation of metallic nickel and nickel silicide.[60] Thermogravimetric analysis of Ni_3N powders under reducing atmosphere was studied and nickel metal was reported as the final decomposition product at 160 °C.[98] A subsequent study revealed that the decomposition temperature of Ni_3N to depends upon the atmosphere under which decomposition is occurring.[99] Ni_3N is shown to decompose around 150 °C under reducing conditions and upwards of 300 °C under inert atmospheres.[98,99] Thin films of Ni_3N have been produced using chemical vapor deposition,[60,53d,100a] physical vapor deposition,[100b-e] and ion beam implantation.[99,100f,100g]

In this chapter, the first ALD growth study of Ni_3N is presented. Films were grown using a volatile and thermally stable nickel diazadienyl precursor mentioned in the previous chapter, bis(1,4-di-*tert*-butyl-1,3-diazabutadienyl)nickel(II) (**5**) and 1,1-dimethylhydrazine as the coreactant. Complex **1** undergoes solid state decomposition at 230 °C and sublimes on a preparative scale at 115 °C/0.05 Torr with a sublimed recovery of 92.3% and nonvolatile residue of 6.9% as mentioned in Chapter 2. Hence, **1** has potential properties as an ALD precursor. This process exhibits an ALD window between 225 and 240 °C and affords high quality Ni_xN (x = 2-4.6) with low impurity concentration on thermal SiO_2 substrates. The scheme for this process is illustrated in Figure 23.

Figure 23. General scheme for the ALD growth of Ni_xN from **5**.

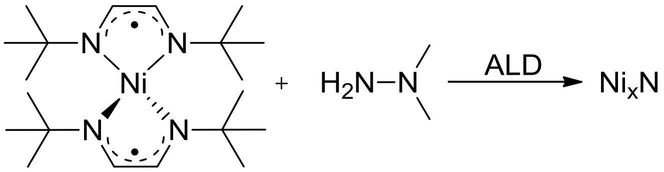

3.2 Results and Discussion

ALD growth of Ni_3N on 500 nm thick thermal SiO_2 was investigated using **1** and anhydrous 1,1-dimethylhydrazine. The growth of Ni_3N was evaluated by varying substrate temperatures, precursor pulse lengths, and the number of deposition cycles. The study of growth rate as a function of the pulse length of **5** was carried out at a substrate temperature of 225 °C (Figure 24). The 1,1-dimethylhydrazine pulse length, purge time between each reactant, and the number of deposition cycles were held constant at 0.2 s, 3.0 s, and 1000 cycles, respectively. The source temperature was kept at 150 °C to allow for sufficient consumption of the precursor over the deposition period. In order to display that film growth is occurring by a self-limited ALD mechanism, film saturation must be demonstrated. In the event of surface saturation, all available surface sites are occupied with adsorbed precursor molecules, which in turn remain on the film surface awaiting the introduction of a second co-reactant. Once this condition is met, a constant growth rate is observed even in cases of excess precursor dose, given that neither precursor undergoes thermal decomposition. Self-limited film growth was achieved with **1** pulse lengths ≥ 4.0 s as demonstrated by a constant growth rate of 0.70 Å/cycle. Shorter pulse lengths of **5** (< 4 s) may lead to sub-saturative growth and loss of the self-limited ALD mechanism. For the studies described herein, a pulse length of 4.0 s for **5** was used to guarantee self-limited film growth. A plot of growth rate versus 1,1-dimethylhydrazine pulse length exhibited similar saturative behavior at pulse lengths ≥ 0.2 s (Figure 25).

Figure 24. Growth rate as a function of the pulse length of **5** at a substrate temperature of 225 °C.

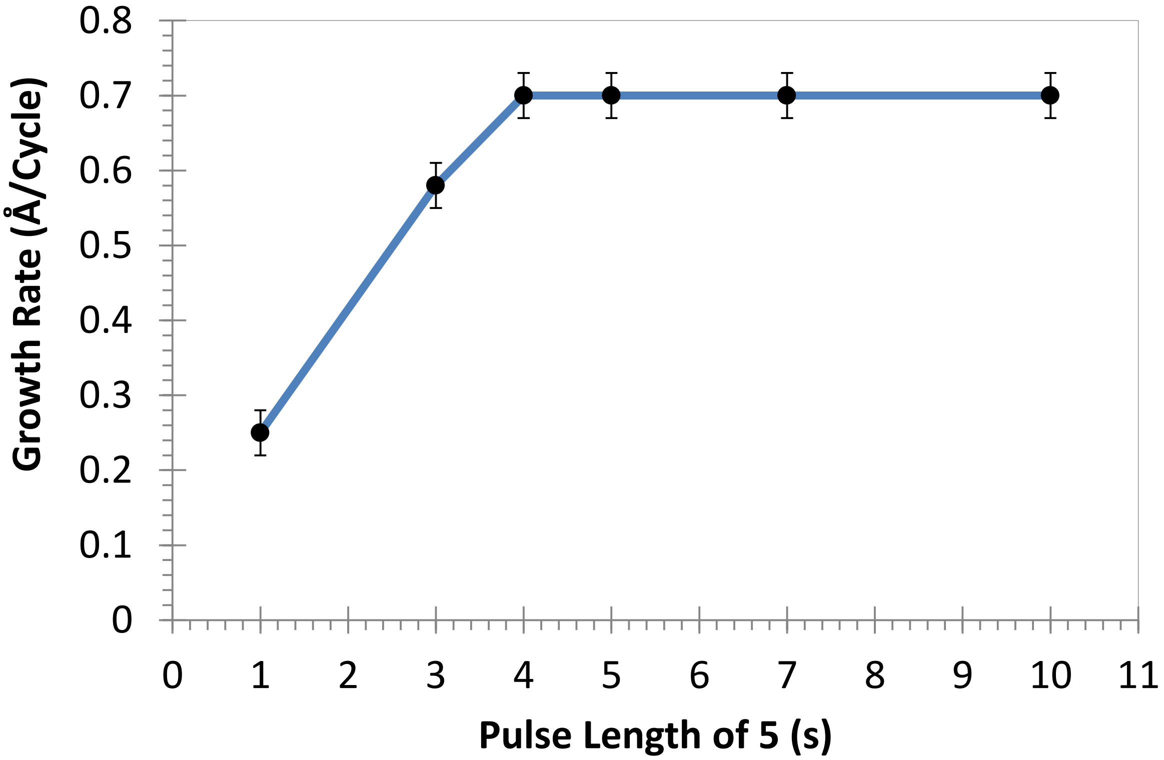

Figure 25. Growth rate as a function of the pulse length of 1,1-dimethylhydrazine at a substrate temperature of 225 °C.

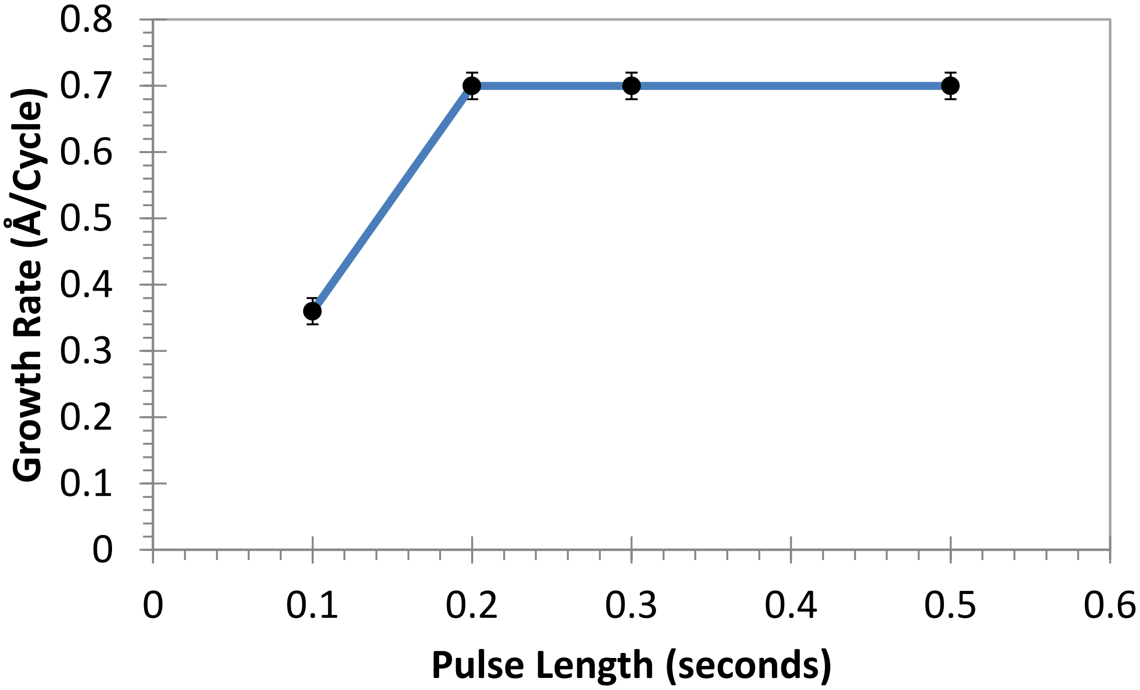

The effect of substrate temperature upon growth rate was also investigated (Figure 26). Film depositions were carried out using **5** and 1,1-dimethylhydrazine pulse lengths of 4.0 s, 0.2 s, and 1000 deposition cycles. Nitrogen purge times of 3.0 s were used between each reactant pulse. A constant growth rate of 0.70 Å/cycle was observed between 225 and 240 °C. Such a region of constant growth rate over a specified temperature range is called the "ALD window" and is further evidence of a self-limited ALD process.[2,10,73] Interestingly, the observed ALD window extends up to 240 °C, which lies slightly beyond the decomposition temperature of **5** (230 °C). At substrate temperatures $\geq$ 240 °C, the growth rate increases, presumably due to precursor decomposition. Ni_xN growth rates of 0.15 and 0.95 Å/cycle were observed at substrate temperatures of 200 and 250 °C, respectively, which lie outside of ALD window.

Figure 26. Growth rate as a function of deposition temperature. An ALD window is observed between 225 and 240 °C.

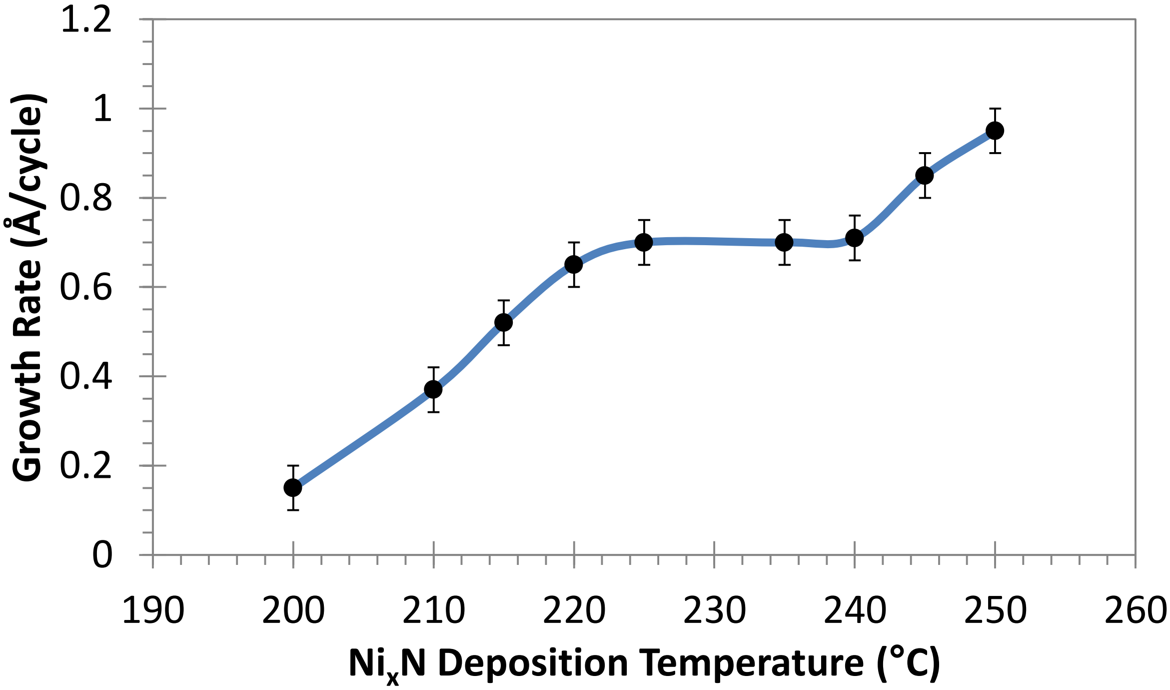

The influence of the number of deposition cycles upon the film thickness of Ni$_x$N was subsequently investigated. In these experiments, **5** and 1,1-dimethylhydrazine pulse lengths were kept at 4.0 and 0.2 s, respectively, with a 3.0 s inert gas purge between each reactant pulse. The substrate temperature was held at 225 °C. As expected, a linear relationship exists between film thickness and the number of ALD cycles (Figure 27). A trend-line that demonstrates a best fit for the data points collected has a y-intercept of 4.45 nm. In principle, the y-intercept should be zero or negative which would indicate an incubation period. In this case, the positive y-intercept value could be attributed to experimental error.

Figure 27. Film thickness as a function of the number of deposition cycles at a growth temperature of 225 °C.

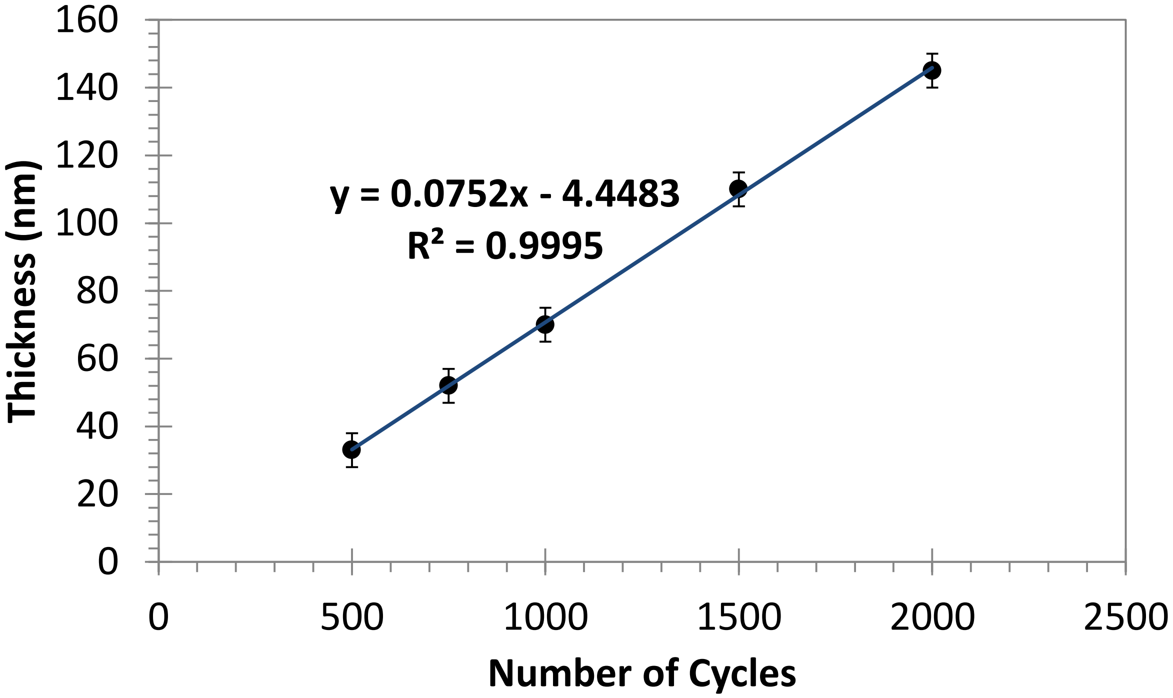

X-ray photoelectron spectroscopy was performed on a representative Ni_xN film deposited at 225 °C to assess the elemental composition and presence of impurities (Figure 28). The surface of the as-deposited film showed the expected ionizations arising from Ni, as well as small ionizations from oxygen, nitrogen, and carbon. A high-resolution scan of the Ni 2p region, as shown in Figure 29, shows evidence for Ni^{2+} as illustrated by the presence of Ni shake-up satellite ionizations. This is a strong indication that the film surface is undergoing oxidation when exposed to ambient atmosphere. Covered samples were stored in open air for 48 h before analysis. Upon 45 s of Ar-ion sputtering all shake-up ionizations disappear, indicating the presence of Ni^0. Before sputtering, nitrogen atomic concentrations were between 2 and 3 at % which were much lower than anticipated; unexpected low N is likely due to film oxidation. After argon ion sputtering, a constant composition of 86.5 at % nickel, 1.2 at % carbon, 10.3 at % oxygen, and 2.0 at % nitrogen was observed. The Ni $2p_{1/2}$ and Ni $2p_{3/2}$ ionizations appeared at 869.6 and 852.2 eV. It is presumed that the Ar-ion sputter gun is inducing film reduction resulting in preferential nitrogen loss or nitrogen off-gassing, which may explain the presence of Ni^0 and low observed nitrogen values.

Figure 28. XPS spectra of Ni_xN films deposited at 225 °C/1000 cycles.

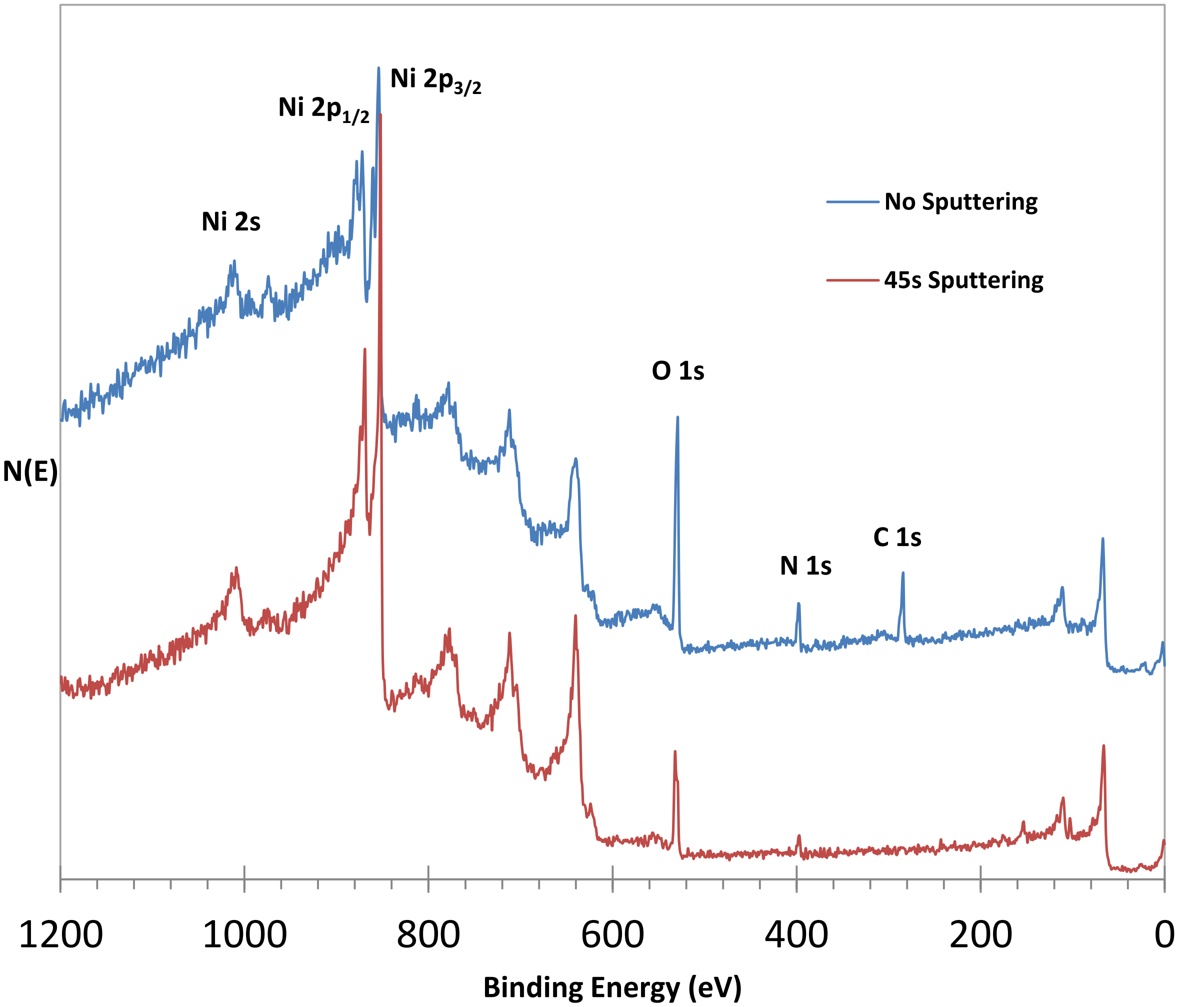

Figure 29. High-resolution XPS multiplex of Ni 2p region.

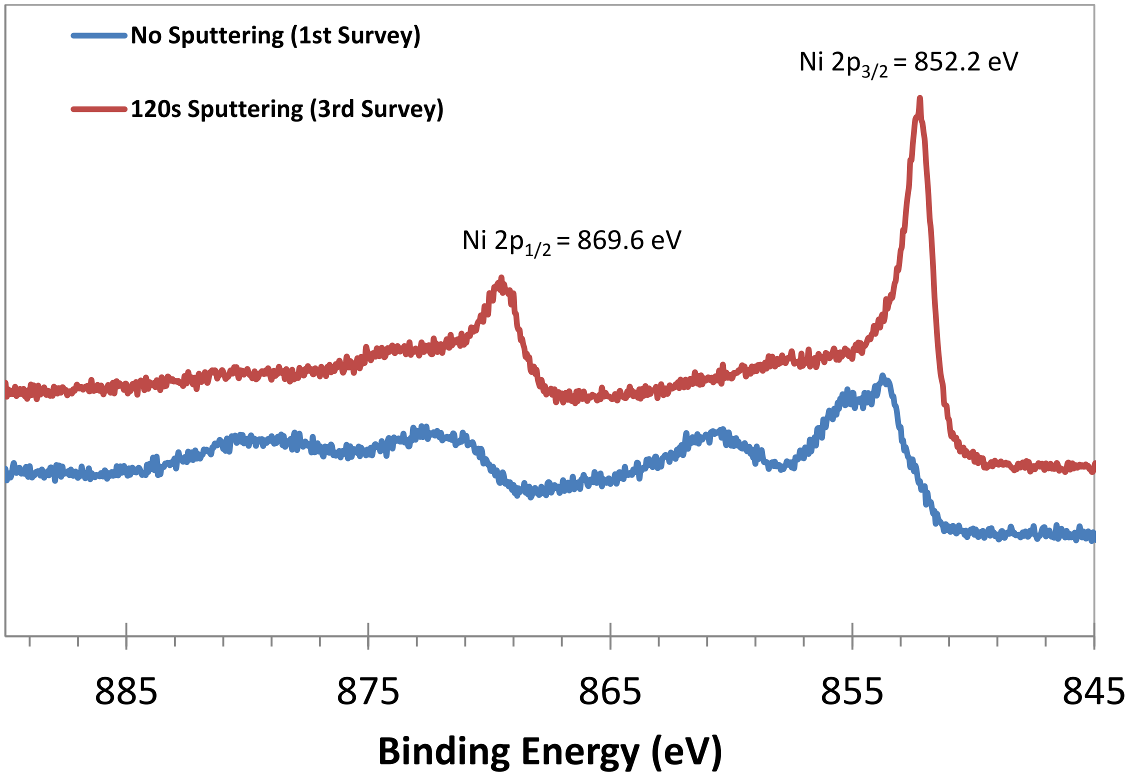

TOF-ERDA was performed on as-deposited films grown at 225, 230, 240, and 400 °C to probe the elemental compositions (Table 6). The atomic compositions of the films ranged from 53.5 to 55.5% nickel, 1.7-2.6% carbon, 32.6-41.0% oxygen, 0.7-4.2% nitrogen, and 3.1-6.6% hydrogen. Again, it is presumed that the presence of elevated carbon, oxygen, and hydrogen impurities may arise from post-deposition exposure to the ambient atmosphere. The oxidation process may be evolving volatile nitrogen compounds giving the resulting oxidized surface with high oxygen and low nitrogen content. Samples were analyzed six months after deposition due to unexpected instrument maintenance in Dresden, Germany. While care was taken to secure the shipment under argon, the delayed analysis undoubtedly led to loss of inert conditions and further oxidation.

Table 6. Atomic concentrations of Ni, O, N, C, and H obtained by TOF-ERDA.

Deposition Temperature (°C)	**at % Ni**	**at % O**	**at % N**	**at % C**	**at % H**
215	55.1 ± 0.5	32.6 ± 0.7	4.2 ± 0.3	2.5 ± 0.2	5.7 ± 0.2
225	53.5 ± 0.5	33.3 ± 0.8	4.0 ± 0.3	2.6 ± 0.3	6.6 ± 0.2
235	55.5 ± 0.5	33.0 ± 0.8	4.1 ± 0.3	1.7 ± 0.2	5.8 ± 0.3
245	53.4 ± 0.5	41.0 ± 0.7	0.7 ± 0.1	1.9 ± 0.2	3.1 ± 0.3

To assess possible preferential sputtering of nitrogen in XPS, fresh samples were deposited, sealed carefully under inert conditions, and submitted for Rutherford backscattering (RBS) and nuclear reaction analyses (NRA). These studies were employed to obtain accurate Ni:N ratios. Representative films deposited at 1000 cycles at temperatures of 215, 225, 235, and 245 °C were used to quantify how the Ni:N ratio will vary with deposition temperature. As shown on Table 7, the values of x in Ni_xN vary independently as a function of temperature with x ranging from 2.0 to 4.6 at 235 and 215 °C respectively. These results showed that nitrogen is retained in the sample, which XPS and XRD could not verify. The labile nature of nitrogen in the film may indicate the sudden increase of Ni in the film deposited at 245 °C. Loss of nitrogen and reduction to Ni metal at this temperature is well documented, as previously mentioned.[98,99] This process was verified to yield metallic Ni by powder XRD analysis when deposited at 250 °C as shown in Figure 30.

Table 7. Ni:N ratio as a function of deposition temperature determined by RBS/NRA.

Deposition Temperature (°C)	**Ni:N ratio**
215	4.6 : 1
225	3.5 : 1
235	2.0 : 1
245	3.9 : 1

Figure 30. Powder XRD scan of a Ni_xN film deposited at 250 °C.

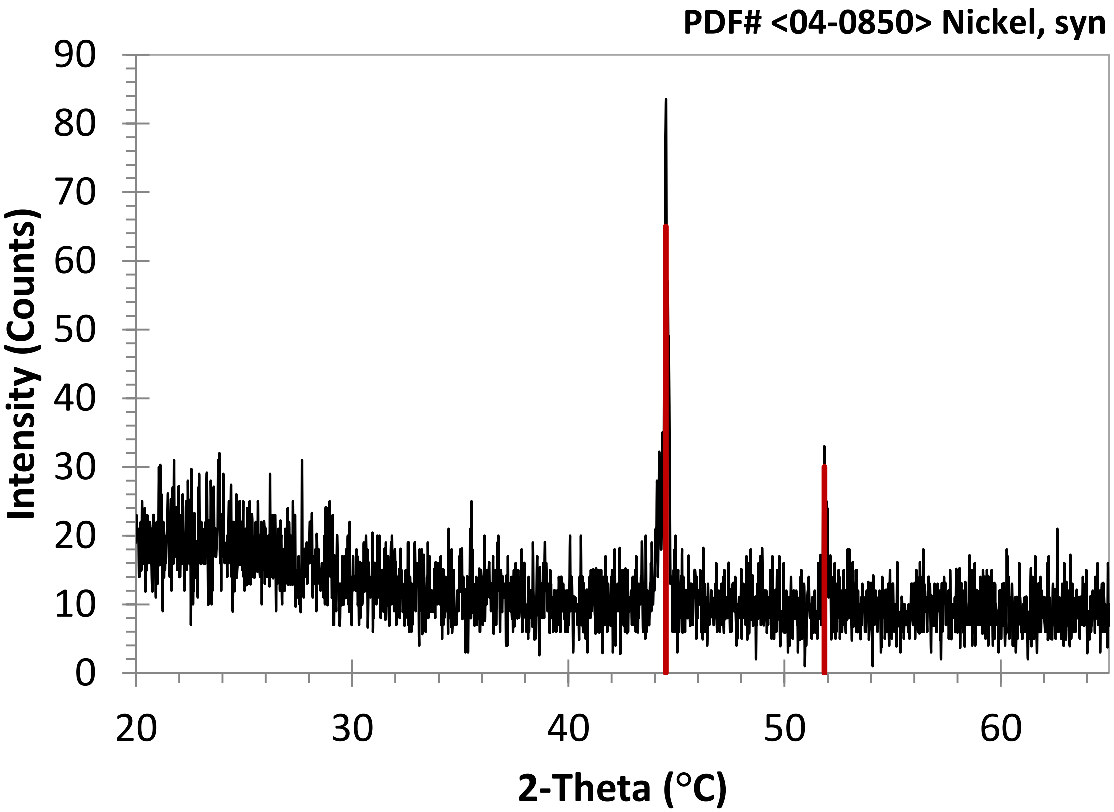

Surface morphology was examined using atomic force microscopy (AFM) and scanning electron microscopy. The AFM image of a 70 nm thick film grown at 225 °C is shown in Figure 31. The rms surface roughness of a 2 μm x 2 μm area was 10.87 nm and the surface contains various sized granules. An AFM study of the surface roughness at different substrate temperatures indicates a large gain in rms surface roughness from 225 (10.9 nm) to 250 °C (16.0 nm). This increase can be attributed to particle agglomeration and self-decomposition of **5** to nickel metal at temperatures ≥ 240 °C. In fact, a powder X-ray diffraction (XRD) scan of a film deposited at 250 °C displayed weak reflections that correspond to nickel metal (JCPDS file number 04-0850) Figure 30. Scanning electron micrograph images of films grown under identical conditions showed film surfaces that were free of cracks and pinholes and contained similar surface features to those observed using AFM. In addition, powder XRD experiments showed that all films were amorphous as deposited at temperatures within the ALD window.

Figure 31. AFM images of Ni_xN films deposited at (**a**) 225 °C (70 nm thick; RMS roughness = 10.9 nm), (**b**) 235 °C (70 nm thick; RMS roughness = 13.6 nm), and (**c**) 250 °C (95 nm thick; RMS roughness = 16.0 nm).

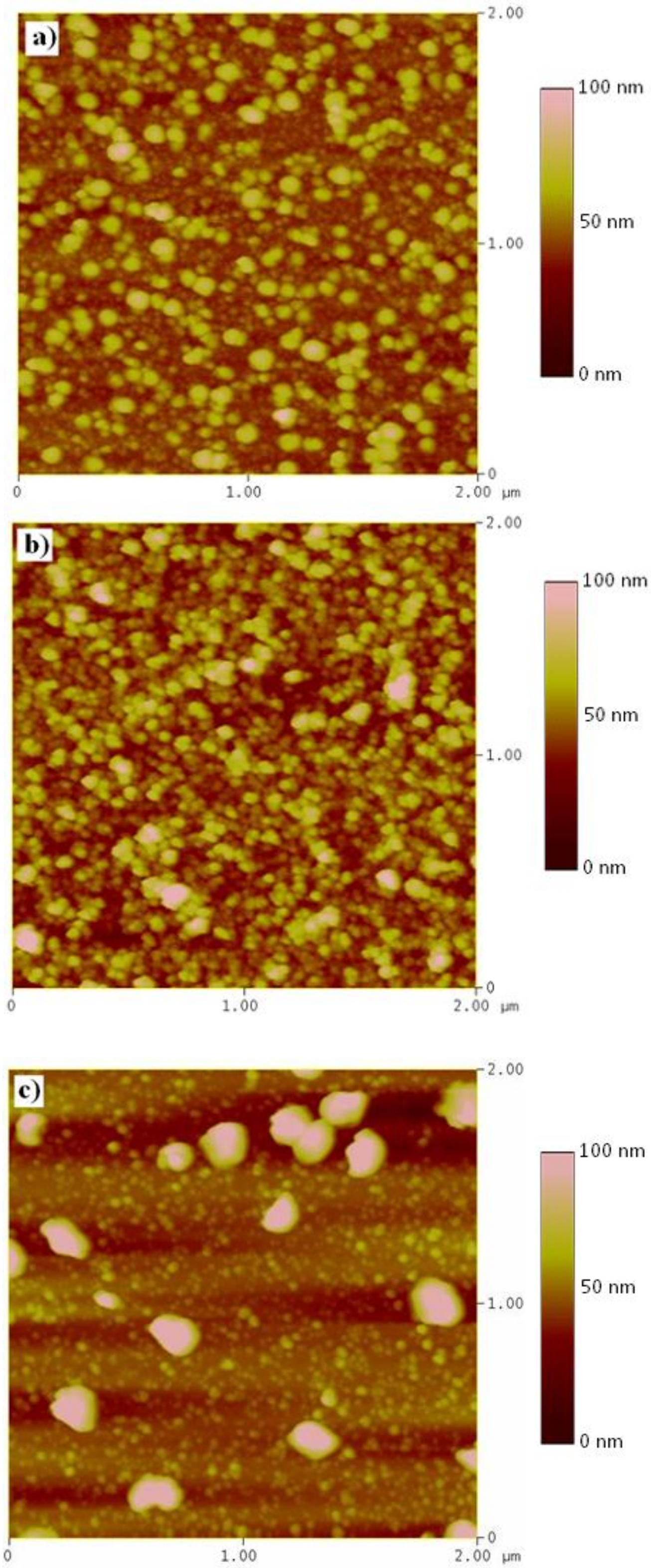

3.3 Conclusions

The study documented herein demonstrates the first ALD growth of Ni_3N thin films. An ALD window was observed between 225 and 240 °C. The upper limit of ALD growth is due to the decomposition of **5** to nickel metal as determined by XRD. The affinity for nitride formation in this process is likely due to the use of 1,1-dimethylhydrazine. However, it appears that nitrogen incorporated in the film is easily displaced by film oxidation or through Ar-ion sputtering as verified by XPS studies. In addition, it was found that the films begin to decompose thermally to Ni metal at 250 °C as shown by XRD. This observation supports previous documented examples of incidences involving Ni_3N decomposition under similar conditions.[98,99] While little documented evidence exists explaining the air-sensitive nature of Ni_3N, it is proposed that the high roughness of the surface plays an important role. The high surface area exposed may allow for quick and thorough oxidation of Ni_3N deposited by this process. Future studies employing **5** and other transition metal analogs should avoid use of nitrogen-based co-reactants to prevent unwanted nitride formation in the pursuit for metallic films.

3.4 Experimental Section

A Picosun R-75BE ALD reactor was used for thin film deposition experiments. The ALD reactor was operated under a constant stream of nitrogen (99.9995%) at a pressure of 8–12 mbar. The deposition of Ni_xN thin films by ALD was studied employing **5**, and anhydrous 1,1-dimethylhydrazine (SAFC-Hitech). In initial growth trials, the sublimation temperature for **1** was found to be optimum at 150 °C under the reactor pressure. The substrate temperatures were held between 200 and 250 °C. Nitrogen was used as both the carrier and purge gas and was purified from ambient air using a Texol GeniSys nitroGenerator. Film growth experiments were performed using a range of pulse lengths for **1** and anhydrous 1,1-dimethylhydrazine to determine the degree of surface saturation. Ni_xN films were deposited on thermal SiO_2 substrates (500 nm thick) obtained from Noel Technologies. One substrate, a 3 cm x 3 cm square coupon, was used in each deposition experiment. Film thicknesses were determined using cross-sectional SEM collected on a JEOL-6510LV scanning electron microscope. The film growth rate was determined by dividing the measured film thickness by the number of deposition cycles. Powder X-ray diffraction experiments were performed on a Rigaku R200B 12 kW rotating anode diffractometer, using Cu Kα radiation (1.54056 Å) at 40 kV and 150 mA. AFM images were obtained using a MultiMode nanoscope IIIa (Digital Instruments, VEECO). The samples were measured using the tapping mode in air with an E scanner with a maximum scanning size of 12 µm at a frequency of 1 or 2 Hz. The tip employed was a Tap150AI-G with a resonance frequency of 150 kHz and a force constant of 5 N/m. Surface roughness was calculated as rms values. XPS analyses were performed using a Perkin-Elmer 5500 XPS system using monochromatized Al Kα radiation using AugerScan v3.2 as the analyses software. RBS experiments were carried out by using a 2 MeV He^{2+} ion beam at a backscattering angle of 165° to quantify nitrogen content in the films. Quantitative determination of nickel was made by NRA using 1.25 MeV deuterium beam. A thin foil of mylar was placed in front of the silicon particle detector to filter out the backscattered ions. Sputtered samples of Au and TiN upon silicon substrates were used as calibration standards for RBS and NRA experiments. RBS and NRA composition values were compared to evaluate the Ni:N ratios. SIMNRA 6.0 was used as the RBS/NRA analysis software. TOF-ERDA was performed using a 35 MeV Cl^{7+} ion beam. The angle between the sample normal and the incoming beam is 75°, the scattering angle is 31°. The analyzed area was 1.5 x 1.5 mm². The recoil ions were detected with a Bragg Ionization Chamber using a full energy detection circuit and a fast timing circuit to obtain a Z dependent signal to separate ion species. Hydrogen was detected with a separate solid state detector at a scattering angle of 38° preceded by a Mylar foil to stop other scattered and recoiled ions.

CHAPTER 4

Low Temperature Growth of High Purity, Low Resistivity Copper Films by Atomic Layer Deposition

4.1 Introduction

In this chapter, a new low temperature copper ALD process is described that employs a three precursor sequence entailing Cu(dmap)$_2$ (**6**), formic acid, and hydrazine. In this process, **6** is unreactive toward hydrazine but is transformed to copper(II) formate, which is then readily reduced to copper metal by the hydrazine pulses. The work described in this chapter therefore addresses a central problem with the ALD growth of metal thin films: low reactivity of the metal precursors towards common reducing co-reagents. Analogous three-step processes comprising a metal precursor, a strong acid, and a reducing agent should allow the low temperature ALD growth of many transition metal thin films.

Multi-step approaches in developing ALD processes are not unprecedented and have been used previously in the growth of metal films. Other multi-step routes to copper films have included reduction of ALD CuO by isopropanol,[71] reduction of ALD Cu_3N with H_2,[72] and reduction of ALD Cu_2O by formic acid in conjunction with a ruthenium seed layer.[73] Examples of direct copper ALD processes include $CuL_2/ZnEt_2$ at 100-150 °C (L = $OCHMeCH_2NMe_2$, β-ketiminate, β-diketiminate),[62,63] Cu(thd)$_2$/H_2 at 190-260 °C (thd = 2,2,6,6-tetramethyl-3,5-heptanedionate),[64] [Cu(sBuNCMeNsBu)]$_2$/H_2 at 150-250 °C,[65] Cu(hfac)$_2$/alcohol at 300 °C (hfac = 1,1,1,5,5,5-hexafluoro-3,5-pentanedionate),[66] CuCl/H_2 at 360-410 °C,[67] and CuCl/Zn at 440-500 °C.[68] ALD growth of copper thin films was claimed from a copper(I) β-diketiminate precursor and diethylsilane,[69] but a later study showed that this process proceeds by a CVD mechanism.[70]

4.2 Results and Discussion

Growth of copper metal films by ALD was carried out using **6**, formic acid, and anhydrous hydrazine as precursors on Si(100) substrates with the native oxide. Precursor **6** has been previously reported[101,102] and is commercially available.[103] Initial ALD growth studies performed with **6** and formic acid at 120 °C afforded green-colored films that washed off of the substrate upon rinsing with deionized water. Presumably, this film corresponded to copper(II) formate, which is stable at the 120 °C deposition temperature. Thermogravimetric analysis of commercially available copper(II) formate tetrahydrate revealed a two-step weight loss event from 50 to 300 °C (Figure 31). The first step corresponds to dehydration of two water molecules confirmed by the sharp endotherm in the DTA scan. Two equivalents of water were lost before approaching 50 °C for a total of four evolved equivalents after 100 °C. The second weight loss event around 200 °C, corresponds to the thermal decomposition to Cu(II) formate to Cu metal. This process is illustrated in Figure 33. This temperature range is well above the thermal decomposition temperature of **6** (~175 °C). Hence, copper film growth at ≥ 225 °C from **6** in a two-step process would proceed by a CVD-like mechanism due to the thermal decomposition of **6** to Cu metal. In addition, using formic acid as the sole reducing agent will prove unworthy as the minimum deposition temperature to yield Cu metal from this process will be > 200 °C, a temperature deemed too high for the microelectronics industry. Therefore, an alternative route will need to be taken if Cu metal is to be deposited at low temperature.

Figure 32. TGA/DTA trace of Cu(II) formate tetrahydrate.

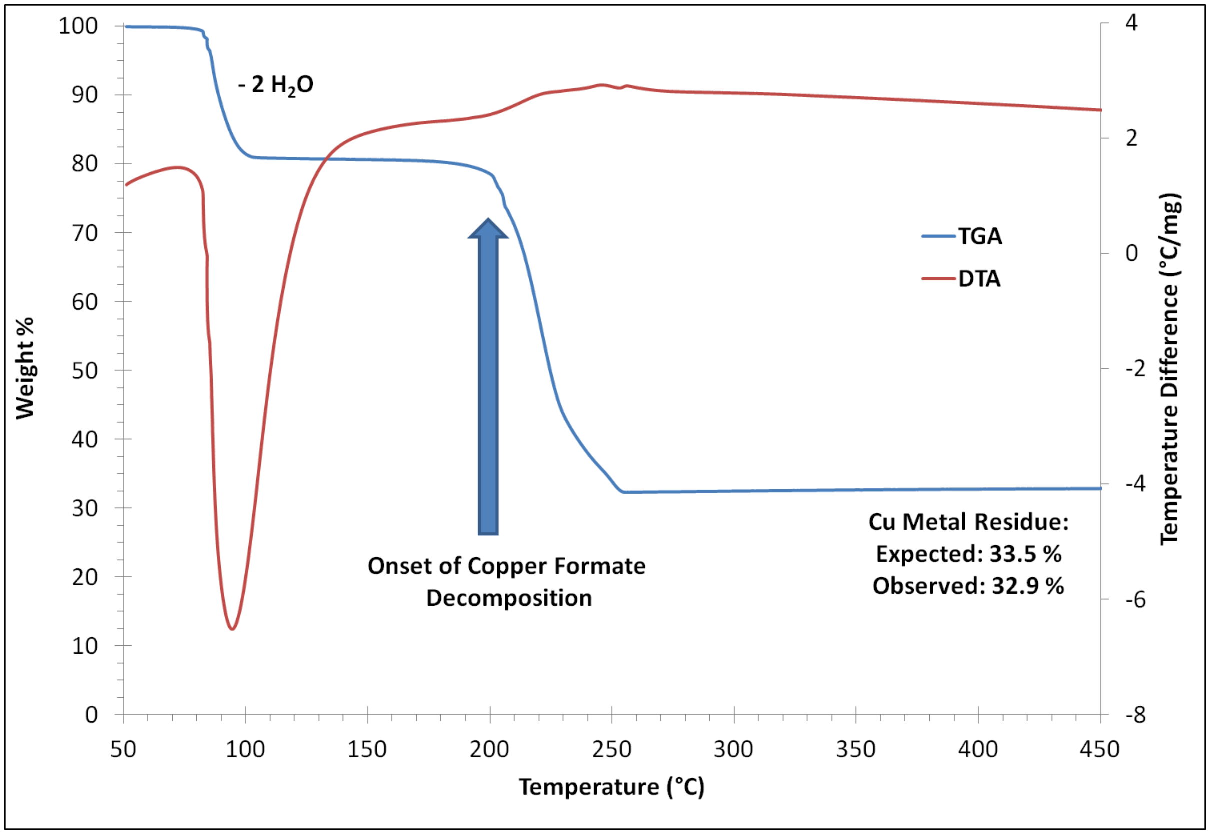

Figure 33. Thermal decomposition of Cu(II) formate to Cu metal.

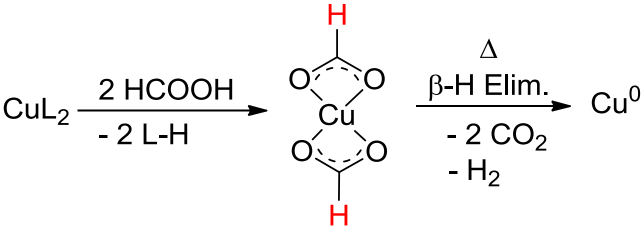

Results in Figure 32 show that Cu(II) formate can be thermally reduced but at temperatures in excess of 200 °C, a temperature too high for a viable Cu ALD process. Efforts were further directed towards the reduction of Cu(II) formate with hopes of lowering the threshold reduction temperature. Chemical reduction of Cu(II) formate may provide a way to access a low temperature Cu metal ALD process. A previous report noted that aqueous solutions of transition metal(II) formates (manganese, cobalt, nickel, and cobalt) undergo a variety of reactions upon treatment with hydrazine hydrate.[104] Interestingly, the copper formate reaction mixture was not stable and resulted in a violent reaction with copper metal formation at room temperature. This result encouraged the exploration of analogous reactions towards developing a low temperature ALD process for Cu metal. Subsequently, the experiment was repeated under careful conditions using commercially available Cu(II) formate (Table 8). Under addition of a few drops of hydrazine hydrate or 1,1-dimethylhydrazine, the blue aqueous Cu(II) formate solution instantly darkened and violently bubbled. After a few minutes of stirring, the opaque orange solution began to leave a Cu metal mirror on the surface of the Erlenmeyer flask (Figure 34). These reactions verify that hydrazine and hydrazine derivatives can chemically reduce Cu(II) formate to Cu metal. Of significance, these reactions occur at room temperature.

Table 8. Solution reaction results of various Cu(II) salts and hydrazine derivatives.

Complex	**Hydrazine**	**1,1-dimethylhydrazine**
Cu(II) Formate	Copper metal	Copper metal
Cu(II) Acetate	Copper metal	Copper metal

Figure 34. Picture of the product of Cu(II) formate and hydrazine.

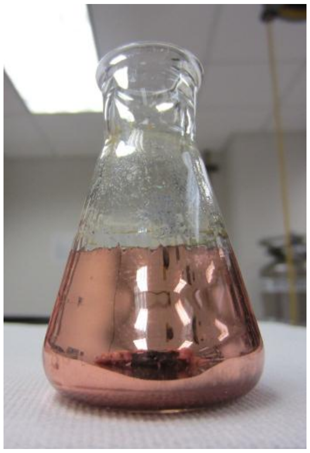

Accordingly, a three-step ALD process entailing **6**, formic acid, and hydrazine was envisioned. Precursor **6** and formic acid leads to the formation of surface bound Cu(II) formate and subsequent exposures to hydrazine drive Cu metal film formation. To assess the growth behavior, precursor pulse lengths, substrate temperatures, and the number of cycles were varied. The growth rate was investigated as a function of the pulse length of **6** at a substrate temperature of 120 °C. The number of deposition cycles, lengths of the formic acid and hydrazine pulses, and length of the purges after each pulse were kept constant at 1000, 0.2 s, 0.2 s, and 5.0 s, respectively. As shown in Figure 35, pulse lengths for **6** of ≥ 3 s afforded a constant growth rate of about 0.50 Å/cycle. Similar experiments were used to explore the growth behavior as a function of the formic acid (Figure 36) and hydrazine pulse lengths (Figure 37), using 1000 cycles, 3.0 s pulses of **6**, 5.0 s purges between precursor pulses, and a growth temperature of 120 °C. Plots of growth rate versus pulse length demonstrated saturative growth with formic acid and hydrazine pulse lengths of ≥ 0.1 s. These experiments demonstrate that the film growth at 120 °C proceeds by a self-limiting ALD growth mechanism. No copper metal film growth was observed at < 200 °C with processes employing **6** and formic acid or **6** and hydrazine.

Figure 35. Growth rate as a function of the pulse length of **6**.

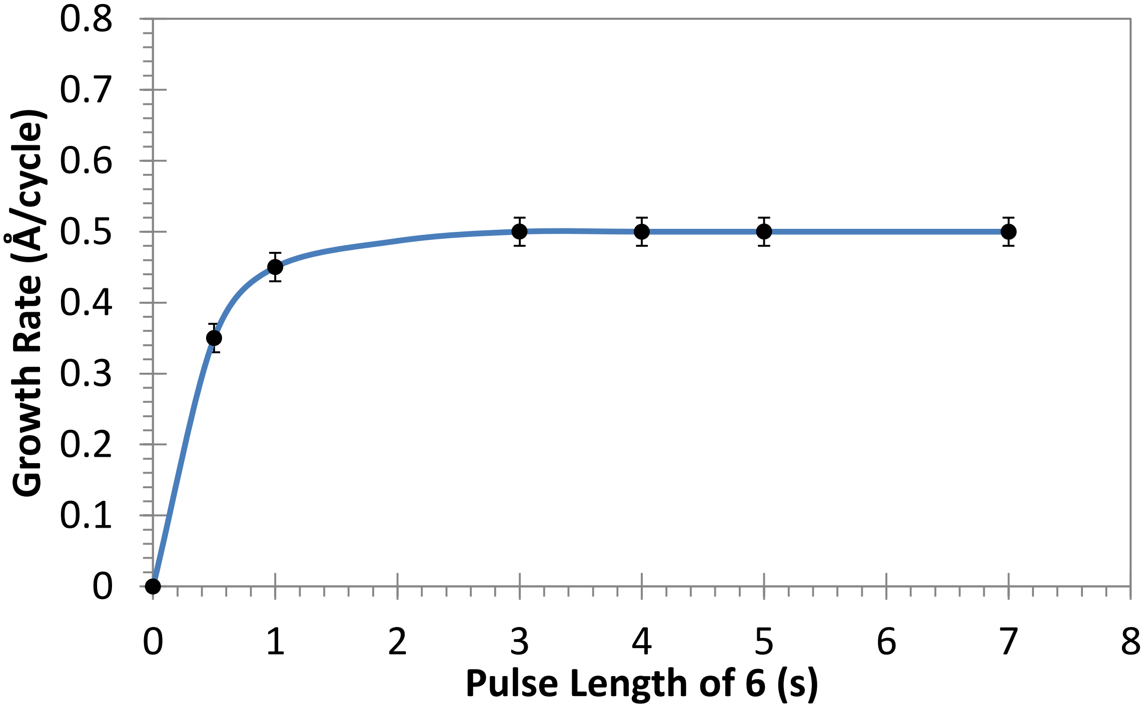

Figure 36. Growth rate as a function of formic acid pulse length.

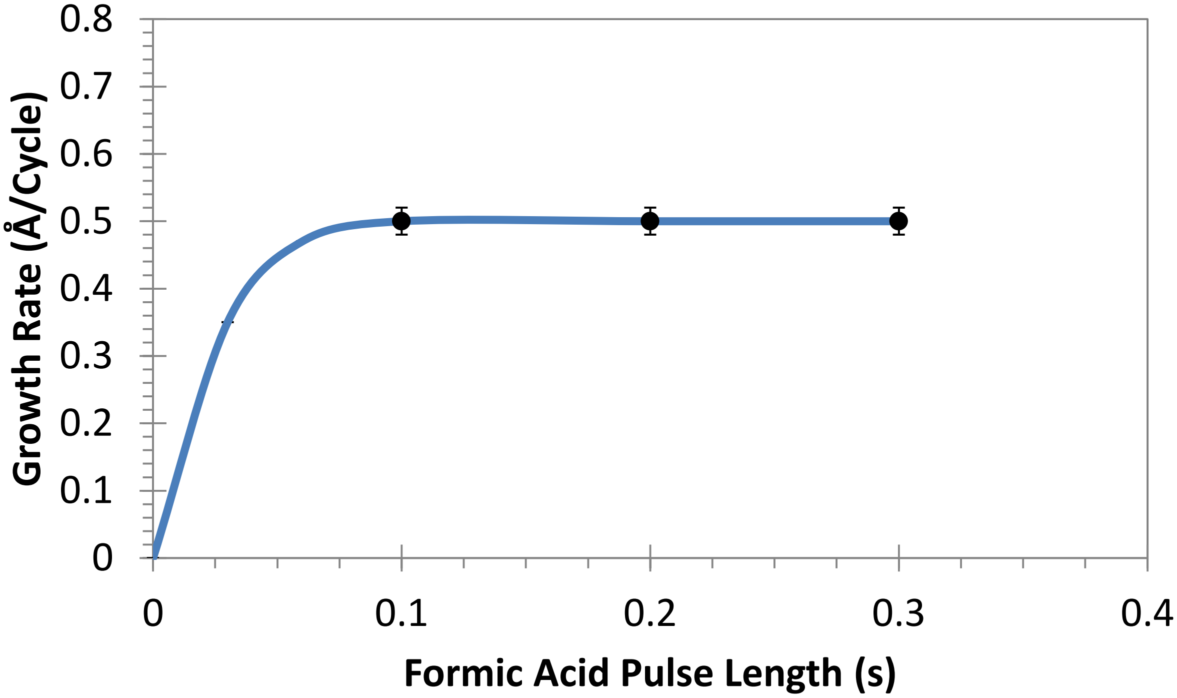

Figure 37. Growth rate as a function of hydrazine pulse length.

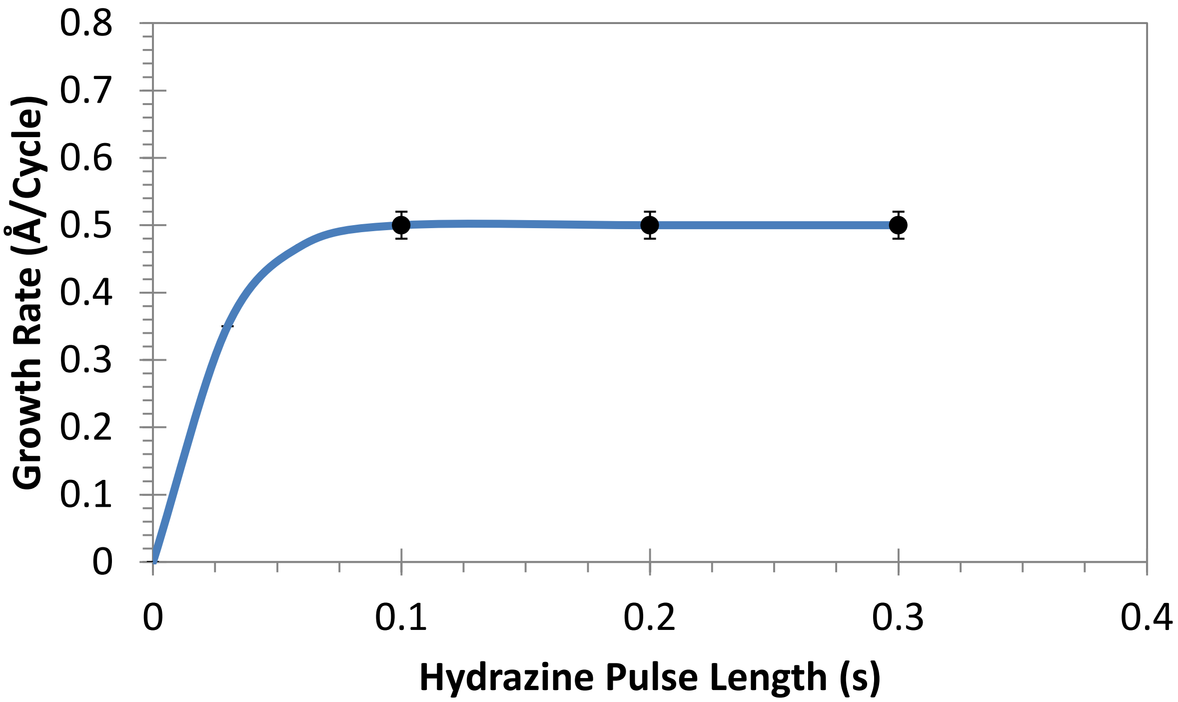

The growth rate as a function of deposition temperature was also investigated (Figure 38). The conditions in these depositions consisted of pulse lengths of 3.0 s, 0.2 s, and 0.2 s for **1**, formic acid, and hydrazine, respectively, purge lengths of 5.0 s between pulses, and 1000 deposition cycles. A constant growth rate of 0.47-0.50 Å/cycle was observed between 100 and 170 °C (the ALD window). Lower growth rates occurred at 80, 180, and 200 °C.

Figure 38. Growth rate as a function of deposition temperature. An ALD window is observed between 110 and 160 °C.

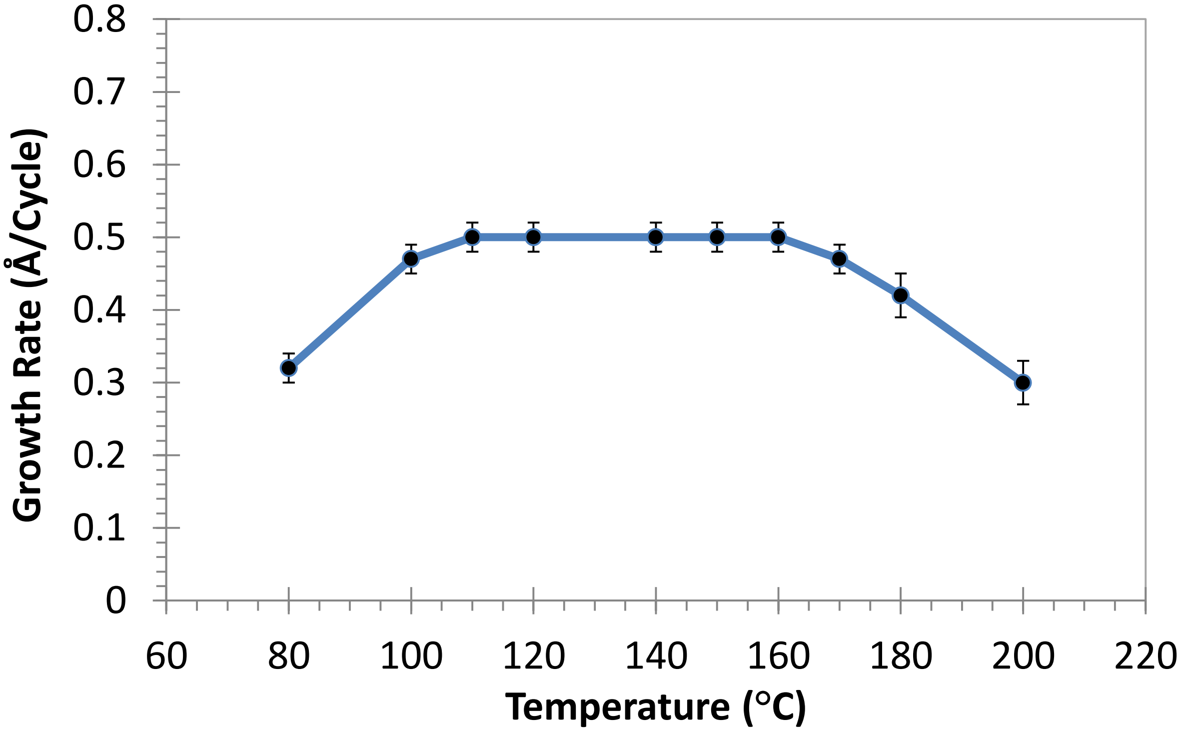

The dependence of the film thickness on the number of deposition cycles was investigated next (Figure 39). In these experiments, the pulse lengths of **6**, formic acid, and hydrazine were 3.0 s, 0.2 s, and 0.2 s, respectively, with purge lengths of 5.0 s between pulses. The deposition temperature was 120 °C. The film thicknesses varied linearly with the number of cycles and the slope of the line (0.50 Å/cycle) equaled the saturative growth rate established in Figure 26. The line of best fit shows a y-intercept of 1.46 nm, which is within experimental error of zero and suggests efficient nucleation.

Figure 39. Film thickness as a function of the number of deposition cycles at a growth temperature of 140 °C.

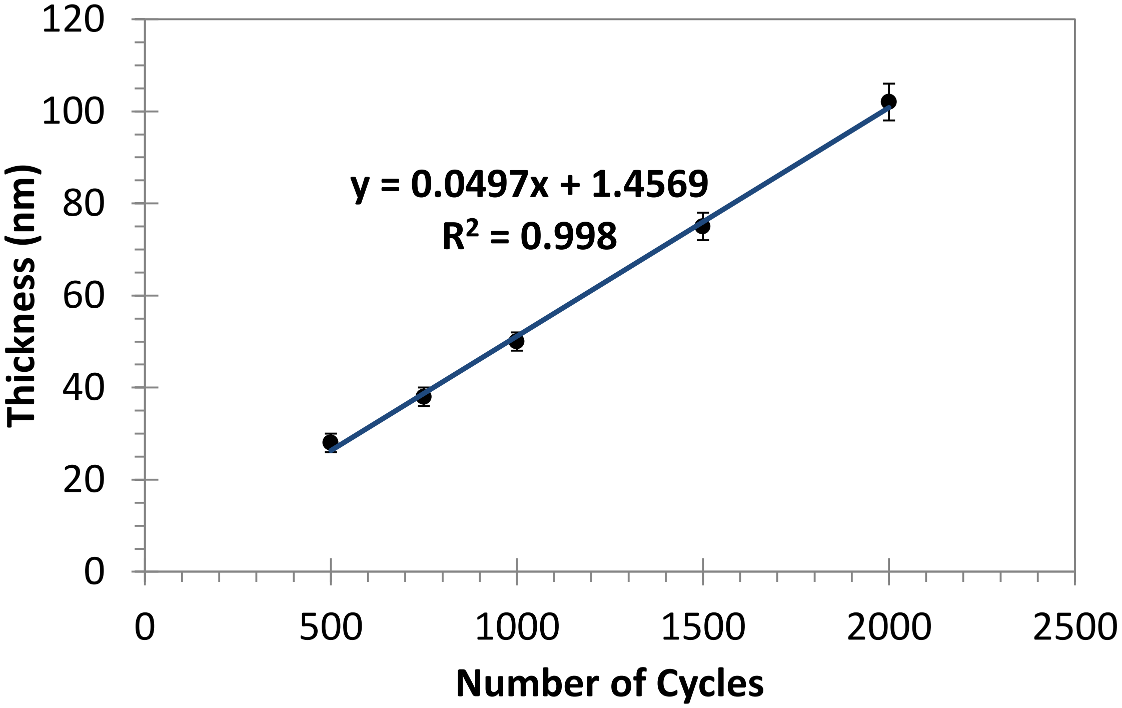

Time of flight-elastic recoil detection analysis (TOF-ERDA) was performed on 45-50 nm thick films grown at 100, 120, 140, 160, and 180 °C to probe the elemental compositions (Table 9). The atomic compositions of the films range from 95.9-98.8% copper, 0.1-1.2% carbon, 0.5-1.0% oxygen, ≤ 0.4% nitrogen, and ≤ 2.0% hydrogen. In general, the films had the highest purity at 100 °C and the lowest purity at 180 °C. Growth at the latter temperature may include some precursor self-decomposition, however, the uncertainties in the compositions preclude more definitive conclusions. Depth profiling studies demonstrate that the majority of the impurities reside at the film surface and at the interface between copper and the silicon substrate (Figure 40). The carbon, oxygen, and hydrogen impurities may arise from post-deposition exposure to ambient atmosphere, or from traces of formate that remain in the film.

Table 9. Percentages of C, O, N, and H in copper films obtained by TOF-ERDA.

Temp °C	**at % C**	**at % O**	**at % N**	**at %H**
100	0.1 ± 0.1	0.5 ± 0.2	≤ 0.1	< 0.5
120	1.0 ± 0.3	0.5 ± 0.2	0.2 ± 0.1	1.2 ± 0.5
140	0.5 ± 0.2	1.0 ± 0.3	0.15 ± 0.1	2.0 ± 0.5
160	0.9 ± 0.3	0.8 ± 0.3	0.15 ± 0.1	0.9 ± 0.4
180	1.2 ± 0.4	1.0 ± 0.3	0.4 ± 0.2	1.5 ± 0.5

Figure 40. TOF-ERDA depth profile of a 50 nm thick Cu film deposited at 120 °C.

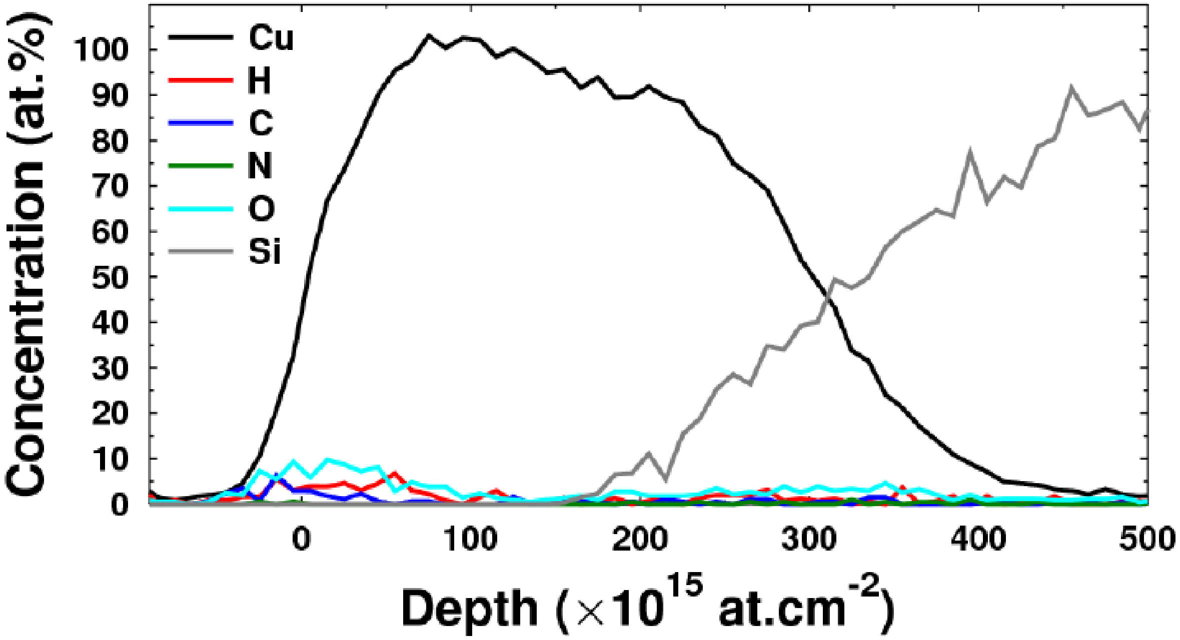

X-ray photoelectron spectroscopy was performed on 50 nm thick copper films deposited at 140 °C to assess the composition of the films (Figure 41). The surface of the as-deposited film showed the expected ionizations arising from metallic copper, as well as small ionizations from oxygen and carbon. Nitrogen concentrations were at or below the detection limit (< 1%). After argon ion sputtering, a constant composition of 95.1 at % copper, 1.2 at % carbon, 3.1 at % oxygen, and < 1 at % nitrogen was observed. The Cu $2p^{1/2}$ and Cu $2p^{3/2}$

ionizations appeared at 952.2 and 932.4 eV, which are exact matches for copper metal (Figure 42).[105]

Figure 41. XPS spectra of ALD Cu films deposited at 120 °C/1000 cycles.

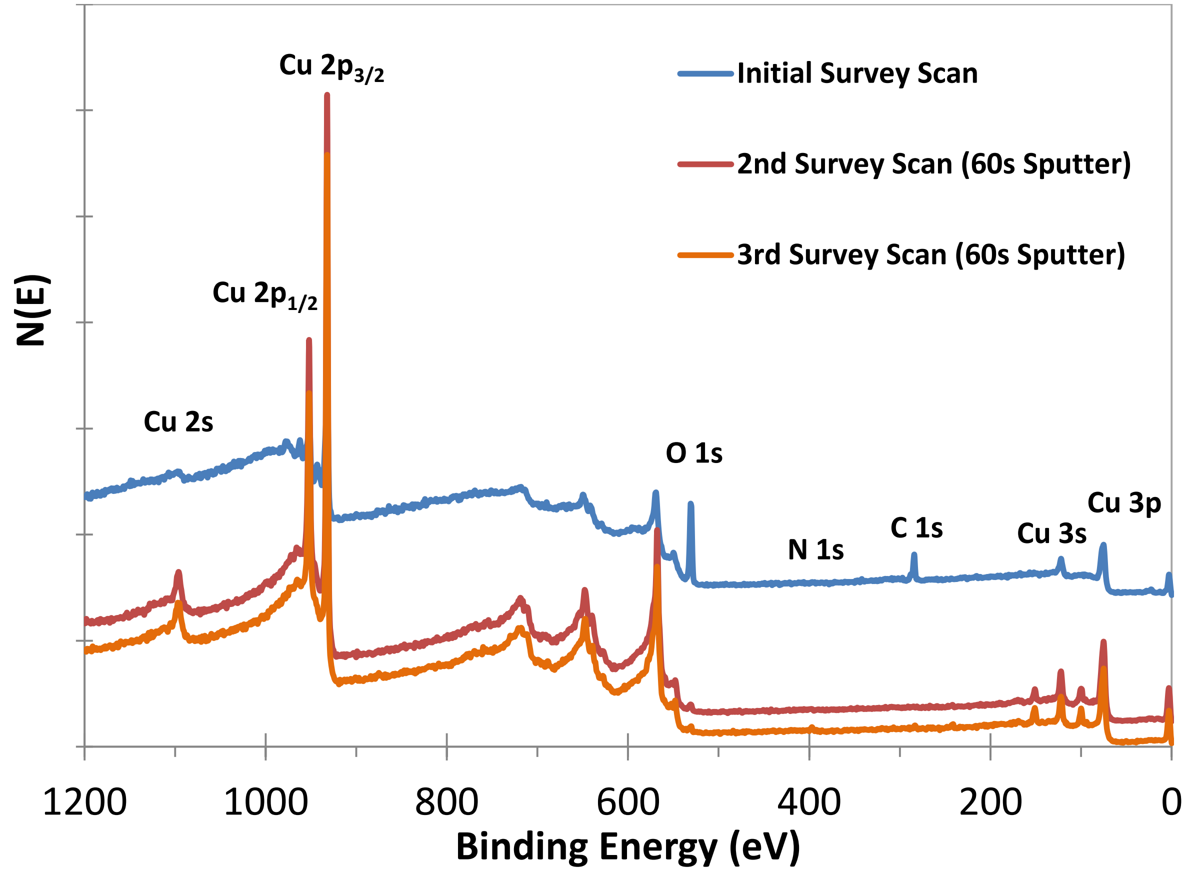

Figure 42. High-resolution XPS multiplex of Cu 2p region.

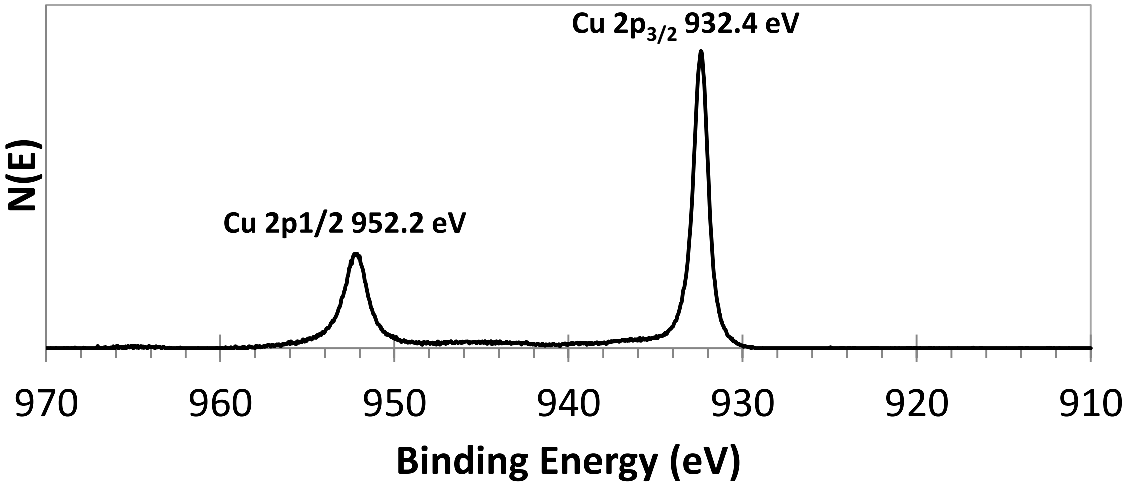

Powder X-ray diffraction experiments were performed on a 45 nm thick film deposited at 100 °C and on 50 nm thick films that were grown at 120, 140, 160, and 180 °C (Figure 43). All of the as-deposited films were crystalline, and showed reflections arising from the (111), (200), and (220) planes of copper metal (JCPDS file number 04-0836).

Figure 43. Powder X-ray diffraction profile of a 50 nm thick Cu film grown at 120 °C.

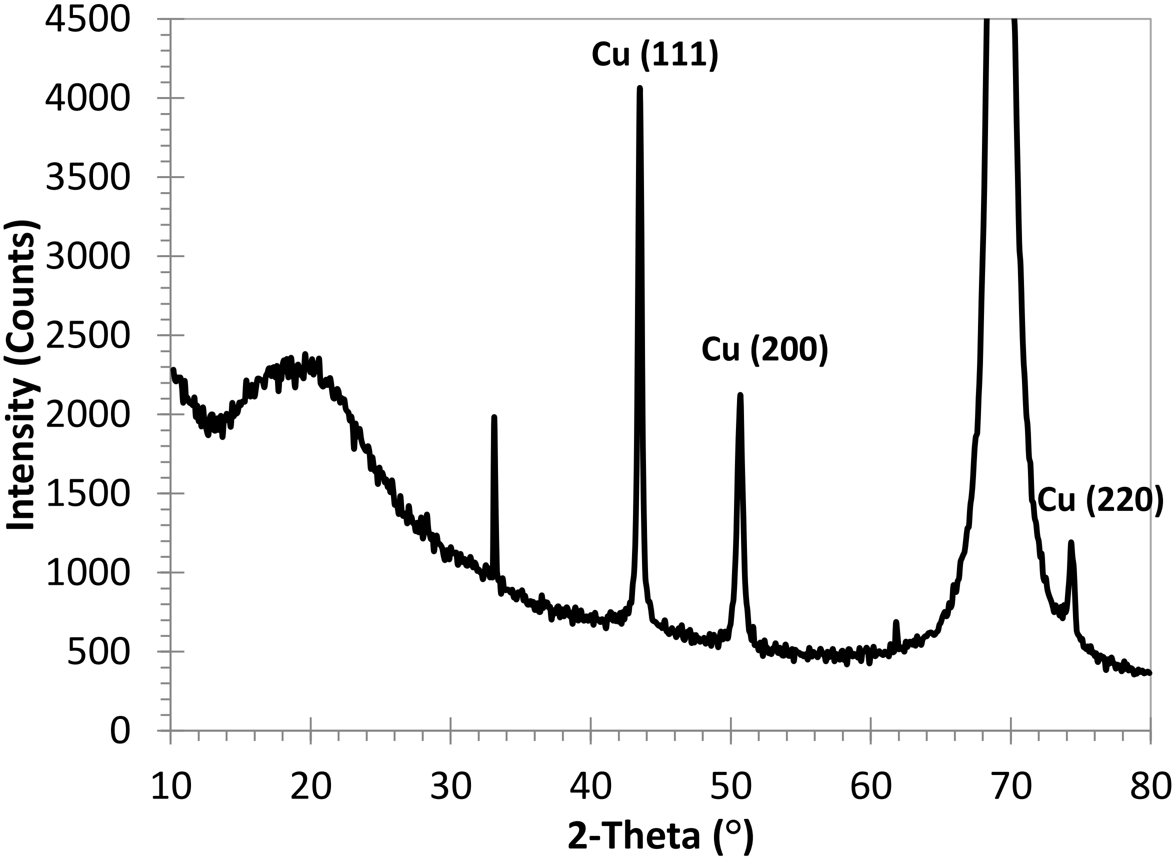

An AFM image of a 50 nm thick film grown at 120 °C had an RMS surface roughness of 3.5 nm (Figure 44). The SEM images of a film deposited under the same conditions showed no cracks or pinholes and a very uniform surface. The resistivities of 45-50 nm thick copper films deposited at 100, 120, and 140 °C ranged from 9.6 to 16.4 μΩ·cm at 20 °C, compared to the bulk resistivity of copper of 1.72 μΩ·cm at 20 °C. For comparison, sputtered 40-50 nm thick copper films on SiO_2 substrates had resistivities of 3-6 μΩ·cm.[106] Hence, our resistivity values indicate high purity copper metal. Films grown at all temperatures passed the Scotch Tape test, demonstrating good adhesion.

Figure 44. AFM image of ALD Cu film deposited at 120 °C/1000 cycles. (RMS roughness = 3.5 nm).

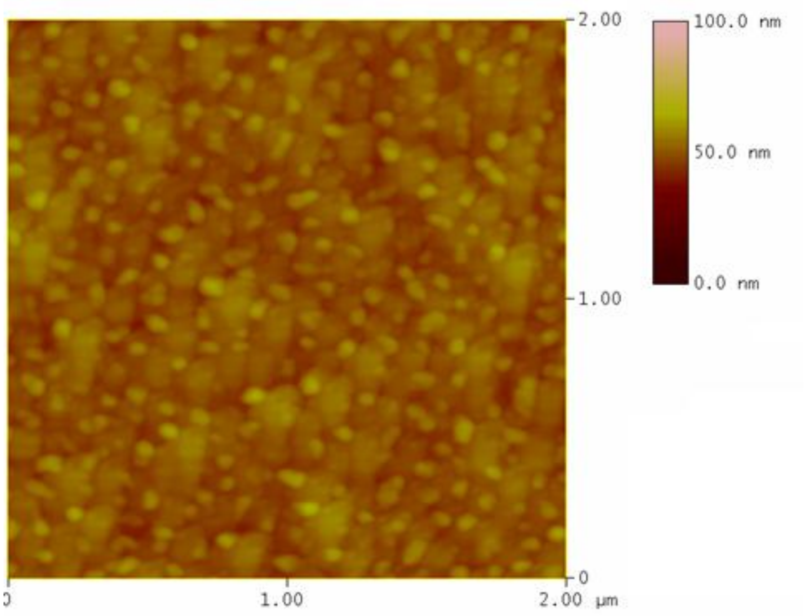

To understand the surface morphology and sheet resistivity as a function of film thickness, Cu films were grown at 100, 200, 400, and 800 cycles at 100 °C (Figures 45-49). FE-SEM surface views show that electrically discontinuous metal island growth (~25 nm wide/5 nm tall) occurs in the first 100 ALD cycles. From 10-20 nm (200-400 ALD cycles), a secondary and electrically continuous underlying Cu layer is formed while the surface Cu seeds remain. The uncertainty in measuring film thickness or particle height needs to be considered as there are Cu islands of varying height at films < 400 cycles. Sheet resistivities measured for 10 and 20 nm thick Cu films were 160 ± 4 μΩ·cm, and 54 ± 7.5 μΩ·cm at 20 °C, respectively. At thicknesses above 40 nm (> 800 cycles), the Cu films attains a denselypacked, highly granular morphology. The sheet resistivity at 20 °C for a 40 nm ALD Cu film was 16 ± 4 μΩ·cm. Cu island growth is due to poor nucleation on the substrate surface in the first few cycles. In order to improve Cu film quality at low thicknesses (low roughness and resistivity) advances in nucleation will need to occur.

Figure 45. Surface SEM views of ALD Cu films grown at 100 °C upon thermal SiO_2 after 100 cycles (5 nm thick).

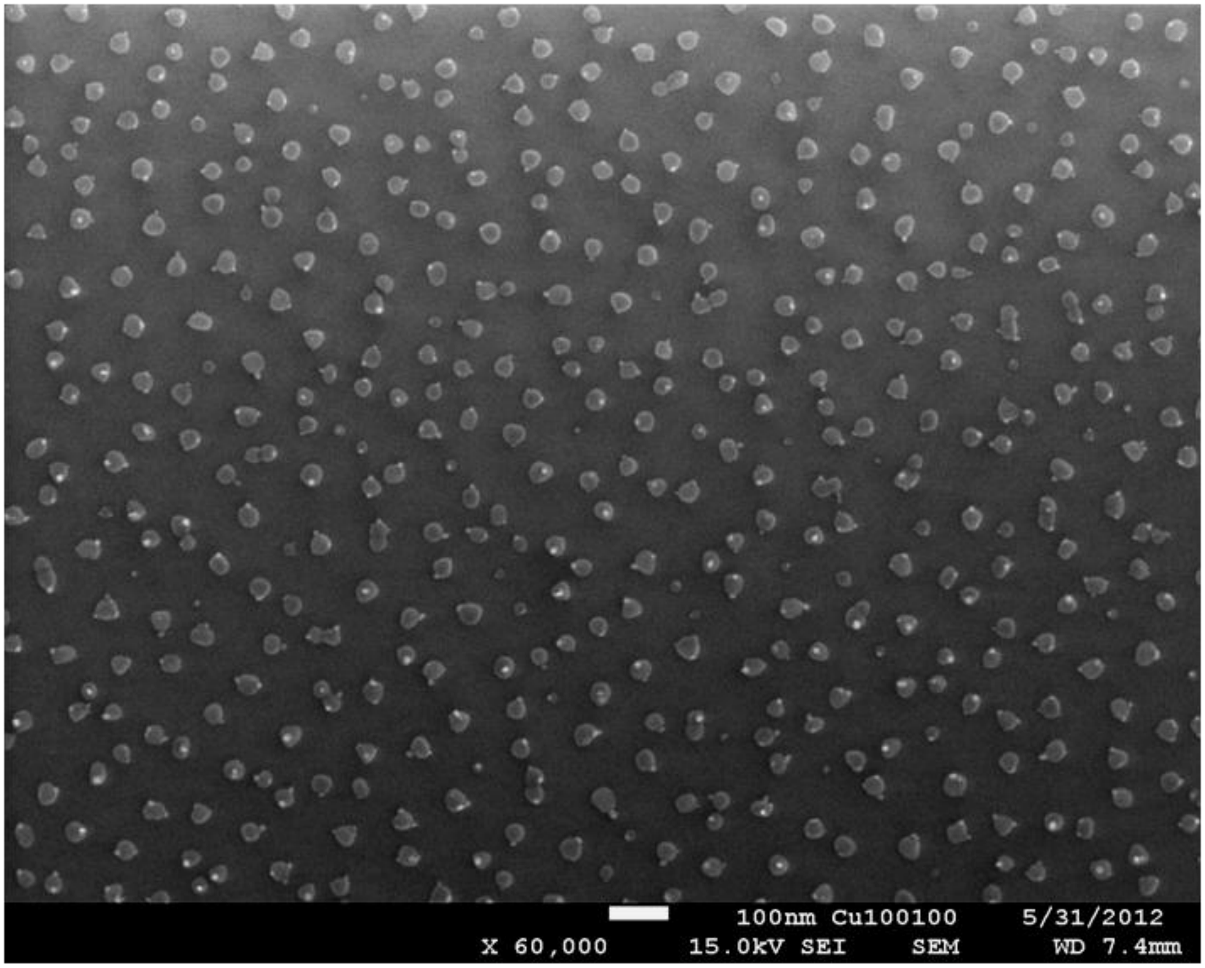

Figure 46. Surface SEM views of ALD Cu films grown at 100 °C upon thermal SiO_2 after 200 cycles (10 nm thick).

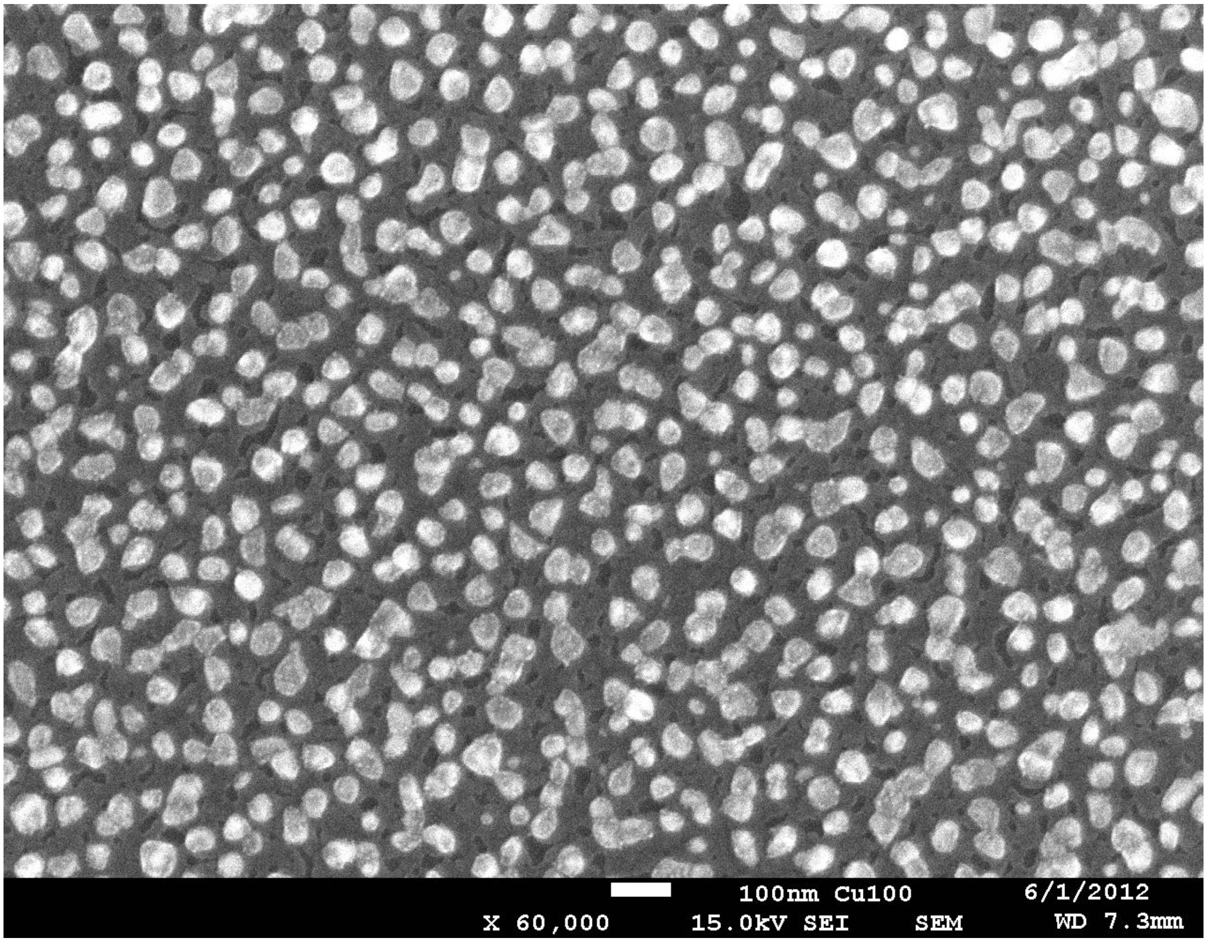

Figure 47. Surface SEM views of ALD Cu films grown at 100 °C upon thermal SiO_2 after 400 cycles (20 nm thick).

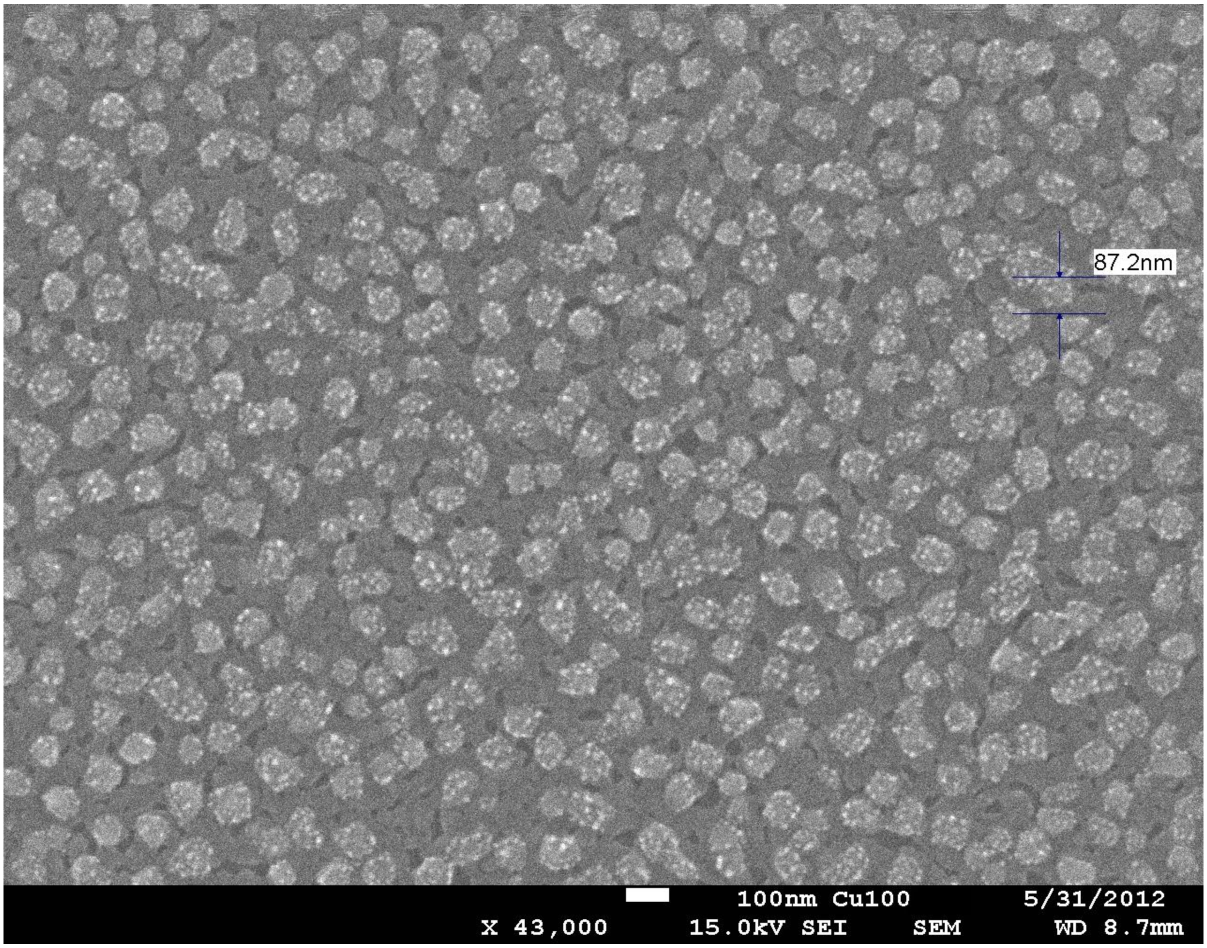

Figure 48. Surface SEM views of ALD Cu films grown at 100 °C upon thermal SiO_2 after 800 cycles (40 nm thick).

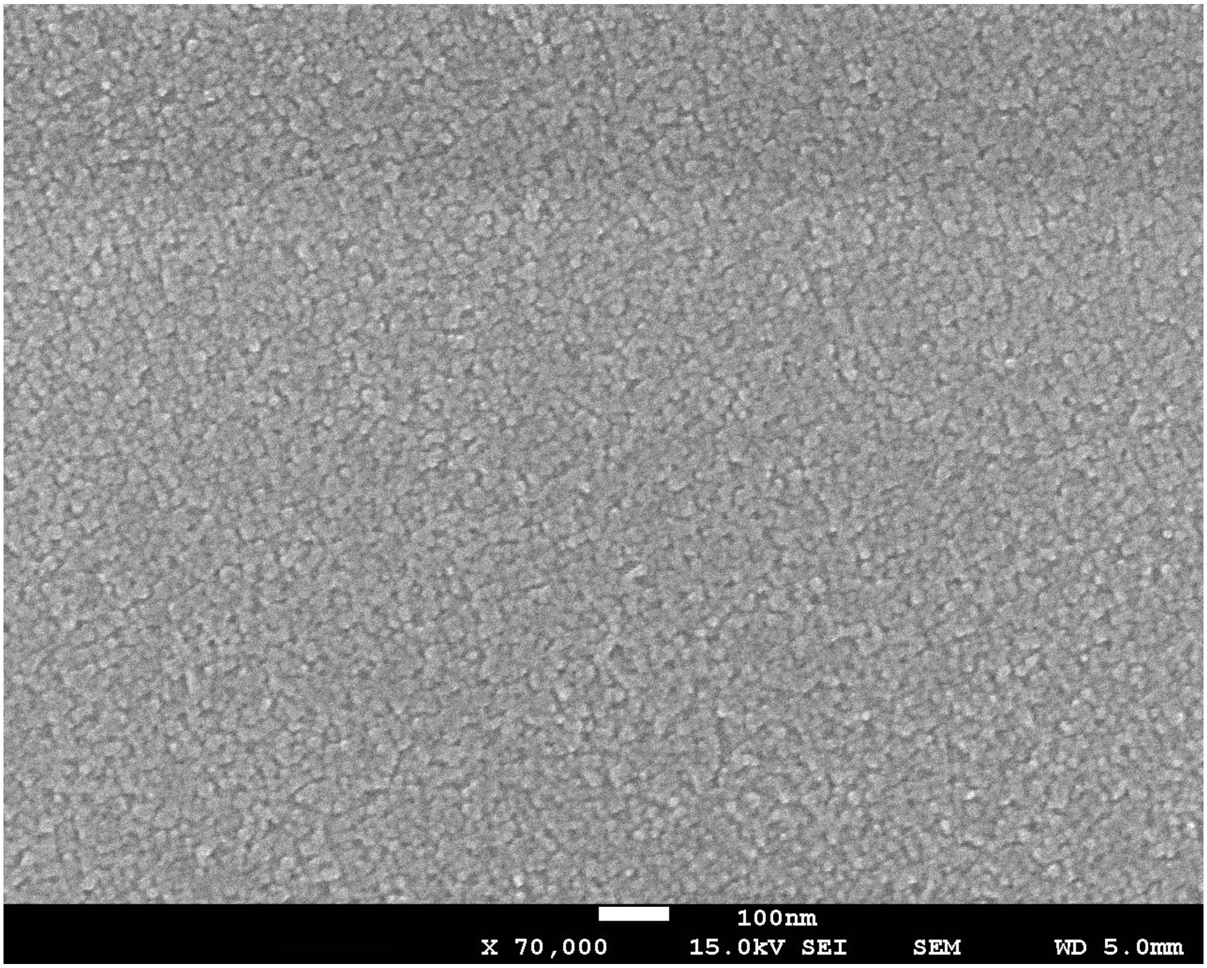

Figure 49. Measured sheet resistivity of ALD Cu films as a function of film thickness.

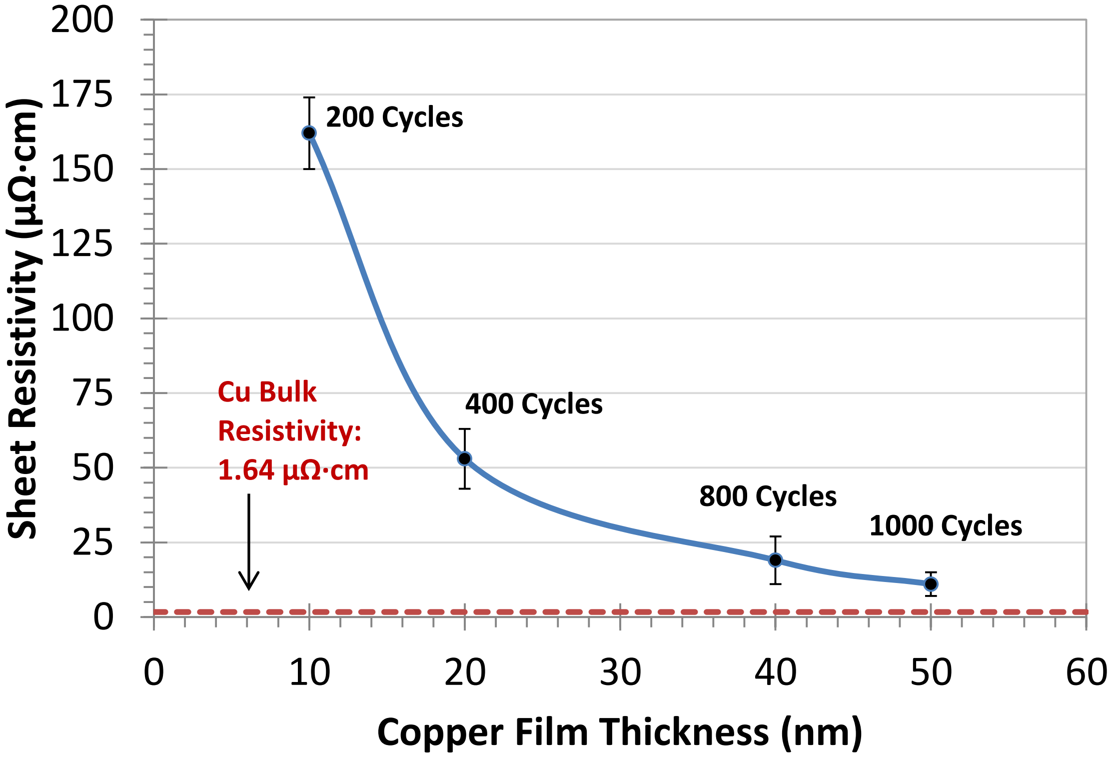

The best previous low temperature copper ALD process, entailing **6** and $ZnEt_2$, is reported to afford high purity copper films within the 100-120 °C ALD window.[62] However, a subsequent report documented a parasitic chemical vapor deposition (CVD) reaction of $ZnEt_2$ that leads to Zn incorporation into the copper films at temperatures between 120 and 150 °C.[63] In the latter study, the copper(II) pyrrolylaldiminate precursor had a minimum deposition temperature of 120 °C, but zinc is likely deposited even at 100-120 °C in processes that employ $ZnEt_2$. The process described herein avoids undesired elements in the precursors, and affords high purity, low resistivity copper metal at all growth temperatures that were examined. An SEM cross-sectional view illustrating the general scheme of film growth is given in Figure 50. Formic acid (pKa = 3.7[104]) is strongly acidic and should lead to very favorable protonation equilibria of the ligands in nearly all classes of commonly used metal precursors. Hence, treatment of a surface-bound metal precursor with formic acid should lead to rapid and efficient ligand removal and formation of a surface-bound metal formate. Formic acid has been previously employed in ALD to reduce Cu_2O films to copper metal,[73] but a ruthenium seed layer was required to catalyze the elimination of carbon dioxide from the surface formate species. Use of formic acid as a co-reagent in the CVD growth of copper metal films was demonstrated,[105] but films were deposited on ruthenium substrates that likely catalyze the decomposition of the surface formates. Preliminary experiments using acetic acid in place of formic acid also afforded copper metal with **6** and hydrazine, which implies that a range of other protic acids can be employed. If the film growth temperature is below the thermal decomposition point of the metal formate, then a subsequent hydrazine pulse leads to reduction to the metal, as exemplified by copper metal growth in the present work. Presumably, reducing co-reagents other than hydrazine can also be used. Metals such as ruthenium that can catalyze the low temperature elimination of carbon dioxide from formates may not require a reducing precursor. Recent results demonstrate that an analogous process entailing $Ni(dmap)_2$, formic acid, and hydrazine leads to nickel nitride thin films at a substrate temperature of 175 °C.[108] The reduction of the nickel(II) ion to nickel metal occurs at $E° = -0.25$ V,[84] which implies that low temperature ALD growth of metal films may be achieved with a metal precursor, a strong acid, and optional reducing reagent (as noted above) for metal ions with electrochemical potentials greater than that of the nickel(II) ion. Metal ions in this category include silver, gold, palladium, platinum, rhodium, iridium, rhenium, tungsten, and others.[84] ALD growth of many of these metals is well documented, but thermal ALD usually occurs at > 200 °C to provide enough activation energy to drive the ligand combustion reactions that occur with the oxygen co-reagent.[109-111]

Figure 50. Cross-sectional FE-SEM image illustrating the general scheme of Cu film growth upon thermal SiO_2.

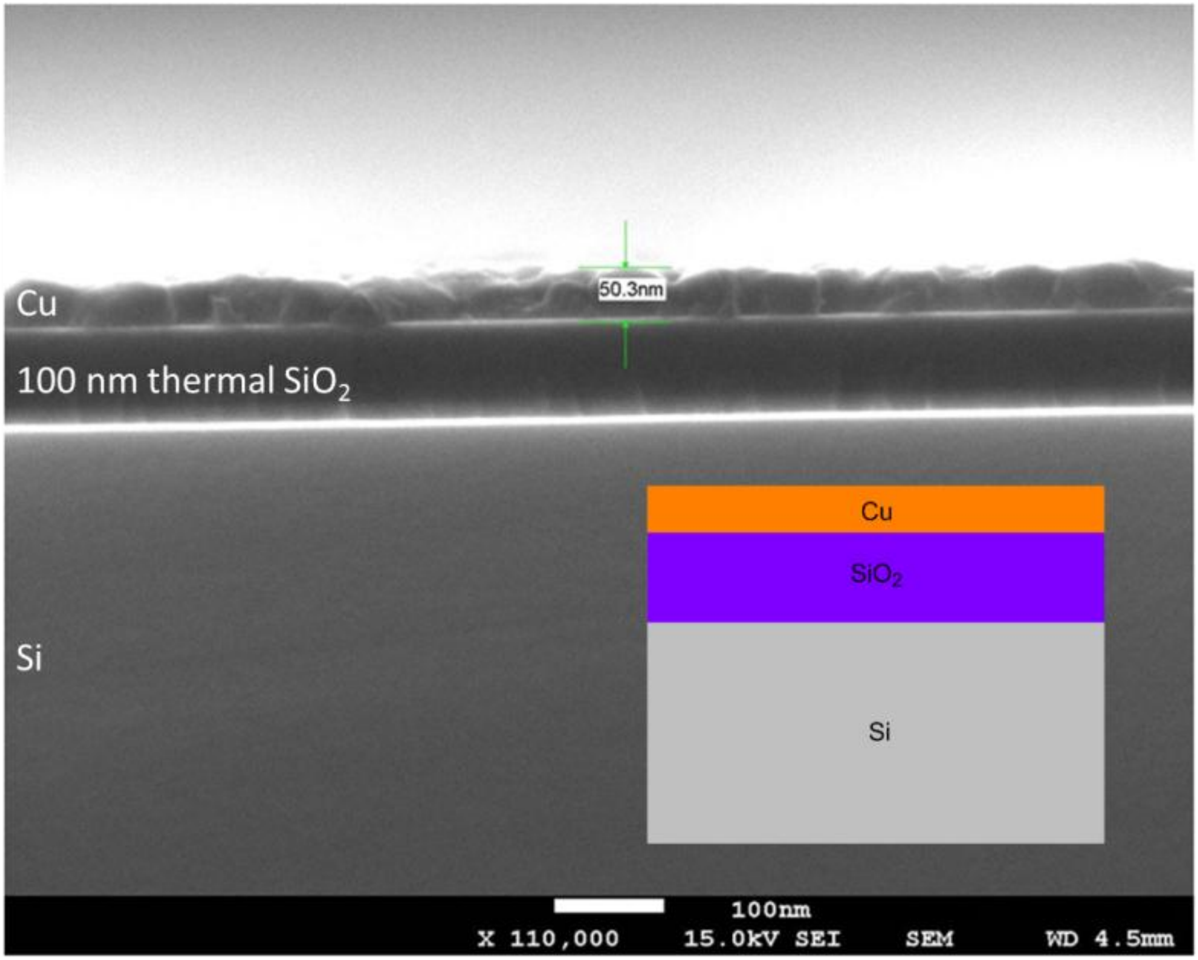

CHAPTER 5

Conclusions

A series of transition metal complexes containing radical anionic diazadienyl ligands has been synthesized, characterized, and their properties were investigated. These new complexes are volatile (sublimation temperatures of 80-120 °C/0.05 Torr), exceptionally thermally stable (decomposition temperatures of ≥ 230 °C), and thus could find use as viable CVD and/or ALD precursors. $Mn(tBu_2DAD)_2$ was shown to be the most thermally robust among the series, with a solid-state decomposition temperature of 325 °C and a sublimation temperature of 120 °C/0.05 Torr. X-ray crystal structure determinations revealed monomeric complexes that adopt tetrahedral coordination environments and ligand core bond lengths that were consistent with tBu_2DAD radical anion coordination. Thermogravimetric traces of all complexes gave single-step weight loss events from 150 to 225 °C with final percent residues ranging from 1.5 to 3.6% at 500 °C. Thermolysis studies reveal that all complexes decompose into their respective crystalline metal powders under inert atmosphere.

The study documented in Chapter 3 demonstrates the first account for the ALD growth of Ni_xN thin films. Growth of nickel nitride thin films was accomplished from bis(1,4-di-*tert*-butyl-1,3-diazabutadiene) nickel(II) ($Ni(tBu_2DAD)_2$) and 1,1-dimethylhydrazine. An ALD window was observed between 225 and 240 °C. The upper limit of ALD growth is due to the decomposition of **1** to nickel metal as determined by XRD. Films grown throughout the ALD window were moderately rough with RMS roughnesses ranging from 10.9-16.0 nm on films deposited from 225-250 °C. The affinity for nitride formation in this process is likely due to the use of 1,1-dimethylhydrazine. Further attempts to obtain nickel metal from this precursor should avoid the use of reducing sources containing nitrogen such as hydrazines, amines, or ammonia.

A low temperature process for the ALD of copper metal thin films is reported in Chapter 4 using a three precursor sequence entailing Cu(dmap)$_2$, formic acid, and hydrazine. A constant growth rate of 0.47-0.50 Å/cycle was observed on silicon wafers at process temperatures between 100 and 170 °C. Compositional analyses (XPS and TOF-ERDA) revealed copper films with low levels of carbon, oxygen, nitrogen, and hydrogen. Powder X-ray diffraction spectra of all films showed polycrystalline copper that is preferentially oriented towards the (111) plane. The resistivities of films grown between 100 and 140 °C ranged between 9.6 and 16.4 μΩ·cm, demonstrating the growth of low resistivity copper films. Cu film growth suffers from island growth in the first 200 ALD cycles. Subsequently, the Cu islands begin to coalesce to form continuous, dense, and granular films. Nucleation strategies will need to be developed to avoid island growth and to achieve film continuity at thicknesses less than 10 nm.

REFERENCES

1. Moore, G. E. *Electronics* **1965**, *38*, 33-35.
2. (a) Kim, H. *Surf. Coat. Technol.* **2006**, *200*, 3104-3111. (b) Kim, H. *J. Vac. Sci. Technol. B* **2003**, *21*, 2231-2261. (c) Merchant, S. M.; Kang, S. H.; Sanganeria, M.; van Schravendijk, B.; Mountsier, T. *JOM-J. Min. Met. Mater. Soc.* **2001**, *52*, 43-48. (d) Wang, S.-Q. *MRS Bull.* **1994**, *19*, 30-40.
3. Roule, A.; Amuntencei, M.; Deronzier, E.; Haumesser, P. H.; Da Silva, S.; Avale, X.; Pollet, O.; Baskaran, R.; Passemard, G. *Microelectron. Eng.* **2007**, *84*, 2610-2614. Goswami, I.; Laxman, R. **2004**, May 1st issue.
4. *International Technology Roadmap for Semiconductors*; 2011 and previous editions. http://public.itrs.net/.
5. (a) Winter, C. H. *Aldrichimica Acta* **2000**, 3-8. (b) Won, Y. S.; Kim, Y. S.; Anderson, T. J.; Reitfort, L. L.; Ghiviriga, I.; McElwee-White, L. *J. Am. Chem. Soc.* **2006**, *128*, 13781-13788. (c) McElwee-White, L. *Dalton Trans.* **2006**, 5327-5333. (d) Koh, W.; Kumar, D.; Li, W.-M.; Sprey, H.; Raaijmakers, I. J. *Solid St. Technol.* **2005**, *48*, 54-58. (e) Sim, H. S.; Kim, S.-I.; Kim, Y. T. *J. Vac. Sci. Technol. B.* **2003**, *21*, 1411-1414. (f) Lee, B. H.; Yong, K. *J. Vac. Sci. Technol. B* **2004**, *22*, 2375-2379. (g) Kelsey, J. E.; Goldberg, C.; Nuesca, G.; Peterson, G.; Kaloyeros, A. E.; Arkles, B. *J. Vac. Sci. Technol. B.* **1999**, *17*, 1101-1104.
6. (a) Haneda, M.; Iijima, J.; Koike, J. *Appl. Phys. Lett.* **2007**, *90*, 252107. (b) Usui, T.; Nasu, H.; Takahashi, S.; Shimizu, N.; Nishikawa, T.; Yoshimaru, M.; Shibata, H.;

Wada, M.; Koike, J. *IEEE Trans. Electron. Dev.* **2006**, *52*, 2492-2499. (c) Koike, J.; Wada, M. *Appl. Phys. Lett.* **2005**, *87*, 041911.

7. Chu, J. P.; Lin, C. H.; John, V.S. *Appl. Phys. Lett.* **2007**, *91*, 132109.
8. Barmak, K.; Cabral, C., Jr.; Rodbell, K. P.; Harper, J. M. E. *J. Vac. Sci. Technol. B.* **2006**, *24*, 2485-2498.
9. (a) Kang, S. H. *JOM* **2008**, *60*, 28-33. (b) Vaz, C. A. F.; Bland, J. A. C.; Lauhoff, G. *Rep. Prog. Phys.* **2008**, *71*, 056501. (c) Shiratsuchi, Y.; Yamamoto, M.; Bader, S. D. *Progr. Surf. Sci.* **2007**, *82*, 121-160.
10. (a) Leskelä, M.; Ritala, M. *Angew. Chem. Int. Ed.* **2003,** *42*, 5548-5554. (b) Niinistö, L.; Päiväsaari, J.; Niinistö, J.; Putkonen, M.; Nieminen, M. *Phys. Stat. Sol. A.* **2004**, *201*, 1443-1452. (c) Putkonen, M.; Niinistö, L. *Top. Organomet. Chem.* **2005**, *9*, 125-145. (d) Puurunen, R. L. *J. Appl. Phys.* **2005**, *97*, 121301. (e) George, S. M. *Chem. Rev.* **2010**, *110*, 111-131. (f) Knez, M.; Nielsch, K.; Niinistö, L. *Adv. Mater.* **2007**, *19*, 3425-3438.
11. (a) Mahan, J. E. *Physical Vapor Deposition of Thin Films*; John Wiley & Sons, Inc.: New York, New York, 2000. (b) Rossnagel, S. M. *J. Vac. Sci. and Technol. A.* **2003**, *21*, S74-S87.
12. (a) Pierson, H. O. *Handbook of Chemical Vapor Depostion (CVD)*; Noyes Publications/William Andrew Publishing: Norwich, New York, 1999. (b) Hitchman, M. L.; Jenson, K. F. *Chemical Vapor Deposition: Principles and Applications*; Academic Press: London, 1993. (c) Dobkin, D. M.; Zuraw, M. K. *Principles of Chemical Vapor Deposition*; Kluwer Academic Publishers: The Dordrecht, Netherlands, 2003.

13. (a) Knez, M.; Nielsch, K.; Niinistö, L. *Adv. Mater.* **2007**, *19*, 3425-3438. (b) Want, D.; Chang, Y.-L.; Wang, Q.; Cao, J.; Farmer, D. B.; Gordon, R. G.; Dai, H. *J. Am. Chem. Soc.* **2004**, *126*, 11602-11611. (c) Farmer, D. B.; Gordon, R. G. *Electrochem. Solid St. Lett.* **2005**, *8*, G89-G91. (d) van Embden, J.; Jasieniak, J.; Gómez, D. E.; Mulvaney, P.; Giersig, M. *Aust. J. Chem.* **2007**, *60*, 457-471. (e) Knez, M.; Kadri, A.; Wege, C.; Gösele, U.; Jeske, H.; Nielsch, K. *Nano Lett.* **2006**, *6*, 1172-1177. (f) Kucheyev, S. O.; Biener, J.; Wang, Y. M.; Baumann, T. F.; Wu, K. J.; van Buuren, T.; Hamzo, A. V.; Satcher, J. H., Jr.; Elam, J. W.; Pellin, M. J. *Appl. Phys. Lett.* **2005**, *86*, 083108. (g) Siwy, Z.; Trofin, L.; Kohli, P.; Baker, L. A.; Trautmann, C.; Martin, C. R. *J. Am. Chem. Soc.* **2005**, *127*, 5000-5001. (h) Kemell, M.; Pore, V.; Tupala, J.; Ritala, M.; Leskelä, M. *Chem. Mater*. **2007**, *19*, 1816-1820.

14. (a) Solehmainen, K.; Kapulainen, M.; Heimala, P.; Polamo, K. *IEEE Photonic Tech L.* **2004**, *16*, 194-196. (b) Graugnard, E.; Gaillot, D. P.; Dunham, S. N.; Neff, C. W.; Yamashita, T.; Summers, C. J. *Appl. Phys. Lett.* **2006**, *89*, 181108. (c) Gaillot, D. P.; Graugnard, E.; Blair, J.; Summers, C. J. *Appl. Phys. Lett.* **2007,** *91*, 181123. (d) Tan, L. K.; Gao, H.; Zong, Y.; Knoll, W. *J. Phys. Chem. C.* **2008**, *112*, 17576-17580. (e) Kumar, P.; Wiedmann, M. K.; Winter, C. H.; Avrutsky, I. *Appl. Optics* **2009**, *48*, 5407-5412.

15. (a) Yen, W. M.; Weber, M. J. *Inorganic Phosphors: Compositions, Preparation, and Optical Properties* CRC Press, **2004**. (b) Leskelä, M.; Koskentalo,T.; Blasse, G. *J. Solid State Chem.* **1985**, *89*, 272-279. (c) Schipper, W. J.; van der Voort, D.; van der Berg, P.; Vroon, Z. A. E. P.; Blasse, G. *Mater. Chem. Phys.* **1993**, *33*, 311-317. (d) Peterson, J. R.; Xu, W.; Dai, S. *Chem. Mater.* **1995**, *7*, 1686-1689. (e) Seo, H. J.; Moon,

B. K.; Kim, B. J.; Kim, J. B.; Tsuboi, T. *J. Phys. Condens. Mater.* **1999**, *11*, 7635-7644. (f) Pir, P. V.; Dotsenko, V. P.; Efryushina, N. P.; Berezovskaya, I. V. *Inorg. Mater.* **2006**, *42*, 901-907. (g) Chang, C.-K.; Chen, T.-M. *Appl. Phys. Lett.* **2007**, *91*, 081902. (h) Song, W.-S.; Kim, Y.-S.; Yang, H. *Mater. Chem. Phys.* **2009**, *117*, 500-503. (i) Pekgözlü, İ.; Karabulut, H. *Inorg. Mater.* **2009**, *45*, 61-64.

16. (a) Sun, D.-L.; Wu, A.-Y.; Yin, S.-T. *J. Am. Ceram. Soc.* **2008**, *91*, 169-173. (b) Luo, L.; Kuzminykh, Y.; Catalano, M.; R.; Malandrino, G.; Hoffman, P. *ECS Trans.* **2009**, *25*, 173-179. (c) Amaral, F.; Valente, M. A.; Costa, L. C. *J. Non-Cryst. Solids* **2010**, *356*, 822-827.
17. Profijt, H. B.; Potts, S. E.; van de Sanden, M. C. M.; Kessels, W. M. M. *J. Vac. Sci. Technol. A.* **2011**, *29*, 050801.
18. Sousa, P. M.; Silvestre, A. J.; Conde, O. *Thin Solid Films* **2011**, *519*, 3653-3657.
19. Lin, H.-T.; Nayak, P. K.; Wang, S.-C.; Chang, S.-Y.; Huang, J.-L. *J. Eur. Ceram. Soc.* **2011**, *31*, 2481-2487.
20. Goedde, D. M.; Windler, G. K.; Girolami, G. S. *Inorg. Chem.* **2007**, *46*, 2814-2823.
21. El-Kadri, O. M., Heeg, M. J.; Winter. C. H. *Dalton Trans*. **2006**, 4506-4513.
22. Knisley, T. J.; Saly, M. J.; Heeg, M. J.; Roberts, J. L.; Winter, C. H. *Organometallics* **2011**, *30*, 5010-5017.
23. Low, Y. H.; Bain, M. F.; Bien, D. C. S.; Montgomery, J. H.; Armstrong, B. M.; Gamble, H. S. *Microelectron. Eng*. **2006**, *83*, 2229-2233.
24. (a) Mathur, S.; Sivakov, V.; Shen, H.; Barth, S.; Cavelius, C.; Nilsson, A.; Kuhn, P. *Thin Solid Films* **2006**, *502*, 88-93. (b) Lin, Y.; Xu, Y.; Mayer, M. T.; Simpson, Z. I.; McMahon, G.; Zhou, S.; Wang, D. *J. Am. Chem. Soc.* **2012**, *134*, 5508-5511. (c)

Bachmann, J.; Jing J.; Knez, M.; Barth, S.; Shen, H.; Mathur, S.; Gösele, U.; Nielsch, K. *J. Am. Chem. Soc*. **2007**, *129*, 9554-9555.

25. Lie, M.; Klepper, K. B.; Nilsen, O.; Fjellvåg, H.; Kjekshus, A. *Dalton Trans*. **2008**, 253-259.
26. Scheffe, J. R.; Francés, A.; King, D. M.; Liang, X.; Branch, B. A.; Cavanagh, A. S.; George, S. M.; Weimer, A. W. *Thin Solid Films* **2009**, *517*, 1874-1879.
27. Martinson, A. B. F.; DeVries, M. J.; Libera, J. A.; Christensen, S. T.; Hupp, J. T.; Pellin, M. J.; Elam, J. W. *J. Phys. Chem. C*. **2011**, *115*, 4333-4339.
28. Kucheyev, S. O.; Biener, J.; Baumann, T. F.; Wang, Y. M.; Hamza, A. V.; Li, Z.; Lee, D. K.; Gordon, R. G. *Langmuir* **2008**, *24*, 943-948.
29. (a) *CRC Handbook of Chemistry and Physics*, 92nd ed.; CRC Press: Boca Raton, FL, 2011–2012; pp 5–80, 5–89. (b) Moon, D.-Y.; Han, D.-S.; Park, J.-H.; Shin, S.-Y.; Park, J.-W.; Kim, B. M.; Cho, J. Y. *Thin Solid Films* **2012**, *in press*, doi: 10.1016/j.tsf.2012.02.015.
30. Rizzi, G. A.; Zanoni, R.; Di Siro, S.; Perriello, L.; Granozzi, G. *Surf. Sci.* **2000**, *462*, 187-194.
31. Nakamura, T.; Tai, R.; Nishi, T.; Tachibara, K. *J. Electrochem. Soc.* **2005**, *152*, C584-C587.
32. Burton, B. B.; Fabreguette, F. H.; George. S. M.; *Thin Solid Films* **2009**, *517*, 5658-5665.
33. Nilsen, O.; Fjellvåg, H.; Kjekshus, A. *Thin Solid Films* **2003**, *444*, 44-51.
34. Nilsen, O.; Foss, S.; Fjellvåg, H.; Kjekshus, A. *Thin Solid Films* **2004**, *468*, 65-74.

35. (a) Sun, H.; Qin, X.; Zaera, F. *J. Phys Chem. Lett.* **2011**, *2,* 2525-2530. (b) Zaera, F. *J. Phys. Chem. Lett.*, **2012**, *3*, 1301–1309. (c) Qin, X.; Sun, H.; Zaera, F. *J. Vac. Sci. Technol. A.* **2012**, *30*, 01A112.

36. Au, Y.; Lin, Y.; Kim, H.; Beh, E.; Liu, Y.; Gordon, R. G. *J. Electrochem. Soc.* **2010**, *157*, D341-D345.

37. (a) Lutsev, L. V.; Stognij, A. I.; Novitskii, N. N. *Phys. Rev. B.* **2009**, *80*, 184423. (b) Theeuwen, S. *Appl. Phys. Lett*. **1999**, *75*, 3677-3679. (c) Sanyal, B.; Eriksson, O.; Arvidsson, P. I. *Phys. Rev. B.* **2008**, *77*, 155407. (d) Vo-Van, Chi; Kassir-Bodon, Z.; Yang, H.; Coraux, J.; Vogel, J.; Pizzini, S.; Bayle-Guillemaud, P.; Chshiev, M.; Guisset, V.; David, P.; Salvador, V.; Fruchart, O. *New J. Phys.* **2010**, *12*, 103040. (e) Fracassi, F.; d'Agostino, R.; Lamendola, R.; Filippo, A.; Rapisarda, C.; Vasquez, P. *J. Electrochem. Soc.* **1996**, *143*, 701-707.

38. (a) Seim, H.; Nieminen, M.; Niinistö, L.; Fjellvåg, H.; Johansson, L. S. *Appl. Surf. Sci.* 1997, *112*, 243-250. (b) Rooth, M.; Lindahl, E.; Harsta, A. *Chem. Vap. Depos.* **2006**, *12*, 209-213.

39. (a) Apatiga, L. M.; Castano, V. M. *Thin Solid Films* **2006,** *496*, 576-579. (b) Maruyama, T.; Nakai, T. *Sol. Energy Mater.* **1991**, *23*, 25-29. (c) Shalini, K.; Mane, A. U.; Shivashankar, S. A.; Rajeswari, M.; Choopun, S. *J. Cryst. Growth* **2001**, *231*, 242-247. (d) Burriel, M.; Garcia, G.; Santiso, J.; Abrutis, A.; Saltyte, Z.; Figueras, A. *Chem. Vap. Depos.* **2005**, *11*, 106-111. (e) Burriel, M.; Garcia, G.; Santiso, J.; Hansson, A. N.; Linderoth, S.; Figueras, A. *Thin Solid Films* **2005**, *473*, 98-103. (f) Fujii, E.; Torii, H.; Tomozawa, A.; Takayama, R.; Hirao, T. *J. Mater. Sci.* **1995**, *30*, 6013-6018. (g) Gulino, A.; Fragala, I. *Inorg. Chim. Acta* **2005**, *358*, 4466-4472. (h) Mane, A. U.;

Shalini, K.; Wohlfart, A.; Devi, A.; Shivashankar, S. A. *J. Cryst. Growth* **2002**, *240*, 157-163. (i) Mane, A. U.; Shivashankar, S. A. *J. Cryst. Growth* **2003**, *254*, 368-377.

40. Lee, H.-B.-R.; Kim, H. *Electrochem. Solid-State Lett*. **2006**, *9*, G323-G325.

41. Kim, K.; Lee, K.; Han, S.; Jeong, W.; Jeon, H. *J. Electrochem. Soc*. **2007**, *154*, H177-H181.

42. Lee, H.-B.-R.; Kim, J.; Kim, H.; Kim, W.-H.; Lee, J. W.; Hwang, I. *J. Korean Phys. Soc*. **2010**, *56*, 104-107.

43. Lee, H.-B.-R.; Kim, W.-H.; Lee, J. W.; Kim, J.-M.; Heo, K.; Hwang, I. C.; Park, Y.; Hong, S.; Kim, H. *J. Electrochem. Soc.* **2010**, *157*, D10-D15.

44. Kim, J.-M.; Lee, H.-B.-R.; Lansalot, C.; Dussarrat, C.; Gatineau, J.; Kim, H. *Jpn. J. Appl. Phys* **2010**, *49*, 05FA10.

45. Yoon, J.; Lee, H.-B.-R.; Kim, D.; Cheon, T.; Kim, S.-H.; Kim, H. *J. Electrochem. Soc*. **2011**, *158*, H1179-H1182.

46. (a) Kwon, J.; Saly, M.; Halls, M. D.; Kanjolia, R. K.; Chabal, Y. J. *Chem. Mater*. **2012**, *24*, 1025-1030. (b) Kwon, J.; Saly, M.; Kanjolia, R. K.; Chabal, Y. J. *Chem. Mater*. **2011**, *23*, 2068-2074.

47. (a) Burriel, M.; Garcia, G.; Santiso, J.; Abrutis, A.; Saltyte, Z.; Figueras, A. *Chem. Vap. Depos.*, **2005**, *11*, 106-111. (b) Klepper, K. B.; Nilsen, O.; Fjellvåg, H. *Thin Solid Films* **2007**, *515*, 7772-7781.

48. Kittl, J. A.; Lauwers, A.; Chamirian, O.; Van Dal, M.; Akheyar, A.; De Potter, M.; Lindsay, R.; Maex, K. *Microelectron. Eng.* **2003**, *70*, 158-165.

49. (a) Stauf, G. T.; Driscoll, D. C.; Dowben, P. A. *Thin Solid Films* **1987**, *153*, 421-430. (b) Ishikawa, M.; Kada, T.; Machida, H.; Ohshita, Y.; Ogura, A. *Jpn. J. Appl. Phys.* **2004**, *43*, L1833.

50. Lee, H.-B.-R.; Bang, S.-H.; Kim, W.-H.; Gu, G. H.; Lee, Y. K.; Chung, T.-M.; Kim, C. G.; Park, C. G; Kim, H. *Jpn. J. Appl. Phys.* **2010**, *49*, 05FA11.

51. (a) Powell, R. J.; Spicer, W. E. *Phys. Rev. B* **1970**, *2*, 2182-2193. (b) Fernandez, V.; Vettier, C.; de Bergevin, F.; Giles, C.; Nuebeck, W. *Phys. Rev. B.* **1998**, *57*, 7870-7876. (c) Spanke, D.; Solinus, V.; Knabben, D.; Hillebrecht, F. U.; Ciccacci, F.; Gregoratti, L.; Marsi, M. *Phys. Rev. B.* **1998**, *58*, 5201-5204. (d) Ohldag, H.; Scholl, A.; Nolting, F.; Anders, S.; Hillebrecht, F. U.; Stöhr, J. *Phys. Rev. Lett.* **2001**, *86*, 2878-2881.

52. (a) Ferreira, F. F.; Tabacniks, M. H.; Fantini, M. C. A.; Faria, I. C.; Gorenstein, A. *Solid State Ionics* **1996**, *86–88*, 971-976. (b) Fujii, E.; Tomozawa, A.; Torii, H.; Takayama, R. *Jpn. J. Appl. Phys.* **1996**, *35*, L328-L330. (c) Yeh, W.-C.; Matsumura, M. *Jpn. J. Appl. Phys.* **1997**, *36*, 6884-6887. (d) Kang, J.-K.; Rhee, S.-W. *Thin Solid Films* **2001**, *391*, 57-61. (e) Ahn, K.-S.; Nah, Y.-C.; Sung, Y.-E. *Appl. Surf. Sci.* **2002**, *199*, 259-269. (f) Min, K.-C.; Kim, M.; You, Y.-H.; Lee, S. S.; Lee, Y. K.; Chung, T.-M.; Kim, C. G.; Hwang, J.-H.; An, K.-S.; Lee, N.-S.; Kim, Y. *Surf. Coat. Technol.* **2007**, *201*, 9252-9255.

53. (a) Yang, T. S.; Cho, W.; Kim, M.; An, K.-S.; Chung, T.-M.; Kim, C. S.; Kim, Y. *J. Vac. Sci. Technol. A.* **2005**, *23*, 1238-1243. (b) Lu, H. L.; Wiemer, C.; Perego, M.; Spiga, S.; Fanciulli, M.; Pavia, G. *J. Electrochem. Soc*. **2008**, *155*, H807-H811. (c) Lindahl, E.; Ottosson, M.; Carlsson, J.-O. *Chem. Vap. Depos.* **2009**, *15*, 186-191. (d) Lindahl, E.; Ottosson, M.; Carlsson, J.-O. *Surf. Coat. Technol.* **2010**, *205*, 710-716. (e)

Chung, T.-M.; Lee, S. S.; Cho, W.; Lee, Y. K.; Hwang, J.-H.; An, K.-S.; Kim, C. G. *Bull. Korean Chem. Soc.* **2011**, *32*, 783-784.

54. (a) Lee, M.-J.; Seo, S.; Kim, D.-C.; Ahn, S.-E.; Seo, D. H.; Yoo, I.-K.; Baek, I.-G.; Kim, D.-S.; Byun, I.-S.; Kim, S.-H. *Adv. Mater.* **2007**, *19*, 73-76. (b) Seo, S.; Lee, M. J.; Seo, D. H.; Jeoung, E. J.; Suh, D.-S.; Joung, Y. S.; Yoo, I. K.; Hwang, I. R.; Kim, S. H.; Byun, I. S. *Appl. Phys. Lett.* **2004**, *85*, 5655-5657. (c) You, Y.-H.; So, B.-S.; Hwang, J.-H.; Cho, W.; Lee, S. S.; Chung, T.-M.; Kim, C. G.; An, K.-S. *Appl. Phys. Lett.* **2006**, *89*, 222105.
55. Chung, T.-M.; Lee, S. S.; Cho, W.; Kim, M.; Lee, Y. K.; Hwang, J.-H.; An, K.-S.; Kim, C. G. *Bull. Korean Chem. Soc*. **2011**, *32*, 783-784.
56. Min, K.-C.; Kim, M.; You, Y.-H.; Lee, S. S.; Lee, Y. K.; Chung, T.-M.; Kim, C. G.; Hwang, J.-H.; Lee, K.-S.; Kim, Y. *Surf. Coat. Tech*. **2007**, *201*, 9252-9255.
57. Arockiasamy, S.; Mallika, C.; Sreetharan, O. M.; Raghunathan, V. S.; Nagaraja, K. S. *Inorg. Chim. Acta*. **2009**, *362*, 1977-1983.
58. Kada, T.; Ishikawa, M.; Machida, H.; Ogura, A.; Ohshita, Y.; Soai, K. *J. Cryst. Growth* **2005**, *275*, E1115-E1119.
59. Malandrino, G.; Perdicaro, L. M. S.; Condorelli, G.; Fragalà, I. L.; Rossi, P.; Dapporto, P. *Dalton Trans*. **2006**, 1101-1106.
60. Li, Z.; Gordon, R. G.; Li H.; Shenai, D. V.; Lavoie, C. *J. Electrochem. Soc*. **2010**, *157*, H679-H683.
61. Bakovets, V. V.; Mitkin, V. N.; Gelfond, N. V. *Chem. Vap. Depos.* **2005**, *11*, 112-117.
62. Lee, B. H.; Hwang, J. K.; Nam, J. W.; Lee, S. U.; Kim, J. T.; Koo, S.-M.; Baunemann, A.; Fischer, R. A.; Sung, M. M. *Angew. Chem. Int. Ed.* **2009**, *48*, 4536-4539.

63. Vidjayacoumar, B.; Emslie, D. J. H.; Clendenning, S. B.; Blackwell, J. M.; Britten, J. F.; Rheingold, A. *Chem. Mater.* **2010**, *22*, 4844-4853.

64. Hsu, I. J.; McCandless, B. E.; Weiland, C.; Willis, B. G. *J. Vac. Sci. Technol. A.* **2009**, *27*, 660-667.

65. (a) Lim, B. S.; Rahtu, A.; Gordon, R. G. *Nature Mater.* **2003**, *2*, 748-754. (b) Li, Z.; Rahtu, A.; Gordon, R. G. *J. Electrochem. Soc.* **2006**, *153*, C787-C794. (c) Li, Z.; Gordon, R. G.; Farmer, D. B.; Lin, Y.; Vlassak, J. *Electrochem. Solid St. Lett.* **2005**, *8*, G182-G185.

66. Solanki, R.; Pathangey, B. *Electrochem. Solid St. Lett.* **2000**, *3*, 479-480.

67. Mårtensson, P.; Carlsson, J.-O. *Chem. Vap. Depos.* **1997**, ***3***, 45-50.

68. Juppo, M.; Ritala, M.; Leskelä, M. *J. Vac. Sci. Technol. A.* **1997**, *15*, 2330-2333.

69. Park, K.-H.; Bradley, A. Z.; Thompson, J. S.; Marshall, W. J. *Inorg. Chem.* **2006**, *45*, 8480-8482.

70. Thompson, J. S.; Zhang, L.; Wyre, J. P.; Brill, D. J.; Lloyd, K. G. *Thin Solid Films* **2009**, *517*, 2845-2850.

71. Huo, J.; Solanki, R. *J. Mater. Res.* **2002**, *17*, 2394-2398.

72. Li, Z.; Gordon, R. G. *Chem. Vap. Depos.* **2006**, *12*, 435-441.

73. Waechtler, T.; Ding, S.-F.; Hofmann, L.; Mothes, R.; Xie, Q.; Oswald, S.; Detavernier, C.; Schulz, S. E.; Qu, X.-P.; Lang, H.; Gessner, T. *Microelectronic Eng.* **2011**, *88*, 684-689.

74. Niskanen, A.; Rahtu, A.; Sajavaara, T.; Arstila, K.; Ritala, M.; Leskelä, M. *J. Electrochem. Soc.* **2005**, *152*, G25-G28.

75. Moon, D.-Y.; Han, D.-S.; Shin, S.-Y.; Park, J.-W.; Kim, B. M.; Kim, J. H. *Thin Solid Films* **2011**, *519*, 3636-3640.

76. Gardiner, M. G.; Hanson, G. R.; Henderson, M. J.; Lee F. C.; Raston, C. L. *Inorg. Chem.* **1994**, *33*, 2456-2461.

77. (a) Ghosh, M.; Sproules, S.; Weyhermüller, T.; Wieghardt, K. *Inorg. Chem.* **2008**, *47*, 5963-5970. (b) Kreisel, K. A.; Yap, G. P. A.; Theopold, K. H. *Inorg. Chem.* **2008**, *47*, 5293-5303. (c) Kreisel, K. A.; Yap, G. P. A.; Dmitrenko, O.; Landis, C. R.; Theopold, K. H. *J. Am. Chem. Soc.* **2007**, *129*, 14162-14163.

78. Ghosh, M.; Weyhermüller, T.; Wieghardt, K. *Dalton Trans.* **2008**, 5149-5151.

79. (a) Khusnivarov, M. M.; Weyhermüller, T.; Bill, E.; Wieghardt, K. *J. Am. Chem. Soc.* **2009**, *131*, 1208-1221. (b) Khusnivarov, M. M.; Weyhermüller, T.; Bill, E.; Wieghardt, K. *Angew. Chem. Int. Ed.* **2008**, *47*, 1228-1231. (c) Muresan, N.; Lu, C. C.; Ghosh, M.; Peters, J. C.; Abe, M.; Henling, L. M.; Weyhermöller, T.; Bill, E.; Wieghardt, K. *Inorg. Chem.* **2008**, *47*, 4579-4590. (d) Bart, S. C.; Hawrelak, E. J.; Lobkovsky, E.; Chirik, P. *Organometallics* **2005**, *24*, 5518-5527. (e) tom Dieck, H.; Diercks, R.; Stamp, L.; Bruder, H.; Schuld, T. *Chem. Ber.* **1987**, *120*, 1943-1950. (f) tom Dieck, H.; Bruder, H. *J. Chem. Soc., Chem. Commun.* **1977**, 24-25.

80. (a) Muresan, N.; Weyhermüller, T.; Wieghardt, K. *Dalton Trans.* **2007**, 4390-4398. (b) Muresan, N.; Chlopek, K.; Weyhermüller, T.; Neese, F.; Wieghardt, K. *Inorg. Chem.* **2007**, *46*, 5327-5337. (c) Khusnivarov, M. M.; Harms, K.; Burghaus, O.; Sundermeyer, J. *Eur. J. Inorg. Chem.* **2006**, 2985-2996. (d) Gorls, H.; Walther, D.; Sieler, J. *Cryst. Res. Technol.* **1987**, *22*, 1145-1151. (e) Svoboda, M.; tom Dieck, H.; Kruger, C.; Tsay, Y.-H. *Z. Naturforsch.* **1981**, *36b*, 814-822. (f) Robinson, M. A.; Curry, J. D.; Busch, D.

H. *Inorg. Chem.* **1963**, *2*, 1178-1181. (g) Kaltsoyannis, N. *J. Chem. Soc., Dalton Trans.* **1996**, 1583-1589.

81. Greenwood, N. N.; Earnshaw, A. *Chemistry of the Elements*; Second Edition; Butterworth-Heinemann: Oxford, 1997; pp. 1004, 1074, 1115, 1148.
82. (a) Allan, L. E. N.; Shaver, M. P.; White, A. J. P.; Gibson, V. C. *Inorg. Chem.* **2007**, *46*, 8963-8970. (b) Barral, M. C.; Delgado, E.; Gutíerrez-Puebla, E.; Jimenez-Aparicio, R.; Monge, A.; del Pino, C.; Santos, A. *Inorg. Chim. Acta* **1983**, *74*, 101-107. (c) Jameson, G. B.; Oswald, H. R.; Beer, H. R. *J. Am. Chem. Soc.* **1984**, *106*, 1669-1675.
83. (a) Saly, M. J.; Munnik, F.; Winter, C. H. *J. Mater. Chem.* **2010**, *20*, 9995-10000. (b) Saly, M. J.; Munnik, F.; Baird, R. J.; Winter, C. H. *Chem. Mater.* **2009**, *21*, 3742-3744. (c) Saly, M. J.; Munnik, F.; Winter, C. H. *Chem. Vap. Depos.* **2011**, *17*, 128-134. (d) Wiedmann, M. K.; Karunarathne, M. C.; Baird, R. J.; Winter, C. H. *Chem. Mater.* **2010**, *22*, 4400-4405. (e) Saly, M. J.; Heeg, M. J.; Winter, C. H. *Inorg. Chem.* **2009**, *48*, 5303-5312. (f) Wiedmann, M. K.; Heeg, M. J.; Winter, C. H. *Inorg. Chem.* **2009**, *48*, 5382-5391.
84. *CRC Handbook of Chemistry and Physics*, 92nd Edition, **2011-2012**, pp 5-80, 5-89.
85. Rushworth, S. A.; Smith, L. M.; Kingsley, A. J.; Odedra, R.; Nickson, R.; Hughes, P. *Microelectronics Reliab.* **2005**, *45*, 1000-1002.
86. Vidjayacoumar, B.; Emslie, D. J. H.; Blackwell, J. M.; Clendenning, S. B.; Britten, J. F. *Chem. Mater*. **2010**, *22*, 4854-4866.
87. (a) Cheon, J.; Rogers, D. M.; Girolami, G. S. *J. Am. Chem. Soc.* **1997**, *119*, 6804-6813. (b) Entley, W. R.; Treadway, C. R.; Wilson, S. R.; Girolami, G. S. *J. Am. Chem. Soc*.

1997, *119*, 6251-6258. (c) Tagge, C. D.; Simpson, R. D.; Bergman, R. G.; Hostetler, M. J.; Girolami, G. S.; Nuzzo, R. G. *J. Am. Chem. Soc*. **1996**, *118*, 2634-2643.

88. Zhang, Y. P.; Yuan, Z.; Puddephatt, R. J. *Chem. Mater*. **1998**, *10*, 2293-2300.
89. Xu, H. Y.; Xu, S. L.; Wang, H.; Yan, H. *J. Electrochem. Soc.* **2005**, *152*, C803-C807.
90. (a) Li, Z.; Barry, S. T.; Gordon, R. G. *Inorg. Chem.* **2005**, *44*, 1728-1735. (b) Lim, B. S.; Rahtu, A.; Gordon, R. G. *Nature Mater.* **2003**, *2*, 749-754. (c) Lim, B. S.; Rahtu, A.; Park, J. S.; Gordon, R. G. *Inorg. Chem.* **2003**, *42*, 7951-7958.
91. Reedijk, J.; Groeneveld, W. L. *Recl. Trav. Chim. Pays-Bas* **1968**, *87*, 552-558.
92. Kliegman, J. M.; Barnes, R. K. *Tetrahedron*, **1970**, *26*, 2555-2560.
93. Evans, D. F. *J. Chem. Soc.* **1959**, 2003-2005.
94. APEX II collection and processing programs are distributed by the manufacturer, Bruker AXS Inc., Madison, WI, USA, **2009**.
95. Sheldrick, G. M. *Acta Crystallogr., Sect. A: Found. Crystallogr.* **2008**, *64*, 112-122.
96. (a) Lingwal, V.; Panwar, N. S. *J. Appl. Phys*. **2005,** *97*, 104902. (b) Pérez-Rigueiro, J.; Jiménez, C.; Pérez-Casero, R.; Martínez-Duart J. M. *J. Appl. Phys*. **1997**, *81*, 781-785. (c) Cantwell, P. R.; U. Gibson, J.; Allwood, D. A.; Macleod, H. A. M. *J. Appl. Phys.* **2006,** *100*, 093910. (d) Zhou, J. N.; Rar, A.; Otte, D.; Barnard, J. A. *J. Appl. Phys.* **2000**, *88*, 1880. (e) J. Choi, E. G. Gillian, Inorg. Chem. **48**, 4470 (2009). (f) J. Zheng, R. Yang, W. Chen, L. Xie, X. Li, C. Chen, J. Phys D: Appl. Phys. **42**, 185209 (2009). *J. Appl. Phys.* **2000**, *88*, 1880-1885. (g) Maya, L. *J. Vac. Sci. Technol. A* **1993**, *11*, 604-608. (h) Sun, Q.; Fu, Z.-W. *Electrochem. Solid-State Lett.* **2007**, *10*, A189-A193. (i) Fu, Z.-W.; Wang, Y., Yue, X.-L.; Zhao, S.-L.; Qin, Q.-Z. *J. Phys. Chem. B.* **2004**, 108, 2236-2244. (j) Desmoulins-Krawiec, S.; Aymonier, C.; Loppinet-Serani, A.; Weill, F.;

Gorsse, S.; Etourneau, J.; Cansell, F. *J. Mater. Chem.* **2004**, *14*, 228-232. (k) Choi, J.; Gillan, E. G. *Inorg. Chem.* **2005**, *44*, 7385-7393. (l) Törndahl, T.; Ottosson, M.; Carlsson, J.-O. *J. Electrochem. Soc.* **2006**, *153*, C146-C151. (m) Modin, A.; Kvashnina, K. O.; Butorin, S. M.; Werme, L.; Nordgren, J.; Arapan, S.; Ahuja, R.; Fallberg, A.; Ottosson, M. *J. Phys.: Condens. Matter* **2008**, *20*, 235212.

97. (a) Gillot, F.; Oró-Solé, J.; Palacín, M. R. *J. Mater. Chem.* **2011**, *21*, 9997-10002. (b) Gajbhiye, N. S.; Ningthoujam, R. S.; Weissmüller, J. *Phys. Stat. Sol.* **2002**, *189*, 691-695. (c) Wang, Y.; Fu, Z.-S.; Yue, X.-L.; Qin, W.-Z. *J. Electrochem. Soc.* **2004**, *151*, E162-E167

98. Baiker, A.; Maciejewski, M. *J. Chem. Soc., Faraday Trans.* **1984**, *80*, 2331-2341.

99. Neklyudov, I. M.; Morozov, A. N. *Physica B.* **2004**, *350*, 325-337.

100. (a) Lindahl, E.; Ottosson, M.; Carlsson, J.-O. *ECS Trans.* **2009**, *25*, 365-372. (b) Vempaire, D.; Fettar, F.; Ortega, L.; Pierre, F.; Miraglia, S.; Sulpice, A.; Pelletier, J.; Hlil, E. K.; Fruchart, D. *J. Appl. Phys.* **2009,** *106*, 073911. (c) Popović, N.; Bogdanov, Ž.; Goncić, B.; Štrbac, S.; Rakočević, Z. *Appl. Surf. Sci.* **2009**, *225*, 4027-4032. (d) Tarasenko, A. A.; Jastrabík, L.; Chvostova, D.; Sobota, J. *Thin Solid Films*, **1998**, *313-314*, 314-318. (e) Maya, L. *J. Vac. Sci. Technol. A.* **1993,** *11*, 604-608. (f) Kuznetsov, D. L.; Ugodnikov, G. G.; Filatov, I. E. *Tech. Phys. Lett.* **2008**, *34*, 87-89. (g) Vempaire, D.; Miraglia, S.; Sulpice, A.; Ortega, L.; Hlil, E. K.; Fruchart, D.; Pelletier, J. *J. Magn. Magn. Mater.* **2004**, *272-276*, e843-e844.

101. Goel, S. C.; Kramer, K. S.; Chiang, M. Y.; Buhro, W. E. *Polyhedron* **1990**, *9*, 611-613.

102. Becker, R.; Devi, A.; Weiss, J.; Weckenmann, U.; Winter, M.; Kiener, C.; Becker, H.-W.; Fischer, R. A. *Chem. Vap. Depos.* **2003**, *9*, 149-156.

103. We determined that **1** has a melting point of 139-141 °C, sublimes on a preparative scale (~ 1 g) at 90 °C/0.05 Torr in ~ 4 hours with 89% sublimed recovery and 3% non-volatile residue, and undergoes solid state thermal decomposition between 185 and 188 °C.

104. Ravindranathan, P.; Patil, K. C. *Thermochim. Acta* **1983**, *71*, 53-57.

105. *Handbook of X-ray Photoelectron Spectroscopy*; Wagner, C. D.; Riggs, W. M.; Davis, L. E.; Moulder, J. F.; Murlenberg, G. E., Perkin-Elmer Corporation: Eden Prairie, Minnesota; **1979**, pp. 81-82.

106. Zhang, W.; Brongersma, S. H.; Richard, O.; Brijs, B.; Palmans, R.; Froyen, L.; Maex, K. *Microelectron. Eng.* **2004**, *76*, 146-152.

107. *CRC Handbook of Chemistry and Physics*; 92nd Ed.; **2011-2012**; p. 5-94.

108. *Unpublished Results*

109. Song, H.; Norman, J. A. T.; Shimogaki, Y. *Microelectronics Eng.* **2010**, *87*, 249-253.

110. Aaltonen, T.; Ritala, M.; Tung, Y.-L.; Chi, Y.; Arstila, K.; Meinander, K.; Leskelä, M. *J. Mater. Res.* **2004**, *19*, 3353-3358.

111. Knapas, K.; Ritala, M. *Chem. Mater.* **2011**, *23*, 2766-2771.

ABSTRACT

NEW PRECURSORS AND CHEMISTRY FOR THE GROWTH OF TRANSITION METAL FILMS BY ATOMIC LAYER DEPOSITION

by

THOMAS JOSEPH KNISLEY

December 2012

Advisor: Dr. Charles H. Winter

Major: Chemistry (Inorganic)

Degree: Doctor of Philosophy

The advancing complexity of advanced microelectronic devices is placing rigorous demands on currently used PVD and CVD deposition techniques. The ALD deposition method is proposed to meet the film thickness and conformality constraints needed by the semiconductor industry in future manufacturing processes. Unfortunately, there is a limited number of chemical precursors available that have high thermal stability, reactivity, and vapor pressure suitable for ALD film growth to occur. These properties collectively contribute to the lack of suitable transition metal precursors available for use in ALD. In this thesis, the discovery of a series of novel transition metal diazadienate precursors that promising properties deemed suitable for ALD is reported. The volatility and thermal stability of the new transition metal diazadienyl compounds were studied by preparative sublimation and capillary tube melting point/decomposition experiments. Thermogravimetric analyses (TGA) demonstrate precursor residues of less than 4% at 500 °C. In addition, sublimation data, melting points, and decomposition temperatures for all complexes are presented. The manganese diazadienyl complex has the highest decomposition temperature of the series of complexes produced (325 °C). During preparative sublimations, the product

recoveries of all transition metal diazadienyl complexes were greater than 92.0% with nonvolatile residues of less than 7.0%. This is an excellent indication that these complexes may be suitable candidates as metal precursors for ALD.

Nickel nitride (Ni_xN) films have been studied as an intermediate material for the formation of both nickel metal and nickel silicide using chemical vapor deposition. Herein, the ALD growth of nickel nitride thin films from bis(1,4-di-*tert*-butyl-1,3-diazabutadiene) nickel(II) ($Ni(tBu_2DAD)_2$) and 1,1-dimethylhydrazine, is described. An ALD window for the deposition of nickel nitride films on 500 nm thermal SiO_2 substrates was observed between 225 and 240 °C with a constant growth rate of 0.70 Å/cycle. X-Ray photoelectron spectroscopy (XPS) showed all expected ionizations with carbon concentrations below the detection limit after argon ion sputtering. Due to preferential nitrogen sputtering in XPS, Rutherford backscattering spectrometry (RBS) and nuclear reaction analysis (NRA) were performed and subsequently revealed Ni:N ratios between 2–4 for films deposited within the ALD window. AFM measurements revealed a RMS roughness value of 10.8 nm on an as-deposited film at 225°C. All as-deposited films were amorphous as determined by X-ray diffraction.

Copper is the primary interconnect material in microelectronics devices, due to its high conductivity and low affinity towards electromigration. With transistor gate lengths scheduled to reach 14 nm by 2014, there are severe demands upon the current film growth techniques used in device fabrication. The ALD film growth method is ideally suited for future microelectronics manufacturing, since it inherently provides highly conformal thin films, even in high aspect ratio nanoscale features, and allows sub-nanometer control over film thicknesses. In Chapter 4, the atomic layer deposition of high purity, low resistivity copper metal thin films using a three precursor sequence entailing Cu(dmap)$_2$, formic acid, and hydrazine, is presented. In this process, Cu(dmap)$_2$ is unreactive towards hydrazine but is transformed to copper(II) formate, which is then readily reduced to copper metal by subsequent hydrazine exposure. The present work therefore addresses a central problem with the ALD growth of metal thin films: low reactivity of metal precursors toward common reducing agents. A constant growth rate of 0.47-0.50 Å/cycle upon prime grade Si(100) was observed at substrate temperatures between 100 and 170 °C. Compositional analyses (XPS and TOF-ERDA) revealed copper films with low levels of carbon, oxygen, nitrogen, and hydrogen. Powder X-ray diffraction spectra of all films showed polycrystalline copper. The resistivities of films grown between 100 and 140 °C ranged between 9.6 and 16.4 μΩ·cm, demonstrating the growth of high purity, low resistivity copper films. An AFM measurement revealed a RMS roughness value of 3.5 nm on an as-deposited 50 nm Cu film at 120 °C.

AUTOBIOGRAPHICAL STATEMENT

THOMAS JOSEPH KNISLEY

Education	Ph.D., Inorganic Chemistry, Wayne State University, Detroit, MI 2008-2012; GPA: 3.50/4.00 Advisor: Dr. Charles H. Winter
	B.S., Chemistry, University of Michigan–Dearborn, Dearborn, MI 2003-2008; GPA: 3.50/4.00

Publications

1.) “Volatility and High Thermal Stability in Mid to Late First Row Transition Metal Diazadienyl Complexes,” **T. J. Knisley**, M. J. Saly, M. J. Heeg, J. L. Roberts, and C. H. Winter, *Organometallics* **2011**, *30*, 5010-5017.

2.) “Low Temperature Growth of High Purity, Low Resistivity Copper Films by Atomic Layer Deposition,” **T. J. Knisley**, T. C. Ariyasena, T. Sajavaara, M. J. Saly, and C. H. Winter, *Chem. Mater.* **2011**, *33*, 4417-4419.

3.) “Exceptional Thermal Stability and Volatility in Mid to Late First Row Transition Metal Complexes Containing Carbohydrazide Ligands,” M. C. Karunarathne, **T. J. Knisley**, G. S. Tunstull, M. J. Heeg, and C. H. Winter, *Polyhedron*, **2012**, *36*, *http://dx.doi.org/10.1016/j.poly.2012.07.034, invited to submit for the Alfred Werner 100th anniversary issue.*

4.) “Metallic Materials Deposition: Metal-Organic Precursors,” C. H. Winter, **T. J. Knisley**, L. C. Kalutarage, M. A. Zavada, J. P. Klesko, and T. H. Perera, *Encyclopedia of Inorganic and Bioinorganic Chemistry* **2012**, *in press, submitted 5/21/2012.*

5.) “Atomic Layer Deposition of Nickel Nitride Thin Films from a Volatile and Thermally Stable Nickel Diazadienyl Precursor,” **T. J. Knisley**, M. J. Saly, R. Kanjolia, and C. H. Winter, **2012**, *in preparation.*

6.) "Ruthenium Substrate-Catalyzed Growth of Ni_xN by Atomic Layer Deposition," T. C. Ariyasena, **T. J. Knisley**, T. Sajavaara, and C. H. Winter, **2012**, *in preparation.*